

Dipl.-Ing. Hannes Hinterbichler, BSc

SELF-SIMILAR SPRAY FLOW

An investigation of consumer-type sprays

DOCTORAL THESIS

to achieve the university degree of
Doktor der technischen Wissenschaften
submitted to

Graz University of Technology

Supervisor

Univ.-Prof. Dr.-Ing. habil. Günter Brenn
Institute of Fluid Mechanics and Heat Transfer

Second supervisor

Ao.Univ.-Prof. Dipl.-Ing. Dr.techn. Helfried Steiner
Institute of Fluid Mechanics and Heat Transfer

Graz, August 2020

Affidavit

I declare that I have authored this thesis independently, that I have not used other than the declared sources/resources, and that I have explicitly indicated all material which has been quoted either literally or by content from the sources used. The text document uploaded to TUGRAZonline is identical to the present doctoral thesis.

Date

Signature

SELF-SIMILAR **SPRAY FLOW**

**An investigation of
consumer-type sprays**

Hannes Hinterbichler

Acknowledgments

The present investigations on self-similar spray flow have been conducted between 2016 and 2020 at the Institute of Fluid Mechanics and Heat Transfer at Graz University of Technology. I would like to express my sincere gratitude to everyone who accompanied and supported me during my doctoral studies.

I am especially grateful to both of my supervisors, Prof. Günter Brenn and Prof. Helfried Steiner, for their trust and their outstanding academic mentorship. Their invaluable commitment, expertise and suggestions highly contributed to the success of the present thesis. Furthermore, I would like to express my gratitude to Prof. Gianpietro Elvio Cossali from the University of Bergamo for the review of this doctoral thesis.

As a member of the team of the Institute of Fluid Mechanics and Heat Transfer at Graz University of Technology, I have been surrounded by many great colleagues. Thank you for all your help and support. In particular, I would like to thank Christoph Irrenfried and Håkon Bartnes Line for their advice and friendship. My time at the institute has truly been a wonderful experience.

Support by the SIINN ERA-NET, funded under the ERA-NET scheme of the Seventh Framework Programme of the European Commission, Research Directorate - General, Grant Agreement No. 265799, is acknowledged. Financial support from the Austrian Research Promotion Agency FFG (project no. 849876) is acknowledged.

I am very grateful to all my amazing friends who accompanied me during this journey. Special thanks go to Martin Kremsmayr. We started our studies together as bachelor students and he supported me ever since. Thank you for your marvelous friendship. I would also like to thank Richard Forstner for constantly challenging my thoughts and beliefs. I tremendously enjoy our – unfortunately far too rare – conversations and hope for many more to come.

Above all, I am most grateful to my family. Franz and Ulrike, thank you for your endless love and support. Christoph and Eva, thank you for your love and friendship. Katja, thank you for your love, your encouragement and your patience.

Graz, August 2020

Hannes Hinterbichler

Abstract

Sprays generated in atmospheric air by a consumer-type pressure atomizer with off-axis liquid supply are investigated. Measurements are conducted in numerous spray cross sections at a high spatial resolution of the measurement points in radial direction using phase-Doppler anemometry. Altogether, three sprays characterized by different pairs of Weber and Ohnesorge numbers, using two different test liquids, are examined. The liquid mass flow rates are in the same order of magnitude as in commercial consumer sprays. In the sprays, the motion of the gas phase is induced by the interaction with the liquid phase exclusively. The measurements are conducted in a region with large slip between the liquid and the gas phases, governed by strong momentum transfer from the droplets to the gas. Using the phase-Doppler measurement data, a procedure is developed to determine the velocity field of the gas from the motion of small droplets, accounting for bimodal velocity spectra observed at certain measurement locations. The resulting gas-velocity fields exhibit self-similar behavior.

Based on the experimental data, a self-similar description of the gas flow field in the sprays is derived from boundary-layer theory. For this purpose, the momentum transfer from the drops to the gas is accounted for by a source term in the momentum equation. The momentum source is validated against the measurement data showing very good agreement and revealing self-similarity of the liquid phase. The mathematical description of the momentum source accounts for solid-cone and hollow-cone sprays. Remarkably, the obtained self-similar shape function, describing the profiles of the gas velocity components, is the very same as known from axisymmetric single-phase jets. However, the scaling variables of the self-similar coordinate and other flow quantities differ significantly from the single-phase case.

The present study confirms the, long-suspected, self-similarity of spray flow governed by strong liquid-gas momentum transfer, by revealing the self-similarity of the gas velocity field and the momentum loss of the liquid phase. The derived analytical self-similar description of the spray flow is in excellent agreement with the measurement data and provides a convenient starting point for future spray modeling efforts.

Kurzfassung

In der vorliegenden Arbeit werden Sprays, die unter atmosphärischen Bedingungen mittels Druckzerstäubung bei exzentrischer Flüssigkeitszufuhr erzeugt werden, untersucht. Der verwendete Zerstäuber ist exemplarisch für Sprühgeräte, die in Konsumgütern eingesetzt werden. Messungen im Strömungsfeld der Sprays werden in zahlreichen Querschnitten, bei hoher räumlicher Auflösung in radialer Richtung, mittels Phasen-Doppler-Anemometrie durchgeführt. Insgesamt werden drei Sprays untersucht, die durch unterschiedliche Paare von Weber- und Ohnesorge-Zahl charakterisiert sind. Dabei werden zwei verschiedene Flüssigkeiten verwendet. Die Flüssigkeitsmassenströme durch die Düse entsprechen jenen von kommerziell verfügbaren handelsüblichen Sprays. In den untersuchten Sprays wird die Bewegung der Gasphase ausschließlich durch Interaktion mit den Tropfen induziert. Die Messungen decken den Bereich mit großem Schlupf zwischen Flüssig- und Gasphase, beziehungsweise starkem Impulsübergang von den Tröpfchen auf das Gas, ab. Bei der Berechnung der Gasphasengeschwindigkeit aus den Messdaten werden an bestimmten Messpositionen beobachtete bimodale Geschwindigkeitsverteilungen sehr kleiner Tröpfchen berücksichtigt.

Basierend auf der Grenzschichttheorie, und mit Hilfe der Messdaten, wird eine selbstähnliche Beschreibung des Gasströmungsfeldes abgeleitet. Dabei wird der Impulsübergang von den Tröpfchen auf das Gas durch einen Quellterm in der Gasimpulsbilanz berücksichtigt. Der Vergleich von Impulsquelle und Messdaten zeigt sehr gute Übereinstimmung. Dadurch wird auch die Selbstähnlichkeit der Strömung der Flüssigphase in den vorliegenden Sprays bestätigt. Die mathematische Formulierung der Impulsquelle beschreibt Voll- und Hohlkegelsprays. Bemerkenswerterweise ist die selbstähnliche Formfunktion, welche die Geschwindigkeitskomponenten der Gasphase beschreibt, ident mit jener von achsensymmetrischen einphasigen Freistrahlen. Die Skalierungsfaktoren der selbstähnlichen Koordinate und anderer Größen des Strömungsfeldes unterscheiden sich jedoch erheblich vom einphasigen Fall.

Die vorliegende Arbeit bestätigt die seit längerem vermutete Selbstähnlichkeit des Strömungsfeldes in Sprays mit starkem Impulseintrag der Flüssigphase. Dies wird durch die Selbstähnlichkeit des Gasgeschwindigkeitsfeldes und des Impulsverlustes der Flüssigphase aufgezeigt. Die analytische selbstähnliche Beschreibung der Sprayströmung ist in ausgezeichnetem Einklang mit den Messdaten. Weiters stellt sie einen günstigen Ausgangspunkt für zukünftige Arbeiten zur Modellierung von Sprayströmungen dar.

Contents

Acknowledgments	iii
Abstract	v
Kurzfassung	vii
Nomenclature	xi
1 Introduction	1
2 Fundamentals	5
2.1 Spray generation	5
2.1.1 The process of drop formation	5
2.1.2 Pressure atomization	7
2.2 Self-similar jet flow	9
2.2.1 Transport of momentum	10
2.2.2 Transport of other scalar quantities	12
2.3 Self-similar spray flow	13
2.3.1 Literature survey	14
2.3.2 Modeling of equilibrium spray flow	18
3 Experiments	21
3.1 Experimental setup	21
3.2 Phase-Doppler anemometry	24
3.2.1 Fundamentals	24
3.2.2 Local spray characteristics	30
3.2.3 Global spray characteristics	35
3.3 Performed experiments	36
4 Measurement results	39
4.1 Flow field of the liquid phase	39
4.1.1 Local spray characteristics	39
4.1.2 Global spray characteristics	48
4.2 Flow field of the gas phase	52

5	Self-similar modeling	59
5.1	Equations of motion	59
5.2	Self-similar transformation	60
5.3	Scaling variables	63
5.3.1	Axial gas velocity on the spray axis	64
5.3.2	Gas momentum flow rate	64
5.3.3	Normalized axial gas velocity	66
5.3.4	Results	69
5.4	Self-similar shape function	71
5.5	Turbulent eddy viscosity	74
5.6	Momentum source	77
5.6.1	Divergence of liquid momentum	78
5.6.2	Single-drop drag law	80
5.6.3	Comparison	83
5.6.4	Underestimation of the turbulent eddy viscosity	84
5.7	Scope and limitations	93
5.8	Summary	95
6	Predictions	97
6.1	Rate of mass entrainment	97
6.2	Gas-flow turbulent Reynolds number	99
7	Implications	103
7.1	Heat and mass transport	103
7.2	Transition to equilibrium	107
7.3	Self-similarity of the liquid phase	110
7.4	Self-similar planar flows	112
7.4.1	Plane laminar two-phase flow	112
7.4.2	Plane turbulent two-phase flow	115
8	Summary and conclusions	119
	Bibliography	121

Nomenclature

Latin symbols

Symbol	Description	Dimension
a	molecular thermal diffusivity	m^2/s
a_t	effective thermal diffusivity	m^2/s
A	Saffman-corrected probe-volume cross section	m^2
$A_1(z)$	fit function	m/s
$A_2(z)$	fit function	$1/\text{m}^2$
A_m	annular spray cross section	m^2
\tilde{A}	constant	–
B	unit width	m
B_1, B_2	fit parameters	–
\tilde{B}	constant	m^3/s
c_l	concentration of liquid mass	kg/m^3
c_n	drop number concentration	$1/\text{m}^3$
c_p	specific isobaric heat capacity	$\text{J}/(\text{kg K})$
C	model constant	m^2/s
C_μ	empirical constant	–
\tilde{C}	constant	–
d	(drop) diameter	m
d_{or}	orifice diameter	m
d_v	diameter of the probe-volume cross section	m
Δd	size class width	m
D	model constant	$\text{m}^\alpha - 1$
D_a	constant of the single-phase round jet	–
D_{10}	number-mean drop diameter	m

NOMENCLATURE

Symbol	Description	Dimension
\overline{D}_{10}	global number-mean drop diameter	m
D_{32}	Sauter mean drop diameter	m
\overline{D}_{32}	global Sauter mean drop diameter	m
\tilde{D}	constant	$\text{m}^{3\alpha - 1}/\text{s}^\alpha$
\underline{D}	number of drop size classes	–
\mathcal{D}_t	effective diffusion coefficient	m^2/s
\tilde{E}	constant	m^2/s
$f(\eta)$	self-similar shape function	–
f_0	frequency	1/s
f_b	beat frequency	1/s
f_d	momentum source	m/s^2
\bar{f}_d	mean scaled momentum source	$\text{m}^{4\alpha}/\text{s}^2$
$\Delta f_1, \Delta f_2$	frequency shift	1/s
F	model constant	$\text{kg}/\text{m}^3 + \beta$
F_d	drag force	N
g	scaling function	1/m
h	mapping function	m^3/s
\hbar	Planck's constant	J s
\mathcal{H}	enthalpy flow rate	W
i	imaginary unit, integer	–
I	number of radial measurement locations	–
\mathcal{I}	momentum flow rate	N
j	integer	–
k	turbulent kinetic energy	m^2/s^2
k_s	scaling function	–
K_e	entrainment rate coefficient	–
\hat{K}_e	modified entrainment rate coefficient	–
ℓ	characteristic length scale	m
$\ell_{0.5}$	jet half-width	m
ℓ_p	trajectory length of a particle	m
m	relative refractive index	–

Symbol	Description	Dimension
m_s	exponent of the streamwise momentum flow rate	–
\dot{m}	mass flow rate	kg/s
\dot{m}_{or}	initial mass flow rate	kg/s
\dot{m}^+	nondimensional entrainment rate	–
M_{exp}	fit parameter	$\text{kg m}^{2\alpha - 1}/\text{s}^2$
\mathcal{M}_j	vapor mass flow rate	kg/s
n	number of drops	–
\hat{n}	Saffman-corrected number of drops	–
N	total number of drops	–
p	pressure	Pa
\mathcal{P}	turbulent kinetic energy production rate	m^2/s^3
r	radial coordinate	m
Δr	radial spacing	m
R_{exp}	fit parameter	$\text{m}^{1 - \alpha}$
R^2	coefficient of determination	–
S_h	heat source	W/m^3
S_j	vapor source	$\text{kg}/(\text{m}^3 \text{ s})$
t	scaling function	kg/m^3
t_f	relaxation time scale of the continuous phase	s
t_p	relaxation time scale of a particle	s
Δt	measuring time	s
T	temperature	K
u	axial velocity component	m/s
u_0	axial velocity component at the spray axis	m/s
\bar{u}	mean axial velocity	m/s
\hat{u}_l	volume mean axial liquid velocity	m/s
\check{u}_l	mean axial velocity of the liquid phase	m/s
u'	axial velocity fluctuation	m/s
$\overline{u'^2}$	mean squared axial velocity fluctuation	m^2/s^2
$\overline{u'v'}$	cross-correlation of velocity fluctuations	m^2/s^2
U_{exp}	fit parameter	$\text{m}^{2\alpha}/\text{s}$

NOMENCLATURE

Symbol	Description	Dimension
\underline{U}	number of axial velocity classes	–
v	radial velocity component	m/s
\bar{v}	mean radial velocity	m/s
\check{u}_l	mean radial velocity of the liquid phase	m/s
v'	radial velocity fluctuation	m/s
$\overline{v'^2}$	mean squared radial velocity fluctuation	m ² /s ²
\underline{V}	number of radial velocity classes	–
w	total velocity	m/s
\bar{w}	mean total velocity	m/s
W	slit width	m
\underline{W}	number of velocity classes	–
x	coordinate	m
Δx	fringe spacing	m
y	coordinate	m
z	axial coordinate	m
z_0	virtual origin	m
z_b	limit of the regime of liquid-gas momentum transfer	m

Greek symbols

Symbol	Description	Dimension
α	model exponent	–
α_c	model parameter of Chao (1964)	1/s
β	model exponent	–
β_c	model parameter of Chao (1964)	–
γ	inclination angle of the drop trajectory	rad
Γ_1	change of liquid momentum	kg/(m ² s ²)
$\bar{\Gamma}_1$	mean scaled change of liquid momentum	kg m ^{4α - 3} /s ²
Γ_2	change of liquid momentum	kg/(m ² s ²)
$\bar{\Gamma}_2$	mean scaled change of liquid momentum	kg m ^{4α - 3} /s ²
$\underline{\Gamma}$	number of trajectory classes	–

Symbol	Description	Dimension
$\delta_{0.05}$	jet full-width at the 5% points of the axial velocity	m
ε	viscous dissipation rate	m^2/s^3
η	self-similar coordinate	–
θ_d	diameter validation rate	–
ϑ	beam half angle	rad
$\Theta(\eta)$	self-similar vapor concentration	–
$\Theta_a(\eta_a)$	self-similar temperature field of the single-phase jet	–
κ	exponent	–
λ	wavelength	m
μ	dynamic viscosity	Pa s
ν	molecular kinematic viscosity	m^2/s
ν_t	eddy viscosity	m^2/s
ξ	elevation angle	rad
ρ	density	kg/m^3
ϱ	vapor concentration	kg/m^3
σ	surface tension	N/m
τ	time scale	s
τ_l	drop transit time	s
τ_t	eddy turnover time	s
τ_μ	Kolmogorov time scale	s
ϕ	liquid mass flux	$\text{kg}/(\text{m}^2 \text{s})$
φ	scattering angle	rad
Φ	liquid momentum flux	N/m^2
$\Phi_j(\eta)$	self-similar vapor source	–
$\Delta\Phi$	phase shift	rad
ψ	drop number flux	$1/(\text{m}^2 \text{s})$
Ψ	Stokesian stream function	m^3/s
ω_c	turbulent angular fluctuation frequency	1/s
$\Omega(\eta)$	self-similar momentum source	–
$\Omega_c^{(1)}$	spectral kinetic energy of the particle	–
$\Omega_c^{(2)}$	spectral kinetic energy of the continuous phase	–

Subscripts

Symbol	Description
2	referring to the regime of liquid-gas momentum transfer
4	referring to the regime of constant momentum flow rate
∞	in the far field
a	referring to the single-phase round jet
c	referring to the work of Chao (1964)
d	drop size class
exp	experimentally obtained
i	radial measurement location, integer
I	continuity of the axial velocity
II	continuity of the self-similar coordinate
j	vapor or liquid component
l	liquid or drop
max	maximum
or	atomizer orifice, initial condition
p	particle
q	referring to plane laminar two-phase flow
r	in radial direction
s	referring to plane turbulent two-phase flow
t	turbulent
u	axial velocity class
v	radial velocity class
w	velocity class
z	in axial direction
γ	drop trajectory class

Superscripts

Symbol	Description
(a)	referring to the divergence of liquid momentum

Symbol	Description
(b)	referring to the single drop drag law
*	conjugate complex number

Nondimensional numbers

Symbol	Description
Oh	Ohnesorge number
Pr	Prandtl number
Re	Reynolds number
Sc	Schmidt number
We	Weber number
St	Stokes number

Acronyms

Abbreviation	Description
LDV	laser-Doppler velocimetry
LHF	locally homogeneous flow
ODE	ordinary differential equation
PDA	phase-Doppler anemometry
PDE	partial differential equation
PDF	probability density function
PDIA	particle/droplet imaging analysis
PIV	particle image velocimetry
PTV	particle tracking velocimetry
STD	standard deviation

Chapter 1

Introduction

Sprays are everywhere. They occur in natural phenomena, like sea sprays, drizzle and rainfall, many industrial processes, numerous consumer products and they are relevant for the most basic applications in everyday life in human society. In general, a spray is characterized by a system of drops immersed in a continuous gaseous phase (Lefebvre and McDonell 2017). The generation of sprays for a specific purpose requires the controlled atomization of bulk liquid in a gaseous environment. For this reason, the process of spray generation and the design of suitable and efficient atomizers has been extensively studied for almost a century. Typical spray applications are found in combustion, spray drying and coating, atomization of liquid metals, agricultural crop spraying, cleaning, air conditioning and medical sprays (Bayvel and Orzechowski 1993; Lefebvre and McDonell 2017). The list of examples could be continued at will.

Developments in nanotechnology during the past decades enable the application of manufactured nanomaterials in consumer spray products. To enhance the desired effects, they may be used as ingredients in commercially available spray products, like waterproofing sprays or body care products in the near future (Kessler 2011; Lorenz et al. 2011). Moreover, the use of manufactured nanomaterials is already under consideration for various other areas of application, for example as nanofertilizer in agriculture (Raliya et al. 2018). Little is known about the potential for inhalation exposure and the connected health risks of nanoparticle-laden sprays (Quadros and Marr 2010, 2011; Nazarenko et al. 2011). The models of exposure assessment available are stochastic in nature (Park et al. 2017, 2018) and do not directly describe the deterministic nature of the underlying physical processes. The present study aims to contribute to the realistic assessment of health risks connected to nanoparticulate or other hazardous content in consumer spray products, by investigating and modeling the flow field of pressure-atomized consumer-type sprays.

Self-similar phenomena are well-known in mathematics and physics, and can also be observed in the structure of plants in nature (Barnsley 1993; Barenblatt 1996). In fluid dynamics, self-similar phenomena occur in flows without imprinted length or time scales (Brenn 2017). To describe the concept of self-similarity, we follow the example of Pope (2000). Consider a quantity $Q(x, y)$, depending on two independent variables x and

y . As a function of one of the two independent variables, x in the present case, we define characteristic scales $\delta(x)$ and $Q_0(x)$ for the other independent variable y and the dependent variable $Q(x, y)$, respectively. Consequently, the scaled variables

$$\zeta := \frac{y}{\delta(x)} \quad \text{and} \quad \tilde{Q}(\zeta, x) := \frac{Q(x, y)}{Q_0(x)} \quad (1.1)$$

can be defined. If the scaling variables $\delta(x)$ and $Q_0(x)$ are chosen such that the scaled dependent variable $\tilde{Q}(\zeta, x)$ is independent of x , i.e.

$$\tilde{Q}(\zeta, x) = \hat{Q}(\zeta), \quad (1.2)$$

then $Q(x, y)$ is self-similar. The advantages of self-similarity are clearly evident if we consider that the quantity $Q(x, y)$ is governed by a partial differential equation (PDE). Since $Q(x, y)$ is self-similar, it can be expressed by the quantities $\delta(x)$, $Q_0(x)$ and $\hat{Q}(\zeta)$, each depending on a single variable only. Thus, the partial differential equation reduces to an ordinary differential equation (ODE).

The origins of the concept of self-similarity applied to fluid dynamics are difficult to trace (George 1989). First notable contributions were made by the self-similar descriptions of the laminar boundary layer by Blasius (1908) and the axisymmetric single-phase jet by Schlichting (1933). Self-similar phenomena in spray flow are widely reported in the literature. For example, they are known to occur in sprays generated by air-assisted atomization (Li and Shen 1999), in Diesel sprays (Wu et al. 1984; Payri et al. 2016) and in spray flames (Karpetsis and Gomez 1999). In regions of the spray where the droplets and the gas are in dynamic equilibrium, the spray flow was modeled similar to a single-phase jet, but with variable density to account for the presence of the drops (Shearer et al. 1979; Desantes et al. 2011). In many of the studies reported in the literature, liquid and gas were injected simultaneously, resulting in negligible slip between the drops and the gas. This endorses self-similarity with similar scaling as observed in single-phase jets, since the cross-sectional averages of gas and liquid momentum flow rates remain approximately constant.

In this study, we investigate sprays where the motion of the gas is induced by interaction with the liquid drops exclusively. The sprays are generated in atmospheric air by a single-phase pressure-atomizer with off-axis liquid supply, as in use with consumer spray cans. The liquid mass flow rates are of the order of magnitude of commercial consumer spray products. We focus on the region of the sprays where large slip between the drops and the gas phase occurs. The dynamics of this region are governed by strong liquid-gas momentum transfer, effectively reducing the cross-sectional momentum flow rate of the liquid phase and raising the one of the gas phase as the spray propagates downstream. For the experimental characterization of the sprays, we employ phase-

Doppler anemometry (PDA). Using this experimental technique, the size and two velocity components of individual droplets passing the probe volume are measured. To obtain a reliable experimental data set for our modeling efforts, extensive measurements in several cross sections at high spatial resolution are conducted. The main objectives of the present investigation are: (1) The experimental characterization of pressure-atomized consumer-type spray flow, (2) the identification of possibly self-similar behavior and (3) the derivation of a corresponding self-similar mathematical description.

The remainder of the thesis is structured as follows: In *Chapter 2*, we derive the theoretical basis for our work and present a thorough literature survey on self-similar phenomena in spray flow. In *Chapter 3*, we discuss the spray test rig, the measurement technique and the parameters of the experiments. *Chapter 4* presents the measurement results. Moreover, the determination of the gas-phase velocity field from the PDA measurement data is discussed. In *Chapter 5*, we derive an analytical self-similar model from boundary-layer theory to describe the gas flow field in the sprays. For that matter, the momentum transfer from the droplets to the gas is accounted for. All aspects of the obtained model are thoroughly discussed and compared to the measurement data. *Chapter 6* compares certain predictions of the model to results reported in the literature. In *Chapter 7*, we identify possible further investigations, like the extension of the model to heat and mass transfer in evaporating sprays and its application to geometrically different kinds of spray flow. *Chapter 8* concludes the study. The core results of this thesis are published in Hinterbichler et al. (2020).

Chapter 2

Fundamentals

The present chapter provides the theoretical foundation of this study. First, we briefly introduce the fundamentals of spray formation. As a classical example with significant relevance for the present analysis, we then introduce the mathematical description of the self-similar flow field in axisymmetric single-phase jets. Finally, in section 2.3, the current literature on self-similar phenomena in sprays is reviewed.

2.1 Spray generation

The controlled atomization of bulk liquid in a gaseous environment is substantial for a large variety of processes and applications in human society. The main areas of utilization are power engineering, mechanical engineering, chemical engineering, transport, agriculture, environmental protection and various other applications, for example in human health protection and in the food industry (Bayvel and Orzechowski 1993). In the present study, we investigate the flow field of sprays generated by consumer-type spray cans. Our analysis focuses on the downstream propagation of the spray after the drop formation is finished. Thus, the process of atomization per se, which is influenced by the geometrical details of the atomizer, is not a subject of the present work. For completeness, however, we shall provide a brief overview of the mechanisms of spray formation and the regimes of spray development to be expected from an atomizer such as used in the present study.

2.1.1 The process of drop formation

In general, the main goal of the atomization process is the dispersion of liquid in an ambient gaseous phase. To facilitate the desired effects, the resulting droplets should, for example, be as small as possible. Thus, a large interfacial surface area and proper mixing is ensured. In this way, the objectives of the process, for example the evaporation of liquid fuel for combustion or the cooling of a hot air stream, are achieved. The purpose of the atomizer is to ensure proper atomization of the bulk liquid as required for the task at hand. On the one hand, this is achieved by large relative velocities between the liquid and the gas phases. On the other hand, the atomizer is designed such that the formed

liquid shapes are prone to instabilities and therefore disintegrate into droplets. The first stage of the atomization process, where large continuous liquid structures breakup into individual filaments and large droplets, is called *primary atomization*. *Secondary atomization* denotes the subsequent breakup of large droplets into smaller drops due to aerodynamic forces.

According to Lefebvre and McDonell (2017), there are three basic mechanisms for primary atomization. These are the disintegration of liquid jets, the disintegration of liquid sheets and a mechanism called *prompt atomization*. The first two mechanisms involve the emergence of large liquid structures from the atomizer orifice, which are subject to fast growing instabilities and ultimately break up into smaller structures like ligaments and droplets. In certain cases, when there is insufficient time for the growth of instabilities, the liquid is shattered into droplets immediately after ejection and the notion of growing instabilities can be dismissed (Lefebvre and McDonell 2017). This mechanism of atomization has been termed *prompt* by Lefebvre (1992).

Early works on the disintegration of liquid jets date back more than a century (Rayleigh 1878, 1879). Weber (1931) extended Lord Rayleigh's inviscid theory to describe the breakup of viscous jets. Ohnesorge (1936) studied the breakup of liquid jets systematically, varying the fluid properties of the jet, the initial jet velocity and the nozzle diameter. He identified three main regimes of jet disintegration, namely Rayleigh jet breakup, wind-induced breakup and atomization. He observed that the regime of breakup was determined by the Reynolds number of the jet and a second nondimensional group, which would later be termed the Ohnesorge number. As a result of further scientific efforts, the wind-induced breakup regime was subdivided into the first wind-induced breakup regime and the second wind-induced breakup regime (Reitz 1978).

The Rayleigh jet breakup mechanism is caused by axisymmetric deformations of the jet surface. At certain wavelengths, the deformations are amplified by surface tension, leading to the disintegration of the jet. This effect is the so-called Plateau-Rayleigh instability (Plateau 1873; Rayleigh 1878). In the first wind-induced breakup regime, the effect of surface tension is amplified by the relative motion between the liquid and the gas, accelerating the breakup process. The resulting drops are of the same order of magnitude in diameter as the jet. In the second wind-induced breakup regime, the growth of unstable short waves on the surface of the jet, caused by the relative motion between the liquid and the gas phases, lead to its disintegration. In this case, surface tension opposes the wave growth. The resulting drop are much smaller in diameter than the jet. In the atomization regime, the liquid jet is immediately disrupted on entering the gaseous atmosphere at the nozzle orifice.

To produce small droplets from liquid feed streams in cylindrical ducts, either very small nozzles or high energy input is required (Walzel 2019). To overcome this disadvantage, the formation of drops from disintegrating liquid sheets represents a more favorable

approach. Liquid sheets generated by atomizers are typically of a flat or conical shape. Sheets can also be produced by two impinging jets (Taylor 1960). According to Fraser and Eisenklam (1953), there are three main modes of sheet disintegration, called *rim mode*, *wave mode* and *perforated sheet mode*. In the rim mode, the free edge of the liquid sheet contracts into a thick rim due to surface tension. This rim is subject to the same instabilities as a liquid jet and disintegrates into droplets by similar means. Wave motion on the sheet can lead to its disintegration, as liquid structures are torn away before the leading edge of the sheet is reached (Lefebvre and McDonell 2017). The perforated sheet mode is characterized by the formation of holes in the sheet. As the holes grow in size, liquid rims are formed at the free edges of the holes. When the rims of adjacent growing holes coalesce, irregular structures are formed which disintegrate into ligaments and droplets. In practice, the boundaries of transition between these three modes of sheet disintegration are not clear and they often occur superimposed (Walzel 2019).

After the primary atomization process, the resulting drops themselves may be subject to further breakup due to aerodynamic forces. This process is called secondary atomization. In general, secondary atomization of droplets occurs when the aerodynamic forces due to drag exceed the surface tension forces. As a consequence, the drop deforms and disintegrates into smaller droplets. Typically, this limit is expressed by a critical Weber number of the droplet (Lefebvre and McDonell 2017). Depending on the drop size, the relative velocity between the drop and the gas, and the physical properties of the liquid and the gas phases, eight different breakup regimes are known. Their description and the definition of the relevant parameters involved can be found elsewhere (Shraiber et al. 1996; Wozniak 2003).

2.1.2 Pressure atomization

Numerous atomizer designs have been developed over time. Bayvel and Orzechowski (1993) classify the atomizers by the type of energy used for the atomization into four basic categories. These are, *liquid energy*, *gas energy*, *mechanical energy* and *other types of energy*. Lefebvre and McDonell (2017) follow a similar approach. Most commonly, the energy for the atomization is provided by the liquid itself. The pressure drop through the atomizer is converted into kinetic energy to achieve high relative velocities between the liquid and the gas. A plain orifice represents the simplest example for a pressure atomizer, where a liquid jet is ejected into a gaseous environment. A different concept for pressure atomization is given by swirl atomizers (also called simplex atomizers). Due to the swirling liquid inside the atomizer orifice, they eject a conical liquid sheet instead of a liquid jet. Gas-assisted atomizers use the kinetic energy of a high-speed gas flow to disintegrate the liquid. Their design is complex because liquid and gas flow through the atomizer. Compared to pressure atomizers, their operation is also more elaborate, since,

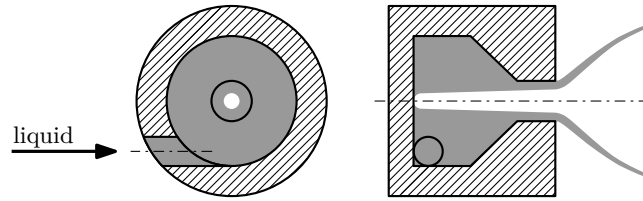


Figure 2.1: Schematic design of a pressure-swirl atomizer (adapted from Lefebvre and McDonell 2017).

in addition to the liquid, pressurized air has to be provided (Lefebvre and McDonell 2017). Rotary atomizers use mechanical energy to atomize the liquid. A rotating surface transfers its rotational energy to the liquid and ejects it by means of centrifugal forces. A flat disk represents the simplest form for the rotating surface, but there are several other designs like vaned disks, cups, or slotted wheels. (Lefebvre and McDonell 2017). The fourth category of Bayvel and Orzechowski (1993) covers all other forms of energy used for atomization. This includes, for example, ultrasonic atomizers, electrostatic atomizers and flash-boiling atomization. For a comprehensive review on the technical design of atomizers we refer to others (Bayvel and Orzechowski 1993; Lefebvre and McDonell 2017).

The atomizer used in the present experiments is a simple single-phase pressure atomizer, as used in many consumer spray cans. Due to an eccentric liquid supply to the nozzle orifice, see section 3.1, angular momentum is imposed on the ejected liquid. The emerging liquid structures appear very similar to the ones generated by classical pressure-swirl atomizers. For this reason, we will introduce the basic design of pressure-swirl atomizers and the properties of the sprays they produce.

Figure 2.1 depicts the basic design of a pressure-swirl atomizer. The liquid enters the swirl chamber through one, or in practice typically several, inlets tangentially. On its path to the nozzle exit, the swirl chamber narrows to increase the liquid swirl. As a consequence of the large centrifugal forces, a gaseous core is formed near the swirl axis. As the liquid is ejected through the nozzle, its high azimuthal velocity is quickly converted into radial motion, forming a liquid sheet (Schmidt et al. 1999). The liquid sheet disintegrates into droplets due to the mechanisms described in section 2.1.1. Depending on the pressure difference between liquid and ambient gas, five different regimes of spray development may occur. The different regimes are illustrated in figure 2.2. The characteristics of the different regimes, according to Lefebvre and McDonell (2017), are described below.

- (a) In the dribble stage, at very low pressure, liquid simply dribbles from the orifice.
- (b) A liquid jet is ejected, forming a distorted pencil.
- (c) A curved sheet is formed, but contracted into a closed bubble-shaped lamella due to surface tension.

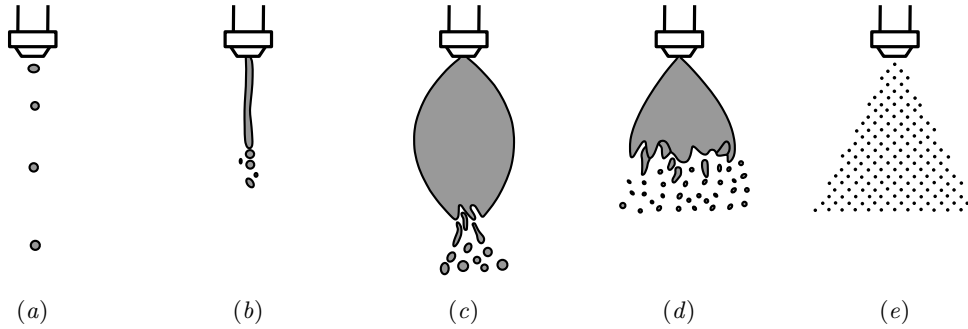


Figure 2.2: Spray development in pressure-swirl atomizers (adapted from Lefebvre and McDonell 2017). (a) dribble stage, (b) distorted pencil, (c) onion stage, (d) tulip stage, (e) fully developed spray. The liquid injection pressure increases from (a) to (e).

- (d) The bubble opens, forming a hollow tulip-shaped sheet. The liquid film is still quite smooth. At the ragged edges of the sheet, the liquid disintegrates coarsely into large droplets.
- (e) The curved liquid tulip straightens to form a hollow conical sheet. Its thickness decreases as the sheet expands and it quickly disintegrates into a well-defined hollow-cone spray.

Note that the gaseous core is only formed in stages (c) to (e). In stages (a) and (b), the swirl chamber is entirely filled with liquid. Depending on the design of the pressure-swirl atomizer, solid-cone or hollow-cone sprays are generated. In the former, the liquid is distributed fairly uniformly throughout each spray cross section. In hollow-cone sprays, the liquid mass is concentrated at the outer edge of the spray. They are characterized by finer atomization compared to solid-cone sprays (Lefebvre and McDonell 2017).

2.2 Self-similar jet flow

The axisymmetric single-phase submerged jet represents a classical example of self-similar behavior in free shear flow. Schlichting (1933) derived a mathematical description of the self-similar two-dimensional flow field of the laminar round jet. His model turned out to be applicable to predict the mean flow field in turbulent jets as well, simply by using the turbulent eddy viscosity instead of the molecular kinematic viscosity as a model parameter (Pope 2000). It has been experimentally confirmed many times since, e.g. Wygnanski and Fiedler (1969), Panchapakesan and Lumley (1993a), Hussein et al. (1994), and Djenidi et al. (2016). The flow field of the single-phase round jet is schematically illustrated in figure 2.3. The fluid exits the nozzle (diameter d_{or}) with the mean velocity \bar{u}_{or} . After a short transition zone, a self-similar flow field emerges. Along lines where the

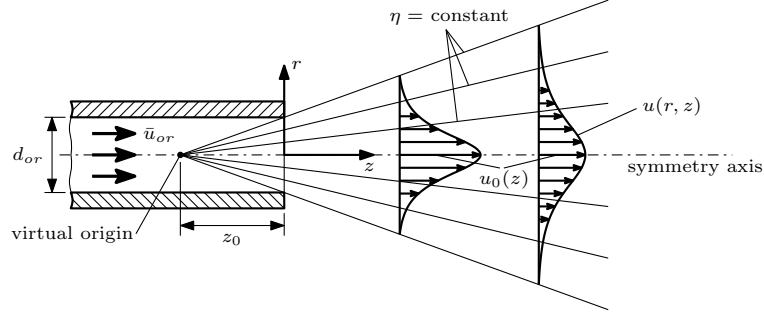


Figure 2.3: Flow field of a single-phase round jet.

values of the self-similar coordinate η are constant, the axial velocity ratio $u(r, z)/u_0(z)$ is constant as well. $u_0(z)$ denotes the axial velocity at the symmetry axis of the jet. As illustrated, constant values of η are represented by straight lines in (r, z) space. Thus, the origin of the self-similar flow field may be conceived as a point source of mass and momentum (George 1989). This singular point in space is called the virtual origin of the flow field, and its location is denoted by z_0 in figure 2.3. Due to the singularity, the mathematical description obviously does not match real jets at coordinates very close to the virtual origin. In general, the virtual origin does not necessarily coincide with the nozzle exit, but lies in its close vicinity. The exact location of z_0 depends on the geometry of the nozzle and the flow conditions through the orifice.

2.2.1 Transport of momentum

In the following, we present the self-similar description of the single-phase round jet by Schlichting (1933). It serves as a basis for the modeling of self-similar spray flow in the present study. The laminar flow field illustrated in figure 2.3 can be described by the boundary layer equations in cylindrical coordinates with constant pressure throughout, reading

$$\frac{\partial u}{\partial z} + \frac{1}{r} \frac{\partial(vr)}{\partial r} = 0 \quad \text{continuity} \quad (2.1)$$

$$u \frac{\partial u}{\partial z} + v \frac{\partial u}{\partial r} = \nu \frac{1}{r} \frac{\partial}{\partial r} \left(r \frac{\partial u}{\partial r} \right) \quad z\text{-momentum} \quad (2.2)$$

$$\frac{\partial p}{\partial r} = 0 \quad r\text{-momentum} \quad (2.3)$$

The molecular kinematic viscosity is denoted by ν . u and v are the velocity components in axial and radial direction, respectively. In the following, the subscript a refers to the

axisymmetric single-phase jet. The ansatz to obtain a self-similar flow field reads

$$\eta_a = D_a \frac{r}{(z - z_0)} \quad \text{and} \quad \Psi_a = \nu(z - z_0) f_a(\eta_a), \quad (2.4)$$

where we require for the self-similar coordinate $\eta_a \propto (z - z_0)^{-1}$ and for the Stokesian stream function $\Psi_a \propto (z - z_0)$ in order for (2.2) to be independent of z and to ensure global momentum conservation (Schlichting 1933). $f_a(\eta_a)$ represents the self-similar shape function and D_a denotes a constant model parameter. Note that Schlichting (1933) did not introduce the parameter D_a in the definition of the self-similar coordinate η_a , but in the solution for $f_a(\eta_a)$. As we will show later, in section 5.2, the definition of η_a including the parameter D_a is of a more general nature, because self-similar coordinates with arbitrary axial scaling require a constant parameter for dimensional reasons (Brenn 2017). Naturally, the self-similar description derived by Schlichting (1933) and the one discussed in the present section are equivalent.

The Stokesian stream function Ψ_a is defined through the axial and radial velocity components as

$$u = \frac{1}{r} \frac{\partial \Psi_a}{\partial r} = \frac{\nu D_a^2}{(z - z_0)} \frac{f'_a}{\eta_a}, \quad (2.5)$$

$$v = -\frac{1}{r} \frac{\partial \Psi_a}{\partial z} = \frac{\nu D_a}{(z - z_0)} \left(f'_a - \frac{f_a}{\eta_a} \right), \quad (2.6)$$

automatically satisfying the continuity equation (2.1). Substituting the velocity components into the z -momentum equation (2.2) yields an ordinary differential equation (ODE) for the self-similar shape function (Brenn 2017)

$$-\left(\frac{f_a f'_a}{\eta_a} \right)' = \left[\eta_a \left(\frac{f'_a}{\eta_a} \right)' \right]', \quad (2.7)$$

where the prime denotes the derivative with respect to η_a . Equation (2.7) with the boundary conditions (Schlichting 1933)

$$f_a(0) = 0 \quad \text{and} \quad f'_a(0) = 0 \quad (2.8)$$

is satisfied by the self-similar shape function

$$f_a(\eta_a) = \frac{\eta_a^2}{1 + \eta_a^2/4}, \quad (2.9)$$

which can easily be verified by introducing (2.9) into (2.7). Momentum conservation requires the initial jet momentum flow rate \mathcal{I}_{or} to be conserved as the jet propagates

downstream. Thus, we can determine the parameter D_a from the global momentum balance, reading

$$\mathcal{I}_{or} = 2\pi\rho \int_{r=0}^{\infty} u^2 r \, dr = 2\pi\rho\nu^2 D_a^2 \int_{\eta_a=0}^{\infty} \frac{f_a'^2}{\eta_a} \, d\eta_a = \frac{16\pi}{3} \rho\nu^2 D_a^2. \quad (2.10)$$

Here, ρ denotes the fluid density. For D_a follows

$$D_a = \frac{1}{4\nu} \sqrt{\frac{3\mathcal{I}_{or}}{\pi\rho}}. \quad (2.11)$$

Self-similarity has been observed in many other types of jet flow. Self-similar solutions were derived for the flow fields of axisymmetric buoyant jets, for swirling jets, and also for plane jets. Self-similar flow fields in jets interacting with solid bodies are documented as well, i.e. wall jets and swirling jets propagating along solid cones. They are, however, not considered in the present review. Their description can be found elsewhere (Tropea et al. 2007; Schlichting and Gersten 2017).

2.2.2 Transport of other scalar quantities

In cases where the temperature of the fluid emerging from the orifice (see figure 2.3) differs from the temperature of the environment, the resulting temperature field of the jet can be described as self-similar as well (Schlichting and Gersten 2017). The same is true for the concentration field if the jet consists of a fluid different from the environment, e.g. a helium jet injected into ambient air (Panchapakesan and Lumley 1993b). In the following, we derive the mathematical description of the self-similar temperature field. This derivation is also applicable to obtain a self-similar concentration field.

The cylindrical axisymmetric thermal energy equation (temperature T), obtained from boundary layer theory, reads

$$u \frac{\partial T}{\partial z} + v \frac{\partial T}{\partial r} = a \frac{1}{r} \frac{\partial}{\partial r} \left(r \frac{\partial T}{\partial r} \right), \quad (2.12)$$

where a denotes the thermal diffusivity. The ansatz for the self-similar temperature field is given by

$$T - T_{\infty} = \frac{F_a}{(z - z_0)} \Theta_a(\eta_a), \quad (2.13)$$

where T_{∞} is the ambient temperature in the far field, F_a a constant parameter required for dimensional reasons, and $\Theta_a(\eta_a)$ the self-similar temperature profile. Introducing (2.13), and the velocity components (2.5) and (2.6), into the energy equation (2.12) yields

$$Pr (f_a \Theta_a)' + (\eta_a \Theta_a')' = 0. \quad (2.14)$$

Here, the molecular Prandtl number is denoted by Pr . Using the boundary conditions (Tropea et al. 2007)

$$\Theta_a(\infty) = 0 \quad \text{and} \quad \Theta_a'(0) = 0, \quad (2.15)$$

equation (2.14) has the following solution for the self-similar temperature profile (Tropea et al. 2007)

$$\Theta_a(\eta_a) = \left(\frac{f_a'}{\eta_a} \right)^{Pr}. \quad (2.16)$$

The invariant of the thermal field is given by the excess heat transport rate of the jet, \mathcal{H}_{or} , (Tropea et al. 2007). Its definition reads

$$\begin{aligned} \mathcal{H}_{or} &= 2\pi\rho c_p \int_{r=0}^{\infty} u(T - T_{\infty})r \, dr = 2\pi\rho c_p \nu F_a \int_{\eta_a=0}^{\infty} f_a' \Theta_a \, d\eta_a = \\ &= 8\pi\rho c_p \nu F_a \frac{2^{Pr}}{2Pr + 1}, \end{aligned} \quad (2.17)$$

where c_p denotes the specific isobaric heat capacity of the jet. From (2.17), the constant F_a can be calculated to

$$F_a = \frac{(2Pr + 1)}{2^{Pr}} \frac{\mathcal{H}_{or}}{8\pi\rho c_p \nu} \quad (2.18)$$

and the ansatz for the self-similar temperature field (2.13) turns into

$$T - T_{\infty} = \frac{(2Pr + 1)\mathcal{H}_{or}}{8\pi\rho c_p \nu (z - z_0)} \left(\frac{f_a'}{2\eta_a} \right)^{Pr}. \quad (2.19)$$

The dependency of the jet temperature on the axial coordinate is the same as for the jet velocity. For $Pr = 1$, the shapes of the self-similar temperature and velocity profiles are identical.

2.3 Self-similar spray flow

In the following, the existing literature on self-similar phenomena in spray flow is reviewed. In section 2.3.2, we discuss a mathematical model describing the self-similar flow field in sprays where drops and gas are in dynamic equilibrium.

2.3.1 Literature survey

Self-similarity in sprays is widely reported in the literature. To facilitate a clear overview, the studies are divided into six different categories. Note, however, that this categorization is somewhat arbitrary and some of the studies may fit into other than the selected category as well.

Air-assisted atomization

Li and Shen (1999) reported self-similar axial drop velocity profiles and self-similar profiles of the axial drop velocity fluctuations in sprays generated by twin-fluid atomization of water jets exposed to an inner high-speed air stream. The flow field became self-similar at axial distances from the orifice $z/d_{or} > 29.5$. The self-similar mean axial drop velocity profile was described by the empirical correlation

$$\frac{\bar{u}_l(r, z)}{\bar{u}_{l,0}(z)} = \cosh^{-2}(10.4\eta) , \quad (2.20)$$

where they used the self-similar coordinate of the single-phase round jet, $\eta = r/z$. The mean drop velocity at the spray axis, $\bar{u}_{l,0}$, showed a similar scaling as observed in the single-phase jet

$$\bar{u}_l(z) = \frac{\hat{C}}{z} \sqrt{\frac{\mathcal{I}_{or}}{\rho}} , \quad (2.21)$$

but with a different constant correlation coefficient \hat{C} . Values of \hat{C} are reported for a variety of different combinations of water and airflow velocities at the nozzle exit (Li and Shen 1999).

Vega et al. (2000) reported self-similar velocity profiles and turbulence intensities in a coaxial airblast atomized spray. Copan et al. (2001) found self-similar axial drop velocity profiles at axial distances $z/d_{or} > 25$ in sprays generated by a twin-fluid nozzle (liquid nitrogen and air). Ariyapadi et al. (2003) generated sprays with a similar twin-fluid nozzle (water and air) and obtained self-similar mean axial drop velocity profiles when plotting them against the radial coordinate divided by the spray half-width $\ell_{0.5}$. The spray half-width increased linearly with z , following the relation

$$\frac{\ell_{0.5}}{d_{or}} = 4.7 + 0.024 \frac{z}{d_{or}} . \quad (2.22)$$

The self-similar mean axial drop velocity profile was described by

$$\frac{\bar{u}_l(r, z)}{\bar{u}_{l,0}(z)} = 0.18 + \frac{2.1}{4(r/\ell_{0.5})^2 + 1.6^2}, \quad (2.23)$$

where the constant value of 0.18 for $r \rightarrow \infty$ was explained by the presence of fast drops with high inertia.

Chen et al. (2006) reported self-similar mean axial drop velocity profiles of the smallest drops ($d < 3 \mu\text{m}$) in air assisted atomization of acetone jets ejected into a uniform co-flowing airstream. To make the velocity profiles collapse on a single self-similar curve, they used the self-similar coordinate of the single-phase jet. They determined the following equation to represent the self-similar velocity profile of drops with $d < 3 \mu\text{m}$

$$\frac{\bar{u}_l(r, z) - u_\infty}{\bar{u}_{l,0}(z) - u_\infty} = \exp \left[-\ln(2) \left(\frac{r}{\ell_{0.5}} \right)^2 \right], \quad (2.24)$$

with account for the velocity u_∞ of the co-flowing air.

Hoeg et al. (2008) obtained self-similar axial gas and drop velocity profiles by numerical simulations of sprays generated by a coaxial airblast atomizer. They used a two-way coupled Eulerian-Eulerian approach for their computations. Li et al. (2009) reported self-similar axial drop velocity profiles in a water spray generated by a plain-jet airblast atomizer. The measurements were taken at axial distances $16.8 < z/d_{or} < 33.3$ from the atomizer orifice. Leboucher et al. (2012) investigated sprays produced by air-assisted atomization of an annular liquid sheet. They reported self-similar mean axial drop velocity profiles at axial distances $z/d_{or} > 7.5$ from the orifice. The self-similar profile was well described by a Gaussian curve, similar to (2.24).

Spray flames

In spray flames, self-similar vapor source profiles and self-similar axial gas velocity profiles were reported by Karpetsis and Gomez (1998, 1999). The fuel was atomized with an ultrasonic nebulizer to avoid slip velocities between the droplets and the gas phase, and carried upwards by a co-flowing air stream. Once ignited, a flame extended from the atomizer tip through a circular contraction ($d_{or} = 12.5 \text{ mm}$) into the measurement region. As the spray flame exits the burner, the gas jet was accelerated due to the vaporization-induced volumetric dilatation, resulting in moderate slip velocities between the droplets and the gas.

Analyzing the axial evolution of the gas velocity, they identified three different spray regions. First, close to the burner exit, the gas was accelerated. Second, a self-similar region at $3 < z/d_{or} < 6.5$, where the gas velocity at the spray axis decreases with a power

law $u_0 \propto z^{-\kappa}$, was found. They obtained exponents between $0.26 \leq \kappa \leq 0.83$ in four sprays generated at different fuel and air mass flow rates. To make the axial gas velocities collapse to a universal self-similar profile, the self-similar coordinate had the same axial dependency as the gas velocity, i.e. $\eta = r_+/z^\kappa$. Note that the definition of the radial coordinate r_+ involves a Howarth transformation (Howarth 1948) to incorporate the gas density. This is not discussed here and can be found in the original paper (Karpetis and Gomez 1999). Third, farther downstream, a region comparable to the single-phase jet where $u_0 \propto z^{-1}$ was observed.

As mentioned earlier, in two of the spray flames self-similar vapor sources were obtained in a region $-1 < z/d_{or} < 6.5$. Depending on the spray, the axial decrease of the vapor source is represented by power laws $\propto z^{-3}$ and $\propto z^{-3.5}$, respectively. To make the measurement data collapse on a self-similar profile, they rescaled the self-similar coordinate to $\eta = r/z^{1.5}$ and $\eta = r/z^{1.75}$, respectively. Note that Karpetis and Gomez (1999) assumed the position of the virtual origin at the tip of the fuel injector ($z/d_{or} = -2$). This may explain the different axial scaling obtained for the self-similar coordinates to describe the self-similarity of the vapor source and the axial gas velocity.

Self-similar axial gas velocity profiles were reported by Russo and Gomez (2006) in buoyancy-dominated laminar spray flames and by Gounder et al. (2012) in turbulent piloted dilute spray flames. Kourmatzis et al. (2015) measured self-similar mean axial velocity profiles for two different drop size classes ($0 < d < 10 \mu\text{m}$ and $40 < d < 50 \mu\text{m}$) in non-reacting sprays and turbulent spray flames. In addition, they reported self-similar turbulence intensities deduced from the smallest droplets ($0 < d \leq 10 \mu\text{m}$).

Diesel sprays

In Diesel-type sprays, Wu et al. (1984) observed self-similar mean axial drop velocity profiles at large axial distances from the atomizer orifice ($300 < z/d_{or} < 800$). In this region of the spray, droplets and gas phase are in dynamic equilibrium, resulting in a similar scaling as observed for the single-phase jet. Similar results were obtained by Felton et al. (1988) by measurements in Diesel sprays in cross sections located at $200 < z/d_{or} < 650$. They observed a universal self-similar mean axial drop velocity profile for $z/d_{or} > 300$ and minor deviations from it for the drop velocities in cross sections at $z/d_{or} < 300$.

Payri et al. (2016) measured the drop velocity field of high-pressure Diesel sprays at varying ambient densities using particle image velocimetry (PIV) without additional seeding. They observed self-similar mean axial drop velocity profiles in cross sections between $503 < z/d_{or} < 727$ for all sprays investigated. For this purpose, the self-similar coordinate of the single-phase round jet was applied. Desantes et al. (2009) and García-Oliver et al. (2017) reported self-similar velocity profiles in inert and reacting Diesel

sprays. Additional studies on self-similar phenomena in Diesel sprays are discussed in section 2.3.2.

Modeling based on similarity assumptions

In the present section we discuss models describing aspects of spray flow, which are based on self-similar assumptions about the flow field. This excludes modeling of spray flow where the two phases are in dynamic equilibrium, which will be discussed in more detail in section 2.3.2. Yeung (1982) suggested the possibility of a mathematical description of a self-similar axisymmetric boundary-layer spray flow, but concluded that no mathematical solution for such a problem was possible. A self-similar description was derived for flat sprays based on the assumption that the droplet motion is not influenced by the gas velocity, i.e. the droplets travel on straight trajectories at a constant velocity.

Ghosh et al. (1991) and Ghosh and Hunt (1994) developed a one-dimensional model to describe the motion of gas flow in sprays induced by the droplets. They assumed that the droplets travel along straight trajectories, implying that the radial distance of the spray edge from the symmetry axis increases linearly with the axial coordinate. They obtained an axial scaling of the axial gas velocity $u \propto z^{-1/2}$ for the region in sprays with large slip velocities between the droplets and the air. Based on this result, they derived a self-similar description of the gas flow in axisymmetric sprays. In doing so, they applied Oseen's approximation (Oseen 1910) to neglect the contribution of the radial velocity component of the advective term in the momentum balance. From our understanding, this approximation is highly questionable, since Oseen's approximation is usually only applied to low Reynolds number flow, i.e. Stokes flow.

The assumption of self-similar flow fields was used in other modeling approaches. Cossali et al. (1996) measured the entrainment rate in the near field of transient Diesel sprays and obtained an axial scaling of the entrained mass flow rate $\dot{m} \propto z^{3/2}$. Assuming a self-similar flow field, similar to a single-phase jet, they calculated a linear increase of the gas-phase momentum flow rate. Based on similarity assumptions, Cossali (2001) developed a onedimensional model to predict the gas entrainment into non-evaporating full cone sprays. The obtained model is, on the one hand, able to predict the axial dependency of the entrained mass flow rate $\dot{m} \propto z^{3/2}$ in the near field measured by Cossali et al. (1996) and, on the other hand, describes its linear evolution, $\dot{m} \propto z$, in the far field.

Dynamical similarity

A recent study by Dhivyaraja et al. (2019) describes a phenomenon they termed as *dynamical similarity*. In fact, this does not represent self-similarity in the classical sense, but it implies the similarity of spray properties observed at given measurement positions

in different sprays. They showed dynamical similarity of the mean drop velocities, the Sauter mean drop diameters, the liquid volume fluxes and the probability density functions (PDF) of the droplet diameter in a given cross section at $z/d_{or} = 19$. The sprays were generated by pressure-swirl atomizers at a broad range of different flow conditions. They defined the similarity variable as the ratio of the local radial coordinate to the radial coordinate of the spray edge

$$\eta = \frac{r}{z \tan \theta_m}, \quad (2.25)$$

where θ_m denotes the cone half angle of the spray.

Dynamical similarity has been reported by others as well. For example, Moon et al. (2014) showed similarity of velocity profiles in two different cross sections in Diesel sprays generated at different injection pressures. Kobashi et al. (2018) reported dynamical similarity of axial velocity profiles and turbulence intensities in a given cross section in non-evaporating Diesel sprays. The sprays were generated at different ambient pressures.

Other self-similar spray flow

Here, we review studies on self-similar spray phenomena that did not fit into the previous categories. Panchagnula and Sojka (1999) reported self-similar mean axial drop velocity profiles in sprays produced by an effervescent atomizer. The self-similar velocity profile was described by an equation similar to (2.20). Soltani et al. (2005) observed areas with self-similar properties near the core region of sprays generated by coaxial liquid-liquid swirl atomization. There, they showed self-similar mean drop velocities and Sauter mean drop diameters. For this purpose they used the self-similar coordinate of the single phase jet. In medical sprays, Amili et al. (2015) reported self-similar axial velocity profiles in sprays generated by pressurized metered dose inhalers.

2.3.2 Modeling of equilibrium spray flow

In many of the studies on self-similar spray flow discussed in the previous section, the drops and the gas flow were in dynamic equilibrium with no, or negligible, slip velocity. This fact was used by some authors to model the spray flow as a single-phase jet with variable fluid density. For example, based on the assumption of locally homogeneous flow (LHF), assuming fast interphase transport rates in comparison to flow development as a whole, Shearer et al. (1979) found self-similar velocity profiles, with scaling variables similar to a single-phase jet, in evaporating sprays generated by twin-fluid atomization. Based on LHF assumptions, similar results were obtained by others (Faeth 1983), also in non-evaporating sprays (Solomon et al. 1985).

Desantes et al. (2011) developed a semi-empirical model based on similarity assumptions to describe the velocity and liquid concentration field of fully developed Diesel sprays. Their key assumption is negligible slip between the liquid and the gas phases. In the following, we will give an overview of their model. Note that several other publications are associated with this work, which are not discussed separately (Desantes et al. 2006a, 2006b, 2007; Payri et al. 2008; Benajes et al. 2016).

Based on experimental observations, Desantes et al. (2011) assumed self-similar Gaussian profiles for the axial velocity and the liquid fuel mass fraction

$$\bar{u}(r, z) = \bar{u}_0(z) \exp \left[-\tilde{\alpha} \left(\frac{r}{z \tan(\theta_u/2)} \right)^2 \right], \quad (2.26)$$

$$\bar{c}(r, z) = \bar{c}_0(z) \exp \left[-\tilde{\alpha} Sc_t \left(\frac{r}{z \tan(\theta_u/2)} \right)^2 \right], \quad (2.27)$$

where $\tilde{\alpha}$ is the shape factor of the Gaussian distribution, θ_u the cone half angle of the velocity field, and $\bar{u}_0(z)$ and $\bar{c}_0(z)$ the axial velocity and the liquid fuel mass fraction at the spray axis, respectively. The effective Schmidt number, Sc_t , includes molecular and turbulent contributions. The local fluid density reads

$$\bar{\rho}(r, z) = \frac{\rho_f}{\bar{c}(r, z)(1 - \rho_f/\rho_g) + \rho_f/\rho_g}, \quad (2.28)$$

where ρ_f and ρ_g denote fuel and air density, respectively. Conservation of the initial liquid momentum flow rate demands

$$\begin{aligned} \mathcal{I}_{or} = \mathcal{I}(z) &= 2\pi \int_{r=0}^{\infty} \bar{\rho}(r, z) \bar{u}^2(r, z) r \, dr = \\ &= 2\pi \rho_f \bar{u}_0^2(z) \int_{r=0}^{\infty} \frac{\exp \left[-2\tilde{\alpha} \left(\frac{r}{z \tan(\theta_u/2)} \right)^2 \right]}{\bar{c}_0(z) \left(1 - \frac{\rho_f}{\rho_g} \right) \exp \left[-\tilde{\alpha} Sc_t \left(\frac{r}{z \tan(\theta_u/2)} \right)^2 \right] + \frac{\rho_f}{\rho_g}} r \, dr. \end{aligned} \quad (2.29)$$

Evaluating the integral and simplifying the results, considering only values of $\tilde{\alpha}$ relevant for the application, (2.29) turns into (Desantes et al. 2007)

$$\mathcal{I}_{or} = \frac{\pi}{2\tilde{\alpha}} \rho_g \tan^2 \left(\frac{\theta_u}{2} \right) z^2 \bar{u}_0^2(z) \sum_{j=0}^{\infty} \frac{1}{1 + j Sc_t/2} \left[\bar{c}_0(z) \left(\frac{\rho_f - \rho_g}{\rho_f} \right) \right]^j. \quad (2.30)$$

This expression can be further simplified by the following relation between the axial velocity and the liquid fuel mass fraction at the spray axis (Desantes et al. 2006a)

$$\bar{c}_0(z) = \frac{(1 + Sc_t) \bar{u}_0(z)}{2 \bar{u}_{or}}, \quad (2.31)$$

yielding

$$\mathcal{I}_{or} = \frac{\pi}{2\tilde{\alpha}} \rho_g \tan^2 \left(\frac{\theta_u}{2} \right) z^2 \bar{u}_0^2(z) \sum_{j=0}^{\infty} \frac{1}{1 + j Sc_t/2} \left[\frac{\bar{u}_0(z) (1 + Sc_t)}{\bar{u}_{or} 2} \left(\frac{\rho_f - \rho_g}{\rho_f} \right) \right]^j. \quad (2.32)$$

Equation (2.32) relates the axial velocity decrease at the spray axis $\bar{u}_0(z)$ to the inlet conditions $(\mathcal{I}_{or}, \bar{u}_{or})$, the fluid properties (ρ_f, ρ_g) and other properties of the flow field $(\tilde{\alpha}, \theta_u, Sc_t)$. With these parameters and \bar{u}_0 known, using the relation (2.31), the velocity and fuel concentration fields, (2.26) and (2.27), in the fully developed region of Diesel-type sprays can be determined.

Chapter 3

Experiments

The analysis of pressure-atomized spray flow is based on measurement data acquired by means of an optical measurement technique. In this chapter, the atomizer used for spray generation, the experimental setup and the governing parameters of the experiments are introduced. Moreover, we discuss the optical measurement technique and the data analysis associated with it.

3.1 Experimental setup

Our investigation of consumer-type sprays is based on measurements using phase-Doppler anemometry (PDA). The experimental setup is schematically depicted in figure 3.1. The atomizer is mounted on a two-axis traverse system allowing for axial and radial navigation in the spray flow field. A pressurized tank supplies liquid at a constant volumetric flow rate. The sprayed liquid is captured by a ventilated spray box to avoid recirculation of drops to the measurement region.

A continuous Argon-ion laser (Coherent Innova 90-C3) serves as the light source for the PDA system (Dantec Dynamics). The transmitting optics focus two pairs of laser beams with wavelengths of 488 nm and 514.5 nm, respectively, in coinciding probe volumes. Drops passing the probe volume scatter light, detected by the receiving optics. The optical configuration of the PDA system is depicted in figure 3.2. The system is operated in first-order refraction mode detecting scattered light at a scattering angle of $\varphi = 50^\circ$. A PDA processor obtains electrical signals for the axial and radial velocity components, u_i and v_i , as well as the drop diameter d , for each drop from the optical signals received. Table 3.1 lists the geometrical parameters and the measuring ranges of the PDA system for all sprays investigated. The principles of phase-Doppler anemometry are discussed in section 3.2. The parameters of the sprays studied in the present work are introduced in section 3.3.

As indicated in figure 3.2, the sprays are assumed to be axially symmetric. Therefore, in each cross section, we place the measurement points on a single radial axis. We cover the half of this axis closer to the receiving optics (positive values of the radial

3 EXPERIMENTS

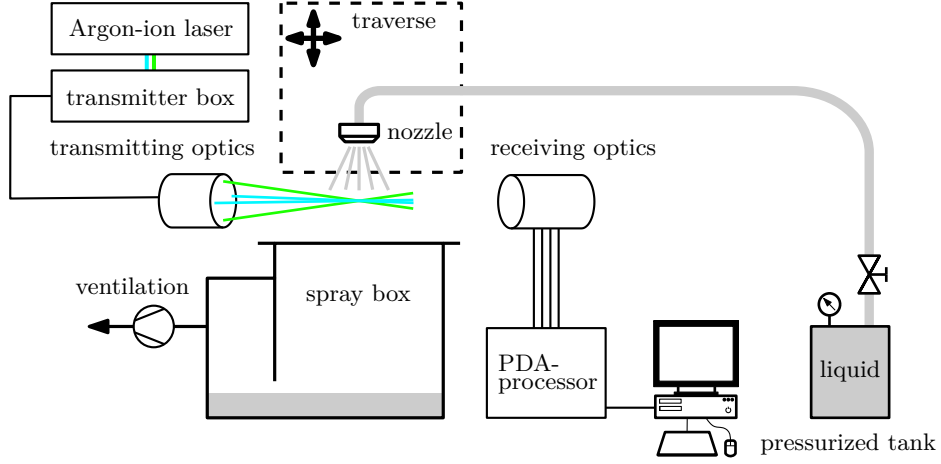


Figure 3.1: Illustration of the experimental setup.

PDA parameters		Spray 1	Spray 2	Spray 3
Scattering angle φ	[$^{\circ}$]	50	50	50
Beam half angle ϑ	[$^{\circ}$]	1.386	1.386	1.386
Phase factor P12	[$^{\circ}/\mu\text{m}$]	2.231	2.373	2.367
Phase factor P13	[$^{\circ}/\mu\text{m}$]	0.870	1.028	1.026
Measuring range d	[μm]	298	251	251
Measuring range u_t	[m/s]		-63.8 – 63.8	
Measuring range v_t	[m/s]		-20.2 – 20.2	

Table 3.1: Geometrical parameters and measuring ranges of the PDA system.

coordinate r , see figure 3.2) at a high spatial resolution. To verify the assumption of axisymmetry, we place less measurement points on the other half of the axis (negative values of r). The properties of 100,000 drops are measured at each sampling point to ensure high statistical reliability of the results, even for spectral spray properties in parts of the probability density function where the sample numbers are low. By virtue of the measurement technique, we defined the edge of the spray at the radial positions where the local frequency of drop detection was 5% of the maximum drop detection rate in the current cross section, or less than 300 Hz, to ensure a feasible duration of the measurements. Typical validation rates of the drop diameter between 60% and 85% were achieved. At measurement locations close to the orifice, with very high drop concentration, validation rates of 50% occurred. In these dense regions of the sprays, the single-particle constraint of PDA is violated at a higher probability than in more dilute regions. The validation rates of the drop velocity were, at every measurement

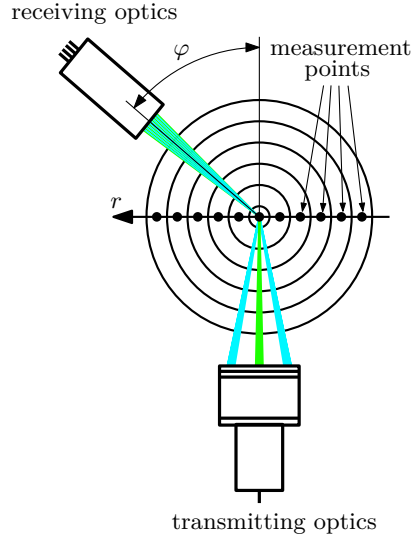


Figure 3.2: PDA optics with a spray cross section.

location, always larger than the validation rates of the drop diameter. The validation rates achieved are well in line with other studies in the literature, e.g. Jedelsky et al. (2018), and what can be reached in spray measurements by PDA as used in the present study.

To generate the sprays, we use a consumer-type single-phase pressure atomizer with off-axis liquid supply. The nozzle diameter is approximately $d_{or} = 0.4$ mm. Figure 3.3(a) shows a photograph of a meridional section of the atomizer, and figure 3.3(b) depicts a schematic illustration of the liquid flow through the atomizer. The liquid is ejected with an angular momentum due to the eccentric liquid feed. As a consequence, the resulting sprays show larger spray angles than observed for plain-orifice atomizers. Contrary to a classical pressure-swirl atomizer, a liquid swirl velocity inside the atomizer is not imprinted (Lefebvre and McDonell 2017). Therefore, the azimuthal velocity component of the liquid sheet emerging from the nozzle is much smaller than its axial velocity component. Structures on the liquid sheet, visualized with a high-speed camera (see figure 3.10), showed radial motion downstream. This endorses our assumption of negligible azimuthal droplet velocity. In fact, previous studies in the literature have shown that, even for pressure-swirl atomizers with significant azimuthal liquid motion inside the atomizer, the swirling flow is quickly converted into radial motion within small downstream distances from the atomizer (Schmidt et al. 1999; Vashahi and Lee 2018). The azimuthal velocity component of the resulting drops turned out to be negligible against their axial and radial velocity components (Dafsari et al. 2017; Jedelsky et al. 2018).

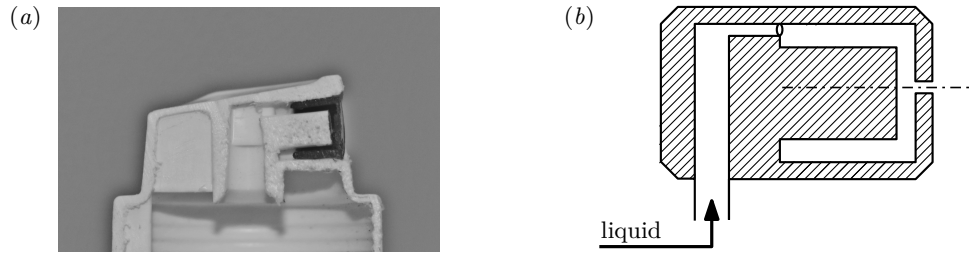


Figure 3.3: (a) Photograph of a meridional section of the atomizer and (b) the corresponding illustration of the liquid path through the atomizer.

3.2 Phase-Doppler anemometry

Phase-Doppler anemometry (PDA) is a non-intrusive optical measurement technique to measure the size and the velocity of spherical particles, especially of liquid droplets in spray flow. In this section, a review of the fundamentals of the phase-Doppler measurement technique is given. Furthermore, we introduce the procedure to obtain local, statistically representative results of directly measured quantities, i.e. the drop diameter and velocity, and indirectly measured quantities, such as the liquid mass and momentum fluxes as well as the spatial droplet concentration. Then, we define equations to globalize the local measurement data to quantities representative for entire cross-sectional areas of the sprays.

3.2.1 Fundamentals

The phase-Doppler measurement technique is based on the detection of light scattered from spherical particles. We introduce the principles by which the velocity and the size of the particles are measured. The overview given below is by no means exhaustive. The fundamentals of PDA and relevant aspects for the treatment of acquired measurement data are discussed. The technical design of phase-Doppler systems is not considered. Comprehensive reviews on the phase-Doppler technique can be found elsewhere, e.g. Albrecht et al. (2003).

Measurement of the particle velocity

The measurement of the particle velocity with PDA relies on the measurement technique called Laser-Doppler velocimetry (LDV). There are two concepts to explain the principle of LDV. On the one hand, it can be explained by the Doppler effect, where light scattered from a moving particle exhibits two shifts in its frequency as compared to the light emitted from the original light source (Durst et al. 1987; Albrecht et al. 2003). On the

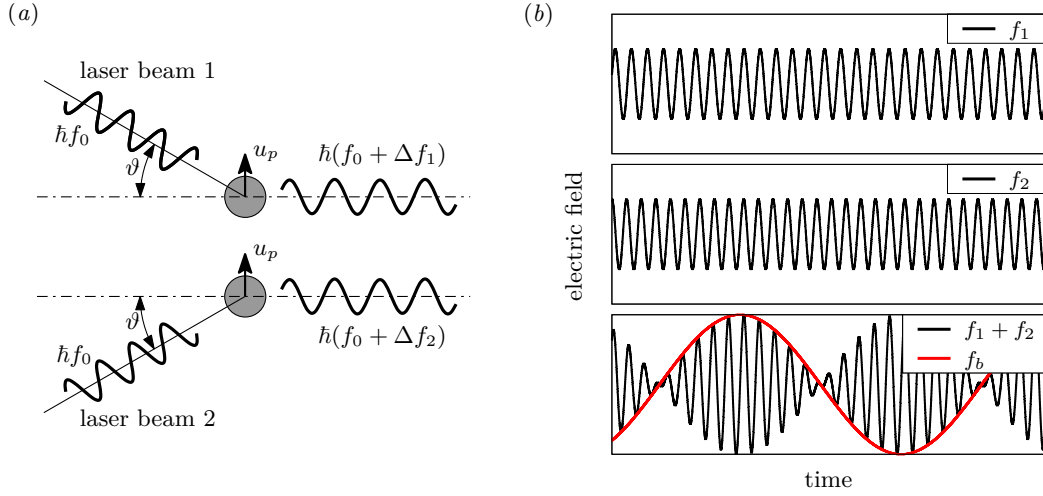


Figure 3.4: (a) Light scattered by a particle passing through the control volume of the two intersecting laser beams. (b) Doppler-shifted frequencies with $f_1 = f_0 + \Delta f_1$ (top) and $f_2 = f_0 + \Delta f_2$ (center). Superposition of the two signals yields the beat with the frequency f_b (bottom). \hbar denotes Planck's constant. The figure is adapted from Feldmann and Mayinger (2001).

other hand, it can be described by the fringe model, which is based on the interference patterns of two intersecting laser beams, producing bright and dark fringes (Rudd 1969; Durst et al. 1987).

In general, there are many different types of LDV systems (Feldmann and Mayinger 2001). For illustration purposes, we consider the dual-beam differential technique only. Two laser beams with the wavelength λ form a control volume by intersecting at the angle 2ϑ . Particles passing the control volume with a velocity u_p , as shown in figure 3.4(a) for both laser beams individually, scatter light which is detected by a photo detector. The scattered light is slightly shifted in frequency due to relative motion of the particle to the direction of laser beams (Doppler effect). With only one laser beam in place, the frequency shift is too small in front of the electric field frequencies to be resolved by a photo detector. Since the two laser beams are not parallel, the frequency shift is also slightly different for the light scattered from each laser beam. The superimposed Doppler shifted components result in a beat with a frequency f_b that can easily be detected. This is illustrated in figure 3.4(b). Using the wavelength of the original laser light, the intersection angle of the two laser beams and the beat frequency, the velocity component of the particle perpendicular to the symmetry axis between the two laser beams, and within the plane formed by the beams (see figure 3.4(a)), can be calculated by (Feldmann and Mayinger 2001)

$$u_p = \frac{\lambda f_b}{2 \sin \vartheta}. \quad (3.1)$$

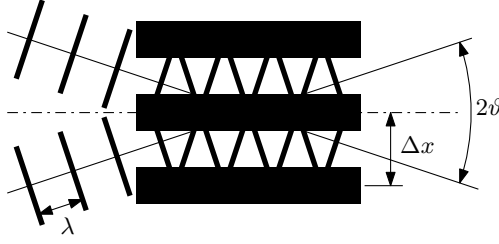


Figure 3.5: The illustration of the fringe model is adapted from Durst et al. (1987).

With the addition of a second pair of laser beams of different wavelength in a rotated plane in space, see figure 3.2, and a second photo detector, an additional velocity component in a second direction can be measured. The intersection angle of the laser beams, defined by the beam half angle, is equal for both pairs of laser beams in the present work and listed in table 3.1.

The principles of LDV can alternatively be explained by the fringe model, which is illustrated in figure 3.5. Two coherent laser beams with wavelength λ intersect at the angle of 2ϑ . Within the created measurement volume, an interference pattern of bright and dark fringes emerges. The bright fringes are illustrated by the black horizontal rectangles in figure 3.5. The fringe spacing Δx depends on the wavelength of the laser light λ and the beam half angle ϑ and can be calculated by (Durst et al. 1987)

$$\Delta x = \frac{\lambda}{2 \sin \vartheta}. \quad (3.2)$$

The intensity of the light scattered by a particle traveling through the measurement volume varies according to the intensity distribution in the fringe pattern. The frequency of the detected signal depends on the velocity of the particle normal to the fringes, and within the plane formed by the two laser beams, and the fringe spacing, resulting in the same expression for the particle velocity as given in (3.1).

Measurement of the particle diameter

Compared to LDV, phase-Doppler anemometry includes the measurement of the particle diameter in addition to the measurement of the particle velocity. The measurement principle is based on the phase of the scattered light emitted from the particle passing the measurement volume. With two detectors at different known locations, a phase shift of the scattered light of a given particle can be measured. The phase shift corresponds to the curvature of the particle's surface, which in case of spherical particles yields the particle size. Durst and Zaré (1975) were the first to show that this phase shift scales linearly with the particle diameter.

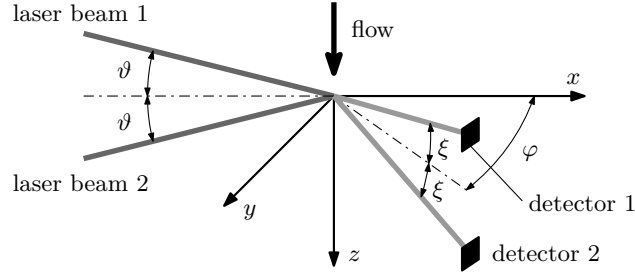


Figure 3.6: Illustration of the detector arrangement in PDA systems (adapted from Albrecht et al. 2003).

Figure 3.6 illustrates the basic arrangement and the detector locations of a PDA system, operated in first-order refraction mode. The laser beams propagate within the (x, z) plane and intersect at the focal point with the angle 2ϑ . The detection optics is placed in the scattering plane (x, y) and rotated by the scattering angle φ with respect to the z axis. The two detectors required to measure the phase shift of the scattered light are elevated and lowered with respect to the scattering plane by the elevation angle ξ . For first-order refraction, the detected phase shift $\Delta\Phi$ relates to the particle diameter d_p as per (Albrecht et al. 2003)

$$\Delta\Phi = \frac{-2\pi d_p}{\lambda} \frac{m \sin \vartheta \sin \xi}{\left[2(1+q) \left(1+m^2 - m\sqrt{2(1+q)}\right)\right]^{1/2}}, \quad (3.3)$$

where

$$q = \cos \vartheta \cos \xi \cos \varphi. \quad (3.4)$$

The relative refractive index is denoted by m .

Since the particle diameter can be determined unambiguously only for a phase shift between 0 and 2π , there is a tradeoff between accuracy and measurable diameter range. For this reason, usually a third detector is added to the PDA system (Albrecht et al. 2003). In this way, the phase shift between the first and the third detector covers a wide diameter range, but at low accuracy. With knowledge of the approximate particle diameter, the 2π ambiguity of the phase shift between the first and the second detector can be overcome, allowing for an accurate determination of the particle diameter.

Particle-size dependent detection area

The measurement volume in PDA is created by the intersection of two coherent laser beams. At small beam half angles ϑ , the measurement volume is long and shaped like a

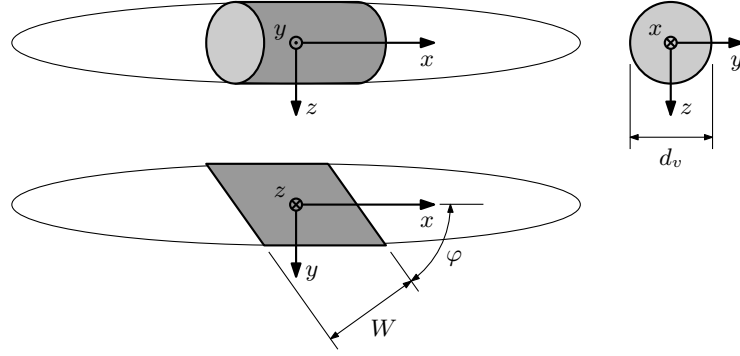


Figure 3.7: Illustration of the PDA measurement volume adapted from Zhang and Ziada (2000).

cigar. From this cigar-shaped measurement volume, the receiving optics (see figure 3.2) only detect scattered light from a well-defined portion due to a slit orifice in front of the aperture of the receiving optics. This is illustrated in figure 3.7, where the slit width is denoted by W . The resulting measurement volume is assumed to be of cylindrical shape with oblique ellipsoidal faces. The slit width of the PDA system used in the present study is $W = 100 \mu\text{m}$.

The length of the measurement volume is determined by the image slit width W and the scattering angle φ . Despite reports on a particle-size dependent slit effect (Albrecht et al. 2003), the length of the measurement volume is assumed to be uniform for all drop sizes in the present study. The effective cross section of the measurement volume, represented by its diameter d_v , however, varies with the size of the particle. The reason for this phenomenon can be explained by the radial Gaussian distribution of the light intensity of the laser beams. As a consequence, the probe volume also exhibits a radial intensity distribution. Particles passing the probe volume close to its axis (represented by the x axis in figure 3.7) scatter more light with more intensity than particles passing it at a larger distance. In addition, the light scattered by large particles is more intense compared to smaller particles because of their larger surface area. Since particles are only detected when the optical power of the scattered light exceeds the detection threshold of the photo detectors, the radial distance from the probe volume axis to the location where this threshold is reached determines the particle-size dependent probe volume diameter. This effect results in an underrepresentation of smaller particles in the local ensemble which has to be accounted for. The correction of the local measurement results due to the particle-size dependent detection area is often referred to as the *Saffman correction* (Saffman 1987). Its application in the present study is discussed below.

To determine the measures required to correct for the particle-size dependent detection area, the effective probe-volume cross section for each particle size class in the local ensemble has to be determined. The length of the trajectory through the probe volume

of a given particle, with the diameter d_p and the velocity w_p , can be calculated by

$$\ell_p = w_p \tau_p, \quad (3.5)$$

where τ_p denotes the transit time of the particle through the probe volume measured by the PDA system. Drops with the longest trajectories are assumed to cross the probe volume very close to the axis. Therefore, the lengths of their trajectories represent the probe volume diameter of particles with the same size. At a given particle size, the probe volume diameter can be determined by the longest trajectory of particles with similar size in the local ensemble

$$d_v(d_p) = \max(\ell_p(d_p)). \quad (3.6)$$

In practice, we do not use the longest trajectory, but the mean of the longest 5% of all trajectories at the considered particle size. Note that the obtained values of $d_v(d_p)$ may be inaccurate for particle sizes, where the number of particles in the local ensemble is low. This is usually the case for large particles. This fact is taken into account as follows. It has been shown, that the diameter of the local probe volume cross section follows in general the trend given by (Albrecht et al. 2003; Wimmer 2012)

$$d_v(d_p) = B_1 \sqrt{B_2 d_p^2}, \quad (3.7)$$

where the two independent parameters B_1 and B_2 can be determined by best fit. For the fitting process, only particles sizes with a sufficiently large number of particles are considered. Using (3.6) and (3.7), the effective particle-size dependent probe volume cross section follows from geometrical considerations, see figure 3.7, by (Zhang and Ziada 2000)

$$A_p(d_p) = \frac{d_v(d_p)W}{\sin \varphi} + \frac{d_v^2(d_p)\pi}{4} \frac{|\bar{v}_p(d_p)|}{\bar{w}_p(d_p) \tan \varphi}, \quad (3.8)$$

where $\bar{v}_p(d_p)$ is the mean velocity component in y direction of particles with diameter d_p and $\bar{w}_p(d_p)$ denotes the mean total particle velocity of particles with diameter d_p . The Saffman correction can now be applied to each particle size in the local ensemble by

$$\hat{n}(d_p) = n(d_p) \frac{\max(A_p)}{A_p(d_p)}, \quad (3.9)$$

where $n(d_p)$ is the number of particles with diameter d_p detected, and $\hat{n}(d_p)$ is the Saffman-corrected number of particles with that size.

For the calculation of liquid mass and momentum fluxes from PDA measurements, the particle-size dependent probe volume cross sections in the radial and axial directions are required. They can be calculated by (Dantec Dynamics 2002)

$$A_r(d_p) = \frac{d_v(d_p)W}{\sin \varphi} + \frac{d_v^2(d_p)\pi}{4 \tan \varphi} \quad \text{and} \quad (3.10)$$

$$A_z(d_p) = \frac{d_v(d_p)W}{\sin \varphi}, \quad (3.11)$$

respectively. In the present PDA system, the radial direction (see figure 3.2) corresponds to the y axis in figure 3.7. To calculate the area of the probe-volume cross section corresponding to arbitrary particle trajectory inclination angles γ_p (see (3.14) below), we use the simple relation proposed by Dantec Dynamics (2002)

$$A(d_p, \gamma_p) = \left(1 - \frac{2\gamma_p}{\pi}\right) A_z(d_p) + \frac{2\gamma_p}{\pi} A_r(d_p). \quad (3.12)$$

3.2.2 Local spray characteristics

PDA measurements provide local information on the size and dynamics of individual drops passing the measurement volume. A PDA system operated with two pairs of laser beams of different wavelengths, as used in the present work, see figure 3.2, measures the drop velocity components in the axial and radial directions, u_l and v_l , as well as the drop diameter d . Assuming axial symmetry of the spray flow, with negligible azimuthal velocity component of individual droplets, the total drop velocity

$$w_l = \left(u_l^2 + v_l^2\right)^{1/2} \quad (3.13)$$

and the trajectory inclination angle of the drop

$$\tan \gamma = \frac{v_l}{u_l} \quad (3.14)$$

can be calculated. In addition, PDA measurements provide the transit time τ_l of each drop passing the measurement volume.

Figure 3.8 shows the measured properties of 100,000 drops at a single measurement position, typical for the sprays investigated in the present study. The diagram represents a so-called scatter plot, where each data point represents one drop with velocity w_l and diameter d . For statistical analysis, local measurement results are represented as number-based histograms showing the number of droplets exhibiting a certain property. For this purpose, the measurement results are classified into classes, with the desired quantity associated. Table 3.2 lists the different classes utilized for the computation of

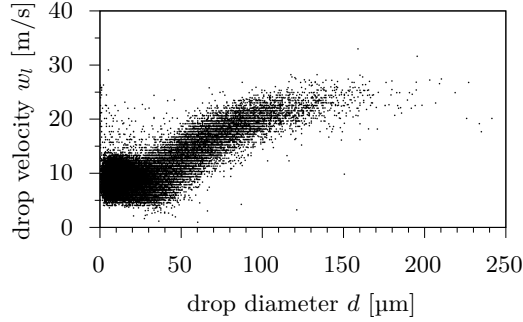


Figure 3.8: Scatter plot of a typical drop diameter-velocity correlation.

Class	Index	Range	Width Δ	Mean	Number
d	\underline{d}	0 to 300 μm	5 μm	\underline{d}_d	$\underline{D} = 60$
u_l	\underline{u}	-10 m/s to 50 m/s	1 m/s	$\underline{u}_{l,\underline{u}}$	$\underline{U} = 60$
v_l	\underline{v}	-20 m/s to 20 m/s	0.5 m/s	$\underline{v}_{l,\underline{v}}$	$\underline{V} = 80$
w_l	\underline{w}	-10 m/s to 50 m/s	1 m/s	$\underline{w}_{l,\underline{w}}$	$\underline{W} = 60$
γ	$\underline{\gamma}$	$-\pi/2$ rad to $\pi/2$ rad	$\pi/60$ rad	$\underline{\gamma}_\gamma$	$\underline{\Gamma} = 60$

Table 3.2: Size classes for statistical evaluation of the measurement data.

spray characteristics in the present study together with their ranges and widths. The number of drops in all size classes must yield the total number N of drops measured at the present location. For example,

$$\sum_{\underline{d}=1}^{\underline{D}} n_{\underline{d}} = N, \quad (3.15)$$

where $n_{\underline{d}}$ is the number of drops in size class \underline{d}_d . The droplets can also be classified with respect to more than one quantity. For example, $n_{\underline{uv}}$ represents the number of drops in the axial velocity class $\underline{u}_{l,\underline{u}}$ with the radial velocity $\underline{v}_{l,\underline{v}}$. Again, summation over both classes must yield the total number of drops detected

$$\sum_{\underline{u}=1}^{\underline{U}} \sum_{\underline{v}=1}^{\underline{V}} n_{\underline{uv}} = N. \quad (3.16)$$

Discretizing the measurement data of figure 3.8 into classes of the drop diameter \underline{d}_d , counting the number of drops with a diameter between $\underline{d}_d - \Delta d/2$ and $\underline{d}_d + \Delta d/2$, yields the number of drops $n_{\underline{d}}$ in each size class \underline{d}_d , as shown by the number-based histogram in figure 3.9(a). To obtain a representation which is comparable between different

measurements, the ordinate values in the number-based histogram are normalized to express the data in the form of a probability density function (PDF). For this purpose, the number of drops in each size class is divided by the total number of drops in the local ensemble and the width of the size class, such that the integral of the PDF equals unity. The number-based PDF for the drop diameter $\text{pdf}(d)$ is calculated by

$$\text{pdf}(d) = \frac{\hat{n}_d}{\Delta d \sum_{d=1}^D \hat{n}_d} . \quad (3.17)$$

and can be seen in figure 3.9(b). \hat{n}_d denotes the Saffman-corrected number of drops in drop size class d_d (see section 3.2.1). Similarly, the probability density functions of the local axial and radial velocity components read

$$\text{pdf}(u_l) = \frac{\hat{n}_u}{\Delta u_l \sum_{u=1}^U \hat{n}_u} \quad \text{and} \quad \text{pdf}(v_l) = \frac{\hat{n}_v}{\Delta v_l \sum_{v=1}^V \hat{n}_v} . \quad (3.18)$$

For an infinitely large sample size, the relative frequencies in a histogram converge to a PDF as the size class width goes to zero.

Other representative local spray characteristics of interest are mean values of the drop velocity and the drop diameter. The most commonly reported mean drop diameters are the number-mean drop diameter D_{10} and the Sauter mean drop diameter D_{32} . The latter is the ratio of the total droplet volume to the total droplet surface area in the ensemble. Their definitions are given by

$$D_{10} = \frac{\sum_{d=1}^D \hat{n}_d d_d}{\sum_{d=1}^D \hat{n}_d} \quad \text{and} \quad D_{32} = \frac{\sum_{d=1}^D \hat{n}_d d_d^3}{\sum_{d=1}^D \hat{n}_d d_d^2} . \quad (3.19)$$

To determine the scatter in a set of given values, the standard deviation (STD) may be used. It represents the root of the squared deviation of a given variable from the number-mean. The standard deviation of the drop diameter $\text{std}(d)$ from its mean value D_{10} is given by

$$\text{std}(d) = \left[\frac{\sum_{d=1}^D \hat{n}_d (d_d - D_{10})^2}{\sum_{d=1}^D \hat{n}_d - 1} \right]^{1/2} . \quad (3.20)$$

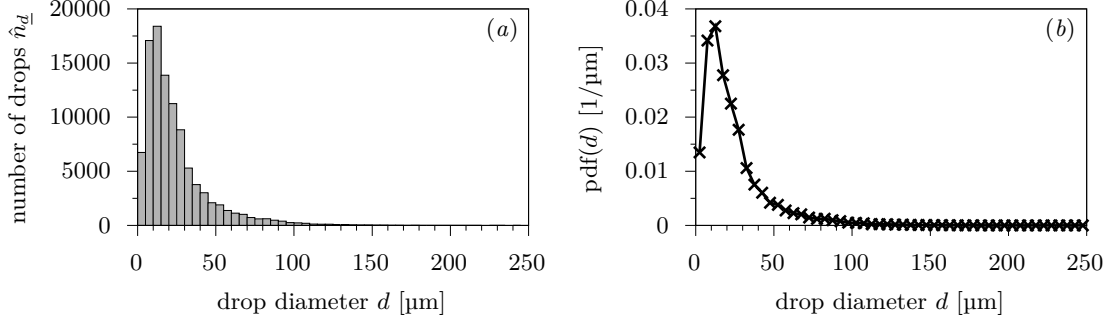


Figure 3.9: (a) Typical drop-size histogram and (b) the corresponding probability density function. The data corresponds to the measurements shown in figure 3.8.

Similar to the number-mean drop diameter D_{10} , see (3.19), the number mean axial and radial drop velocity components \bar{u}_l and \bar{v}_l are obtained by

$$\bar{u}_l = \frac{\sum_{\underline{u}=1}^U \hat{n}_{\underline{u}} u_{l,\underline{u}}}{\sum_{\underline{u}=1}^U \hat{n}_{\underline{u}}} \quad \text{and} \quad \bar{v}_l = \frac{\sum_{\underline{v}=1}^V \hat{n}_{\underline{v}} v_{l,\underline{v}}}{\sum_{\underline{v}=1}^V \hat{n}_{\underline{v}}}, \quad (3.21)$$

respectively. The standard deviations of these two velocity components read

$$\text{std}(u_l) = \left[\frac{\sum_{\underline{u}=1}^U \hat{n}_{\underline{u}} (u_{l,\underline{u}} - \bar{u}_l)^2}{\sum_{\underline{u}=1}^U \hat{n}_{\underline{u}} - 1} \right]^{1/2} \quad \text{and} \quad (3.22)$$

$$\text{std}(v_l) = \left[\frac{\sum_{\underline{v}=1}^V \hat{n}_{\underline{v}} (v_{l,\underline{v}} - \bar{v}_l)^2}{\sum_{\underline{v}=1}^V \hat{n}_{\underline{v}} - 1} \right]^{1/2}. \quad (3.23)$$

From the PDA measurement data, local fluxes, such as liquid mass and momentum fluxes, and the local drop concentration can be calculated. The following equations (3.24) to (3.32) are derived from the works of Dantec Dynamics (2002), Albrecht et al. (2003) and Wimmer (2012). We define the local drop number flux in drop size class $d_{\underline{d}}$, with the trajectory $\gamma_{\underline{d}}$, as

$$\psi_{d_{\underline{d}}} = \frac{n_{d_{\underline{d}}}}{\Delta t \theta_d A_{d_{\underline{d}}}}. \quad (3.24)$$

Here, $n_{d\underline{\gamma}}$ is the number of drops in drop size class $d_{\underline{d}}$ with the trajectory $\gamma_{\underline{\gamma}}$, Δt denotes the local measuring time, θ_d is the local validation rate of the drop diameter and $A_{d\underline{\gamma}}$ represents the Saffman-corrected effective probe-volume cross section for the drop size class $d_{\underline{d}}$ with the trajectory $\gamma_{\underline{\gamma}}$. The local droplet number fluxes in the axial and radial directions are calculated by

$$\psi_z = \frac{1}{\Delta t \theta_d} \sum_{\underline{d}=1}^D \sum_{\underline{\gamma}=1}^{\Gamma} \frac{n_{d\underline{\gamma}} \cos \gamma_{\underline{\gamma}}}{A_{z,\underline{d}}} \quad \text{and} \quad \psi_r = \frac{1}{\Delta t \theta_d} \sum_{\underline{d}=1}^D \sum_{\underline{\gamma}=1}^{\Gamma} \frac{n_{d\underline{\gamma}} \sin \gamma_{\underline{\gamma}}}{A_{r,\underline{d}}}, \quad (3.25)$$

where $A_{z,\underline{d}}$ and $A_{r,\underline{d}}$ are the Saffman-corrected effective probe-volume cross sections of the drop size class $d_{\underline{d}}$ in the axial and radial directions, respectively. Introducing the droplet mass into (3.25) yields the local axial and radial liquid mass fluxes

$$\phi_z = \frac{\pi \rho_l}{6 \Delta t \theta_d} \sum_{\underline{d}=1}^D \sum_{\underline{\gamma}=1}^{\Gamma} \frac{d_{\underline{d}}^3 n_{d\underline{\gamma}} \cos \gamma_{\underline{\gamma}}}{A_{z,\underline{d}}} \quad \text{and} \quad (3.26)$$

$$\phi_r = \frac{\pi \rho_l}{6 \Delta t \theta_d} \sum_{\underline{d}=1}^D \sum_{\underline{\gamma}=1}^{\Gamma} \frac{d_{\underline{d}}^3 n_{d\underline{\gamma}} \sin \gamma_{\underline{\gamma}}}{A_{r,\underline{d}}}. \quad (3.27)$$

The local liquid momentum fluxes in the axial and radial directions are calculated by

$$\Phi_z = \frac{\pi \rho_l}{6 \Delta t \theta_d} \sum_{\underline{d}=1}^D \sum_{\underline{u}=1}^U \frac{d_{\underline{d}}^3 n_{d\underline{u}} u_{l,\underline{u}}}{A_{z,\underline{d}}} \quad \text{and} \quad (3.28)$$

$$\Phi_r = \frac{\pi \rho_l}{6 \Delta t \theta_d} \sum_{\underline{d}=1}^D \sum_{\underline{v}=1}^V \frac{d_{\underline{d}}^3 n_{d\underline{v}} v_{l,\underline{v}}}{A_{r,\underline{d}}}. \quad (3.29)$$

Here, $n_{d\underline{u}}$ and $n_{d\underline{v}}$ represent the numbers of drops in drop size class $d_{\underline{d}}$ with the axial and radial drop velocity components $u_{l,\underline{u}}$ and $v_{l,\underline{v}}$, respectively.

Local drop-number and liquid-mass concentrations can be calculated from PDA data as well. The local drop-number concentration in drop size class $d_{\underline{d}}$ is obtained by

$$c_{n,\underline{d}} = \frac{1}{\Delta t \theta_d} \sum_{\underline{w}=1}^W \sum_{\underline{\gamma}=1}^{\Gamma} \frac{n_{d\underline{w}\underline{\gamma}}}{w_{l,\underline{w}} A_{d\underline{w}\underline{\gamma}}}, \quad (3.30)$$

where $n_{d\underline{w}\underline{\gamma}}$ is the number of drops in drop size class $d_{\underline{d}}$ with the velocity $w_{l,\underline{w}}$ and the trajectory $\gamma_{\underline{\gamma}}$. $A_{d\underline{w}\underline{\gamma}}$ represents the corresponding Saffman-corrected effective probe-

volume cross section. Summation of the drop concentrations in all drop size classes yields the total local drop-number concentration

$$c_n = \sum_{\underline{d}=1}^D c_{n,\underline{d}}. \quad (3.31)$$

The local concentration of liquid mass is obtained by

$$c_l = \frac{\pi\rho_l}{6} \sum_{\underline{d}=1}^D d_{\underline{d}}^3 c_{n,\underline{d}}. \quad (3.32)$$

3.2.3 Global spray characteristics

Spray characteristics representative for an entire spray cross section are called global spray characteristics. To calculate global spray characteristics, the local spray parameters introduced in section 3.2.2 are taken into account by multiplication with two weighting factors. These weighting factors are the size of the local annular cross-sectional area $A_m(r_i)$ of the spray and the local drop number flux $\psi_{\underline{d}}(r_i)$ in drop size class $d_{\underline{d}}$. With uniform radial spacing Δr between radial measurement locations r_i , the size of the annular cross-sectional area $A_m(r_i)$ can be calculated by

$$A_m(r_i) = \begin{cases} \Delta r^2 \pi / 4 & \text{if } r_i = 0 \\ \Delta r \pi r_i & \text{otherwise} \end{cases}. \quad (3.33)$$

The local drop number flux in drop size class $d_{\underline{d}}$ can be obtained from (3.24) as

$$\psi_{\underline{d}} = \sum_{\gamma=1}^{\Gamma} \psi_{\underline{d}\gamma}. \quad (3.34)$$

To ensure reliable global results, a sufficient radial resolution of the measurement points r_i is required. Moreover, if possible, measurement points must cover the radial axis up to the edge of the spray in order to minimize the liquid mass systematically overlooked at large radial distance from the spray axis.

Below, the equations to calculate global spray characteristics related to the drop diameter are introduced. These are the global number-based PDF of the drop diameter $\overline{\text{pdf}(\underline{d})}$, the global number-mean drop diameter \overline{D}_{10} and the global Sauter mean drop diameter \overline{D}_{32} . The following equations (3.35) to (3.37) are derived from Wimmer (2012).

The global number-based probability density function of the drop diameter reads

$$\overline{\text{pdf}(d)} = \frac{\sum_{i=1}^I \psi_{\underline{d}}(r_i) A_m(r_i)}{\Delta d \sum_{i=1}^I \sum_{\underline{d}=1}^D \psi_{\underline{d}}(r_i) A_m(r_i)}, \quad (3.35)$$

where I is the number of radial measurement locations. The global number-mean and Sauter mean drop diameters are calculated by

$$\overline{D_{10}} = \frac{\sum_{i=1}^I \sum_{\underline{d}=1}^D d_{\underline{d}} \psi_{\underline{d}}(r_i) A_m(r_i)}{\sum_{i=1}^I \sum_{\underline{d}=1}^D \psi_{\underline{d}}(r_i) A_m(r_i)} \quad \text{and} \quad \overline{D_{32}} = \frac{\sum_{i=1}^I \sum_{\underline{d}=1}^D d_{\underline{d}}^3 \psi_{\underline{d}}(r_i) A_m(r_i)}{\sum_{i=1}^I \sum_{\underline{d}=1}^D d_{\underline{d}}^2 \psi_{\underline{d}}(r_i) A_m(r_i)}, \quad (3.36)$$

respectively, where the spray cross-sectional area representative for each radial measurement location $A_m(r_i)$ is defined by (3.33). The global standard deviation of the drop diameter reads as follows

$$\overline{\text{std}(d)} = \left[\frac{\sum_{i=1}^I \sum_{\underline{d}=1}^D \psi_{\underline{d}}(r_i) A_m(r_i) (d_{\underline{d}} - \overline{D_{10}})^2}{\sum_{i=1}^I \sum_{\underline{d}=1}^D \psi_{\underline{d}}(r_i) A_m(r_i) - 1} \right]^{1/2}. \quad (3.37)$$

Global means of the drop velocities u_l and v_l can be calculated similar as in equations (3.35) to (3.37) shown above.

3.3 Performed experiments

The process of single-phase liquid atomization in a stagnant gaseous environment is governed by five parameters. These are the characteristic liquid velocity through the atomizer \bar{u}_{or} , a characteristic length scale of the atomizer d_{or} and the relevant liquid fluid properties, namely the liquid density ρ_l , the liquid dynamic viscosity μ_l and the liquid surface tension against the ambient gaseous medium σ . The characteristic velocity \bar{u}_{or} follows from the liquid mass flow rate through the atomizer $\dot{m}_{l,exp}$, the liquid density and the characteristic cross-sectional area $d_{or}^2 \pi / 4$ of the nozzle. These five parameters, with three basic dimensions involved, are represented by two nondimensional groups

$$We_l = \frac{\rho_l d_{or} \bar{u}_{or}^2}{\sigma} \quad \text{and} \quad Oh_l = \frac{\mu_l}{(\rho_l \sigma d_{or})^{1/2}}. \quad (3.38)$$

		Spray 1	Spray 2	Spray 3
Liquid mass flow rate $\dot{m}_{l,exp}$	[g/s]	2.00	2.92	2.45
Density ρ_l	[kg/m ³]	998.2	998.2	981.7
Dynamic viscosity μ_l	[mPa s]	1.00	1.00	1.40
Surface tension against air σ	[mN/m]	72.8	72.8	51.3
Weber number We_l		1395	2974	2921
Ohnesorge number Oh_l		0.0059	0.0059	0.0099
Location of measurement planes z/d_{or}		38 – 375	38 – 450	38 – 625

Table 3.3: Parameters of the performed experiments. The values of the fluid properties are taken from Khattab et al. (2012) at a temperature of 20 °C.

These two nondimensional numbers, called the Weber and the Ohnesorge numbers, determine the atomization process and its result. Their values are used for setting the properties of the spraying process in the experiments. The state of the ambient air is not varied and therefore not represented.

In the present work, we investigate three sprays with different pairs of Weber and Ohnesorge numbers. Henceforth, they will be referred to as spray 1, spray 2 and spray 3. To obtain different pairs of characteristic nondimensional numbers (3.38), we vary the liquid mass flow rate through the atomizer and use two different liquids with distinct fluid properties. Table 3.3 lists the experimental parameters, fluid properties and nondimensional numbers of the three sprays investigated. The liquid mass flow rates are of the order of magnitude as observed in commercial consumer sprays.

In sprays 1 and 2, demineralized water is used as the test liquid, resulting in equal Ohnesorge numbers of both sprays. Spray 2 has a larger Weber number since it is operated at an approximately 50 % higher liquid mass flow rate. The test liquid of spray 3 is an aqueous ethanol solution with an ethanol content of 10 mass percent. Accordingly, the Ohnesorge number of spray 3 exceeds the ones of the other two sprays. The liquid mass flow rate of spray 3 is chosen such that its Weber number is approximately equal to the Weber number of spray 2. Depending on the spray, measurements were carried out in 10 to 13 cross sections downstream from the nozzle exit (see table 3.3). These cross sections are located in regions of the sprays dominated by large slip velocity between the liquid and the gas phases. All experiments were carried out in atmospheric air at temperatures of 20 ± 1 °C.

Figure 3.10 depicts instantaneous photographs of the three sprays in a region close to the orifice to illustrate the atomization process. In all three cases, an annular liquid sheet emerges from the orifice. In spray 1, the sheet does not open as wide as in the other two sprays. Due to their motion relative to the ambient gas phase, the sheets are subject to Kelvin-Helmholtz instabilities (Schmidt et al. 1999). The nonlinear growth of

3 EXPERIMENTS

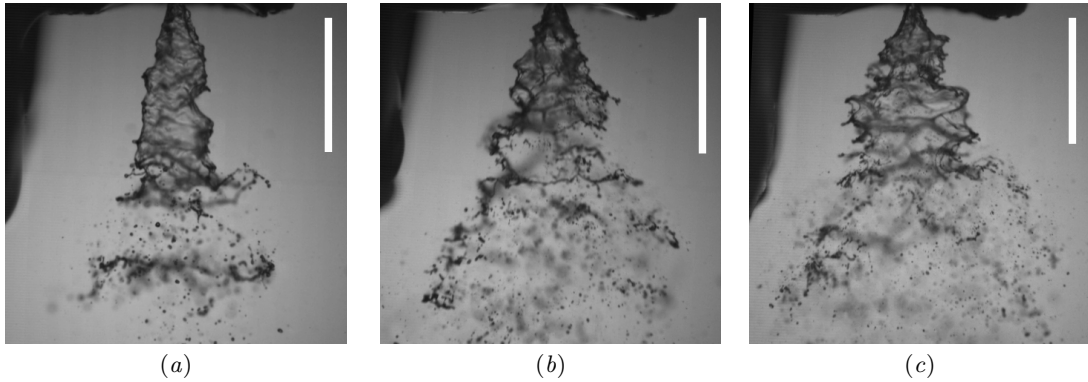


Figure 3.10: Instantaneous photographs of the liquid sheet emerging from the orifice in (a) spray 1, (b) spray 2 and (c) spray 3. The images were acquired with a high-speed camera at 10,000 frames per second, with an exposure time of $307,000^{-1}$ s. The white vertical bar corresponds to a length of 5 mm.

these instabilities causes local thinning of the sheets and their subsequent disintegration into ligaments and droplets. The ligaments themselves are Rayleigh-Taylor and Plateau-Rayleigh unstable. The droplets formed are much faster than the stagnant ambient gas phase and induce the motion of the gas phase. The investigation of this region with large slip velocities between the droplets and the gas is the subject of the present study.

Chapter 4

Measurement results

In this chapter, we present the results of the measurements defined in table 3.3. Section 4.1 discusses the results of the liquid-phase flow field, as measured by phase-Doppler anemometry. The procedure to determine the velocity components of the gas-phase flow field from PDA measurement data, as well as the corresponding results, are introduced in section 4.2.

4.1 Flow field of the liquid phase

The measured characteristics of the droplets are presented and discussed. First, we introduce radial profiles of local variables, computed according to the equations defined in section 3.2.2. Then, we discuss global spray characteristics, as derived in section 3.2.3.

4.1.1 Local spray characteristics

Figures 4.1 to 4.6 depict the local results of the liquid-phase flow field. In these figures, the results are shown from top to bottom for the sprays 1, 2 and 3. Figures 4.1(*a,c,e*) depict the local drop detection rate and (*b,d,f*) the drop diameter validation rate θ_d , as reported by the PDA system. For all three sprays, the frequency of drop detection has a maximum at the spray axis. The profiles decrease radially outwards and along the spray axis with increasing distance from the orifice. The radial positions of the edges of the profiles indicate a stronger radial expansion in sprays 2 and 3 as compared to spray 1. The validation rate of the drop diameter typically ranges between 60% and 85%, see figures 4.1(*b,d,f*). At measurement positions very close to the orifice, validation rates approximately as low as 50% occurred. In this dense region of the sprays, the single-particle constraint and the sphericity constraint of the PDA system are violated at higher probability than in more dilute regions of the sprays farther downstream. The validation rate of the drop diameter θ_d is an important parameter in the calculation of the local drop number flux (3.24).

Figures 4.2(*a,c,e*) show the profiles of the number-mean drop diameter D_{10} . In all three sprays, the number-mean drop diameter is smallest at the spray axis and increases

4 MEASUREMENT RESULTS

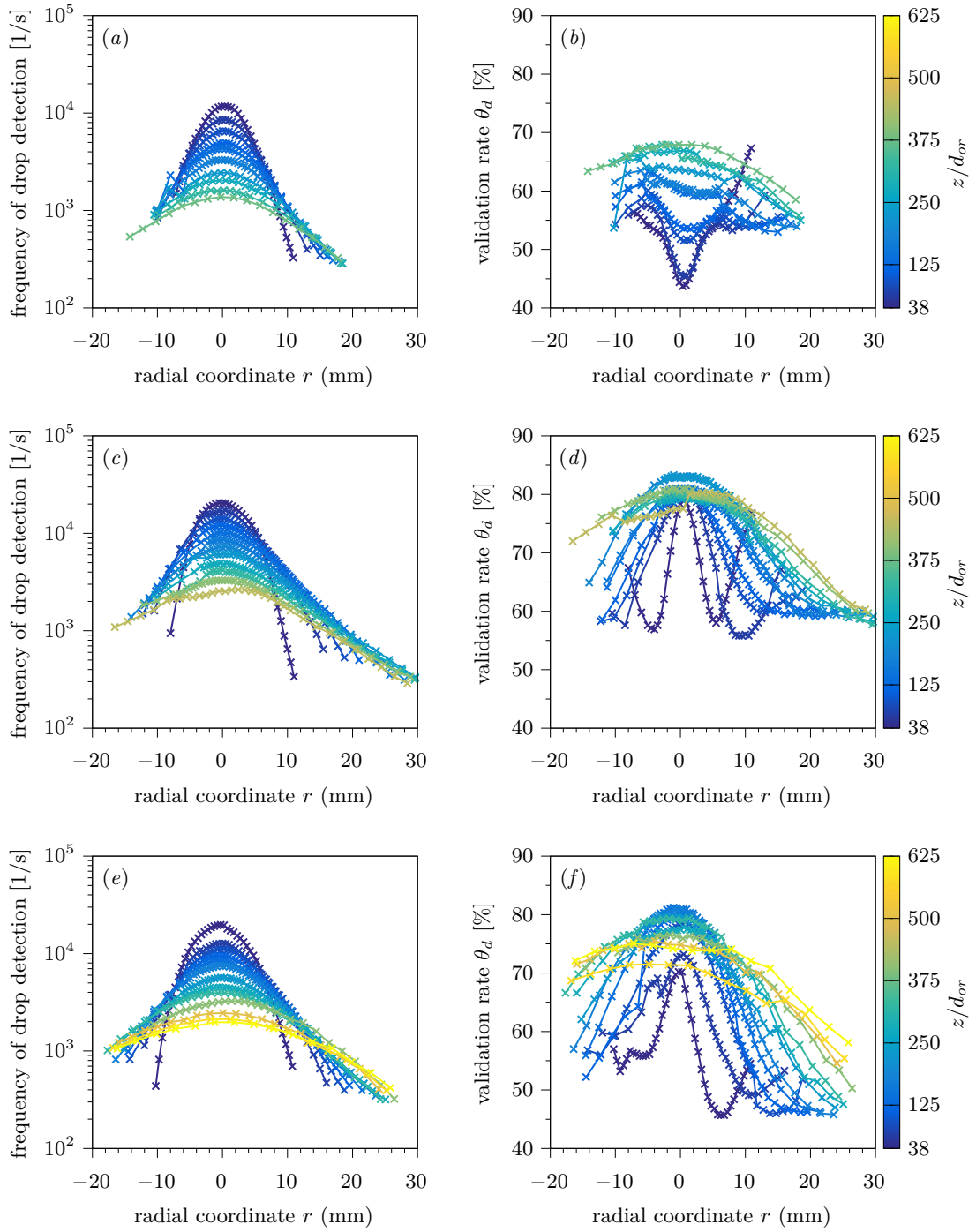


Figure 4.1: (a,c,e) Frequency of drop detection and (b,d,f) validation rate of the drop diameter θ_d , reported by the PDA system. From top to bottom, the results of sprays 1, 2 and 3 are shown.

4.1 FLOW FIELD OF THE LIQUID PHASE

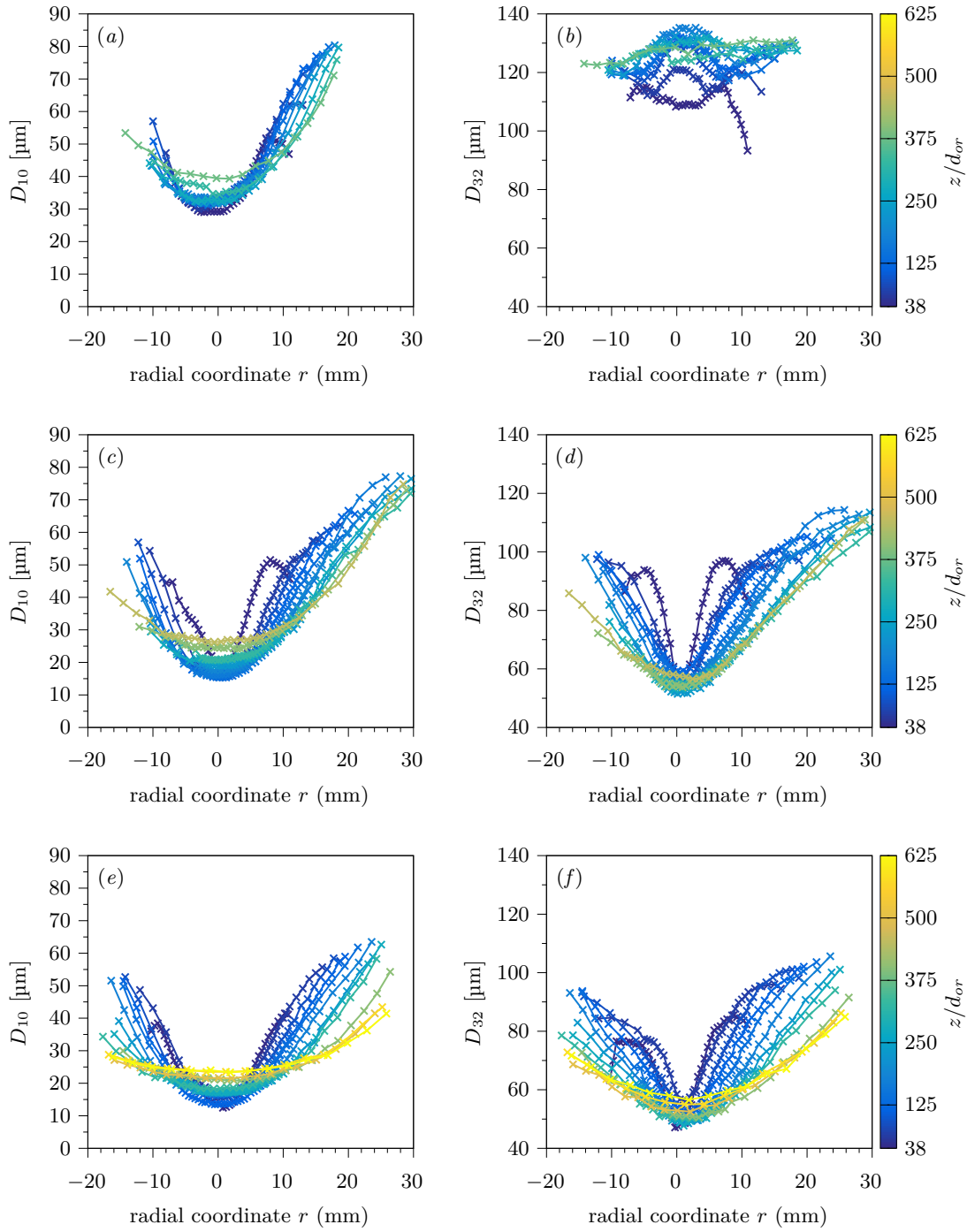


Figure 4.2: Experimentally obtained local mean drop diameters. (a,c,e) Number-mean drop diameter D_{10} and (b,d,f) Sauter mean drop diameter D_{32} . From top to bottom, the results of sprays 1, 2 and 3 are shown.

4 MEASUREMENT RESULTS

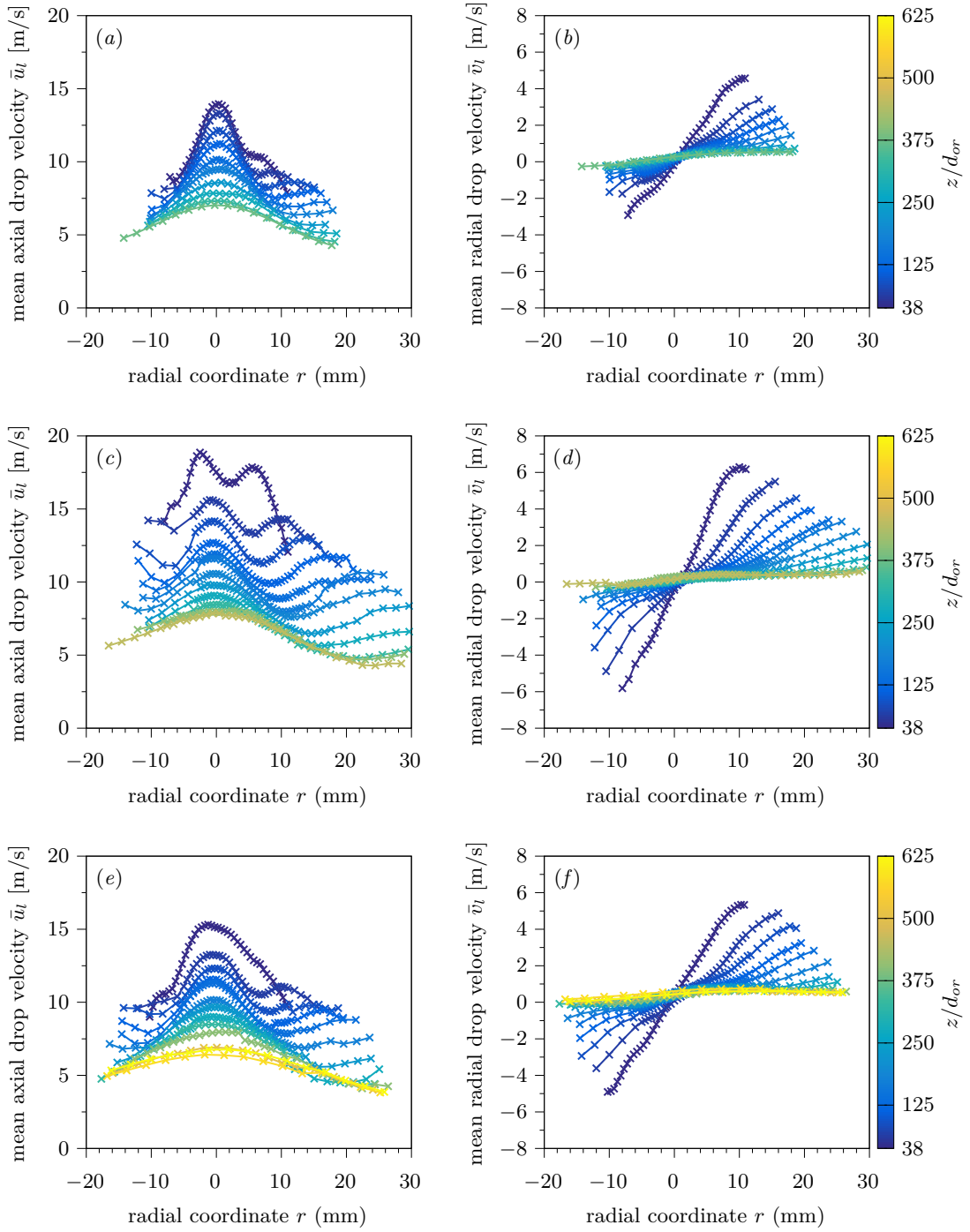


Figure 4.3: Experimentally obtained local mean drop velocities. (a,c,e) Number-mean axial drop velocity \bar{u}_t and (b,d,f) number-mean radial drop velocity \bar{v}_t . From top to bottom, the results of sprays 1, 2 and 3 are shown.

4.1 FLOW FIELD OF THE LIQUID PHASE

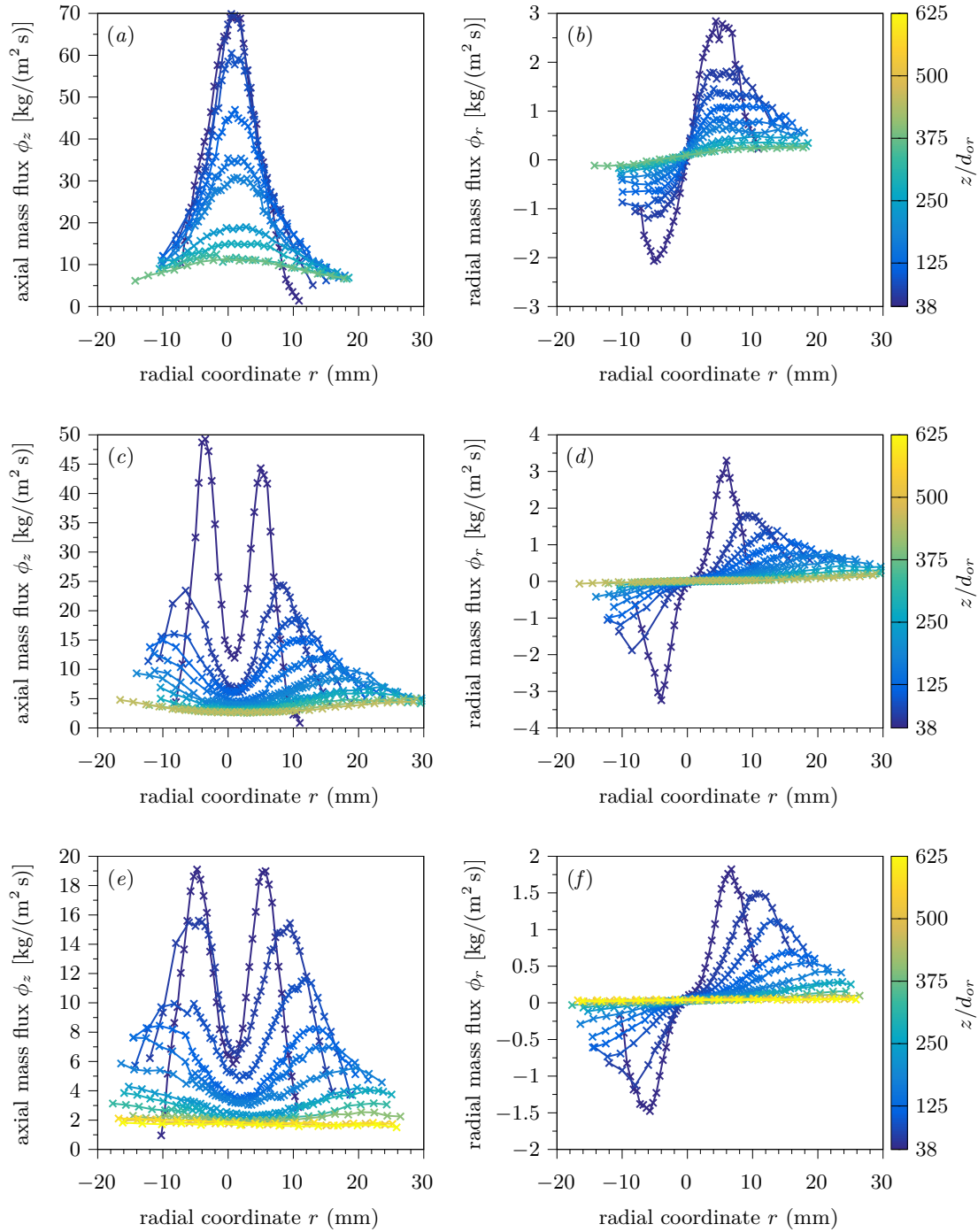


Figure 4.4: Experimentally obtained liquid mass fluxes. (a,c,e) Axial liquid mass flux ϕ_z and (b,d,f) radial liquid mass flux ϕ_r . From top to bottom, the results of sprays 1, 2 and 3 are shown.

4 MEASUREMENT RESULTS

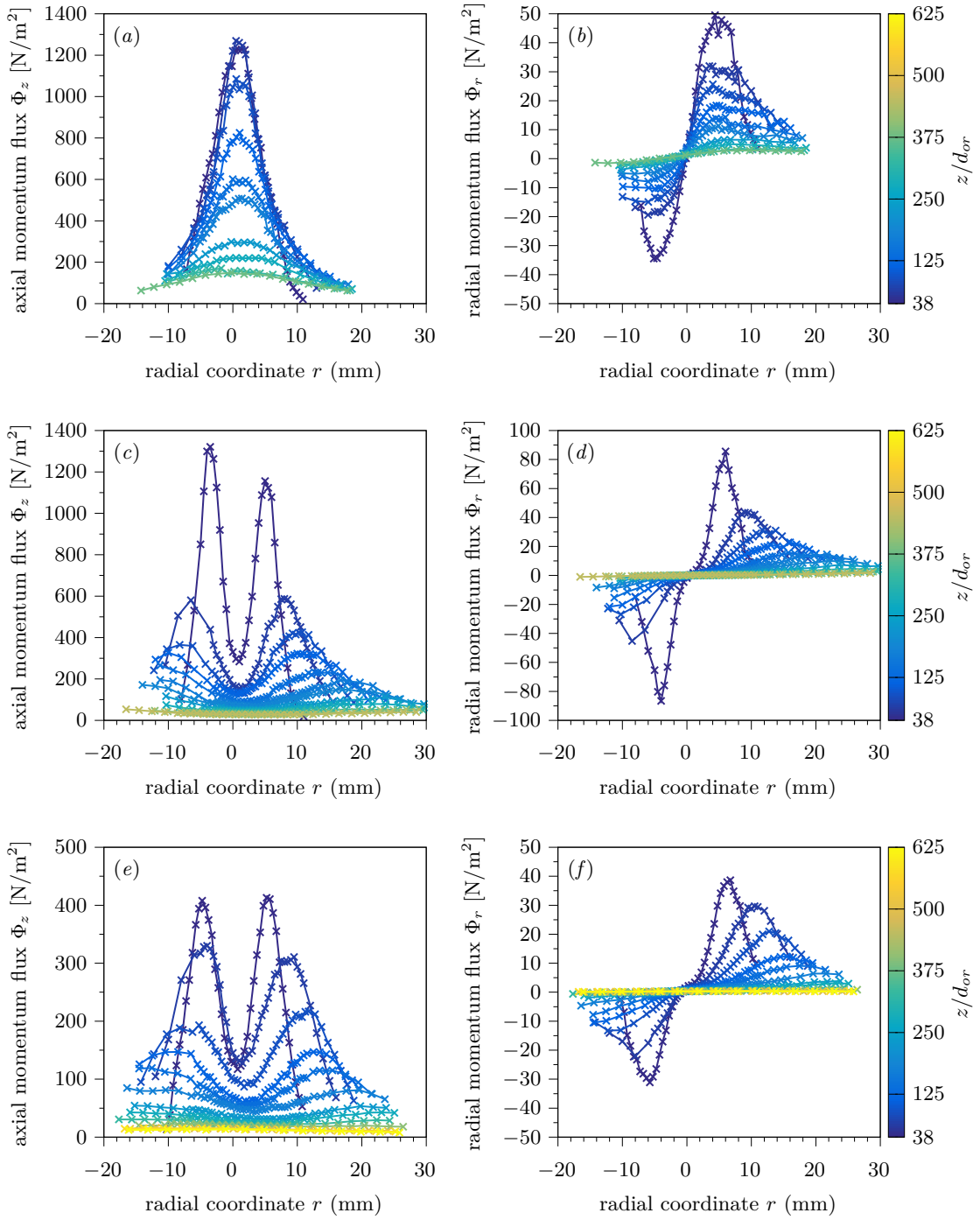


Figure 4.5: Experimentally obtained liquid momentum fluxes. (a,c,e) Axial liquid momentum flux Φ_z and (b,d,f) radial liquid momentum flux Φ_r . From top to bottom, the results of sprays 1, 2 and 3 are shown.

4.1 FLOW FIELD OF THE LIQUID PHASE

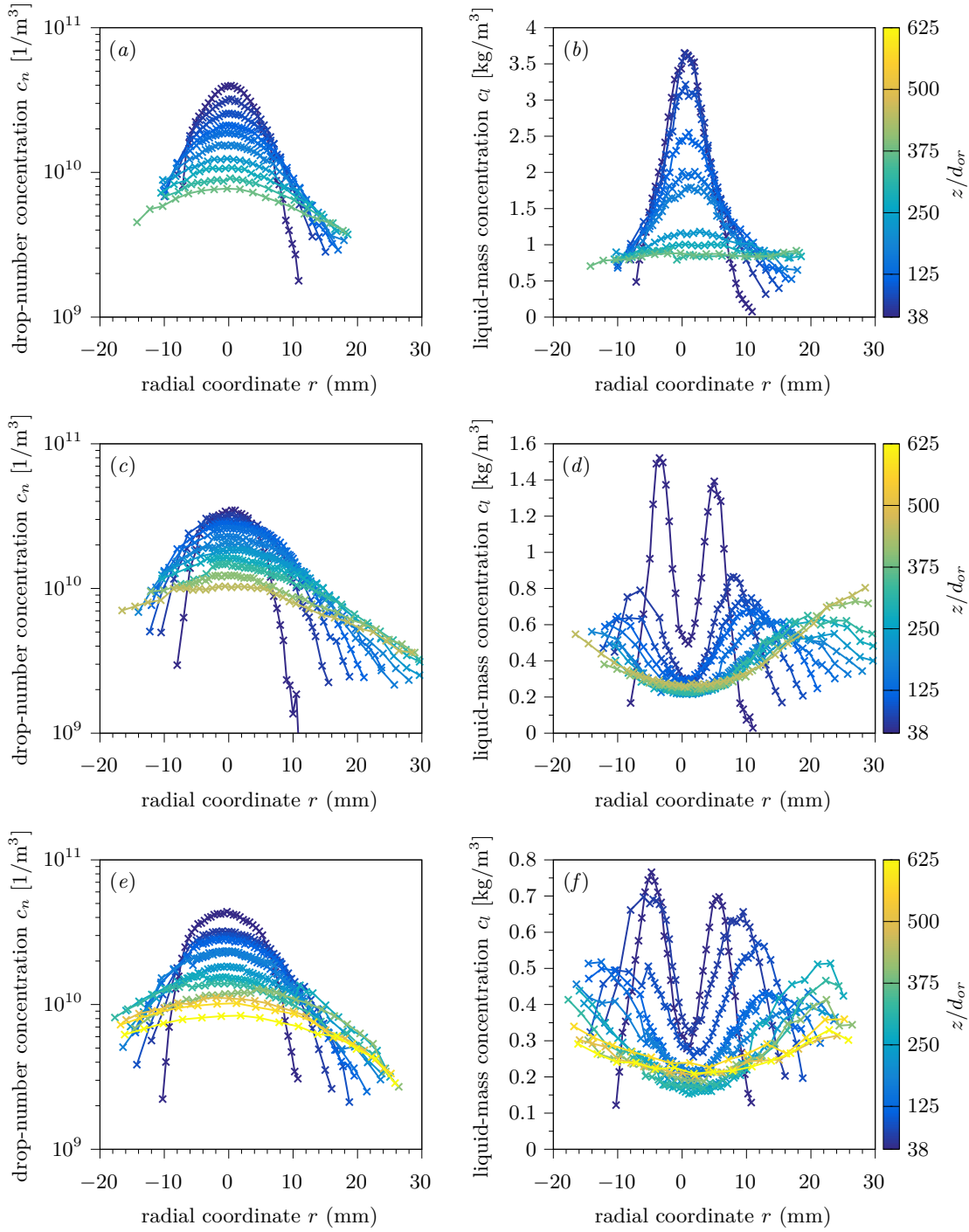


Figure 4.6: Experimentally obtained concentration profiles. (a,c,e) Local drop-number concentration c_n and (b,d,f) local concentration of liquid mass c_l . From top to bottom, the results of sprays 1, 2 and 3 are shown.

radially outwards. This shape of the profiles can be explained by the interaction of the liquid drops with the gas phase. The smallest drops preferentially stay in the core region near the spray axis, while larger drops, with more inertia, rather stay on their trajectories away from the spray axis. With increasing axial distance from the orifice, the mean drop diameter increases along the symmetry axis. This is due to the more pronounced decrease of the number flux of small droplets, compared to larger droplets. Drop coalescence is of minor importance in sprays like the present ones and does not significantly contribute to the increase of the number-mean drop diameter along the spray axis. This point will be discussed in more detail in section 4.1.2. Therefore, the evolution of the mean drop diameter in space is mainly governed by the convective transport of droplets in the two-phase flow field.

The profiles of the Sauter mean drop diameter D_{32} are depicted in figures 4.2(b,d,f). In sprays 2 and 3, they exhibit similar trends as the profiles of the number-mean drop diameter D_{10} . For spray 1, however, the shape of the profiles is quite ragged and does not show an obvious trend. D_{32} is approximately of constant value in each cross section. This behavior can be explained by different stages of spray atomization (see figure 2.2) associated with different liquid mass flow rates (see table 3.3). Due to the low liquid mass flow rate in spray 1, the liquid sheet emerging from the orifice is not fully open (see figure 3.10(a)), resulting in coarser atomization as compared to the two other sprays.

In the profiles of the number-mean axial drop velocity, shown in figures 4.3(a,c,e), significant differences between the sprays can be observed. Bell-shaped profiles, with a maximum at the spray axis, can be seen for spray 1. In contrast, the profile closest to the nozzle exit in spray 2 ($z/d_{or} = 38$), exhibits a local minimum at the spray axis and an additional off-axis maximum. This difference can be explained by the geometry of the atomizer. Due to the eccentric liquid supply, see figure 3.3(b), angular momentum is imposed on the liquid flow through the atomizer, leading to the formation of a hollow cone-shaped liquid sheet (see figure 3.10(b)). In spray 2, the off-axis peak in the velocity profile indicates the location of this sheet. At the lower liquid mass flow rate of spray 1, the angular momentum is not sufficient to fully open the conical sheet, leaving it rather in what is called the "tulip stage" (Lefebvre and McDonell 2017). The "tulip stage" is associated with coarser atomization, where the highest mean drop velocities occur at the spray axis. This explanation is endorsed by the profiles of the axial liquid mass and momentum fluxes, shown in figures 4.4(a,c) and 4.5(a,c), respectively. In spray 1, liquid mass and momentum accumulate at the spray axis, whereas the profiles of spray 2 exhibit an off-axis peak.

With increasing axial distance from the orifice, the shapes of the velocity profiles of all three sprays evolve into one with two peaks. One is located at the symmetry axis and the other next to the axis. The former is mainly determined by the motion of small droplets, yielding the maximum observed at the spray axis. The off-axis peak is

induced by the inertia-driven radial motion of large droplets, which stay on their initial trajectories radially outwards. In spray 3, the number-mean axial drop velocity profile closest to the orifice is bell-shaped, similar as in spray 1, but wider, extending over a larger cross-sectional area. The profiles of the axial liquid mass and momentum fluxes in spray 3 (see figures 4.4(e) and 4.5(e)), however, also exhibit an off-axis peak, suggesting the formation of a conical liquid sheet. This indicates that the velocity profile closest to the orifice in spray 3 represents an intermediate state, where both peaks, on- and off-axis, are merged into a single maximum. In spray 2, we expect an axial velocity profile of similar shape somewhere in the region between the two velocity profiles closest to the nozzle exit, i.e. $38 < z/d_{or} < 63$ (see figure 4.3(c)).

Figures 4.3(b,d,f) show the profiles of the number-mean radial drop velocity in the three sprays. Due to axisymmetry, the mean radial drop velocity is zero at the spray axis in all cross sections. The absolute value of the mean radial drop velocity increases radially outwards, and the profiles are antisymmetric with respect to the spray axis. The highest mean radial velocities are observed near the edge of the spray. Inertia-driven large drops with strong radial momentum are observed at a higher probability in this region, explaining this trend. With increasing axial distance from the atomizer, the mean radial drop velocity decreases.

The axial liquid mass flux in the sprays is depicted in figures 4.4(a,c,e). The profiles reflect the different regimes of atomization in the three sprays. In sprays 2 and 3, the profiles exhibit an off-axis peak in all cross sections, as a consequence of the fully open liquid sheet. The peaks indicate the propagation of droplets emerging from the breakup of the liquid sheet. The peak shifts radially outwards with increasing axial distance from the orifice, corresponding to the inertia-dominated motion of large droplets, which contain the major part of the liquid mass. As a result of the tulip-stage atomization process, the profiles in spray 1 (see figure 4.4(a)) are bell-shaped, with a maximum at the spray axis. The profiles of the radial liquid mass flux, as shown in figures 4.4(b,d,f), are antisymmetric with respect to the spray axis in all three sprays. The radial liquid mass flux grows with increasing radial distance from the symmetry axis, until a maximum is reached. Farther radially outwards it decreases to zero. The radial transport of liquid mass is responsible for the widening of the sprays with increasing axial distance from the atomizer.

The profiles of the axial and radial liquid momentum fluxes, shown in figure 4.5, resemble the profiles of the corresponding liquid mass fluxes in figure 4.4. The profiles of both, liquid mass and momentum fluxes, are of similar shape. In each spray, the mass and momentum fluxes in axial direction are at least one order of magnitude larger than the corresponding fluxes in the radial direction. Note that the reported magnitude of the mass and momentum fluxes has to be interpreted with caution. As discussed in section 3.2.1, flux terms calculated from PDA measurements are prone to errors, especially due

to uncertainties in the calculation of the drop-size and trajectory-dependent effective probe-volume cross section. An estimate of this error in the present measurements is given in section 4.1.2.

Figures 4.6(*a,c,e*) depict the local drop-number concentration. In all three sprays, the profiles are bell-shaped with a peak at the spray axis. Small drops, with diameters around $d \approx 15 \mu\text{m}$, exhibit high frequencies in the drop size spectrum and are preferably located in the core region of the sprays, near the symmetry axis. Large drops occur in lower numbers, and their contribution to the drop-number concentration is therefore of less importance. However, the opposite is true for the local concentration of liquid mass, see figures 4.6(*b,d,f*). The profiles of c_l in sprays 2 and 3 exhibit trends different from the profiles of the drop-number concentration c_n . This is due to the higher contribution of the large droplets to the total liquid mass ($c_l \propto d^3$). The profiles exhibit an off-axis peak, similar to the axial mass and momentum fluxes. In spray 1, most of the liquid mass is concentrated near the spray axis.

4.1.2 Global spray characteristics

Global spray characteristics are representative for a cross section of a spray. Their calculation is discussed in section 3.2.3. We introduce the results for the global drop size distributions and the corresponding mean drop diameters in the three sprays. Then, the liquid mass flow rates are calculated from the PDA measurement data and compared to the values set in the experiments.

Drop size spectra

Figure 4.7 depicts the global number-based probability density functions of the drop diameter in the sprays investigated. For all three sprays, the PDFs exhibit a peak at a droplet size of $d \approx 15 \mu\text{m}$. The PDF of spray 1 exhibits higher frequencies at larger drop diameters as compared to sprays 2 and 3. For spray 1, the PDF approaches zero at $d \gtrsim 200 \mu\text{m}$, for spray 2 at $d \approx 150 \mu\text{m}$ and for spray 3 at $d \lesssim 150 \mu\text{m}$. This is in agreement with the profiles of the local number-mean drop diameters shown in figures 4.2(*a,c,e*), which indicate coarse atomization in spray 1 and fine atomization in spray 3. The profiles of the probability density functions of the drop diameter do not significantly change with increasing distance from the orifice, suggesting that drop coalescence, secondary atomization and drop evaporation play a minor role in these sprays. A similar trend can be observed in the results for the global mean drop diameters. Figure 4.8 shows (*a*) the global number-mean drop diameter \overline{D}_{10} , and (*b*) the global Sauter mean drop diameter \overline{D}_{32} , as a function of the axial distance of the corresponding measurement plane from the orifice. Both, \overline{D}_{10} and \overline{D}_{32} , are largest in spray 1 and smallest in spray 3, with the mean drop diameters of spray 2 exhibiting values in between. The global

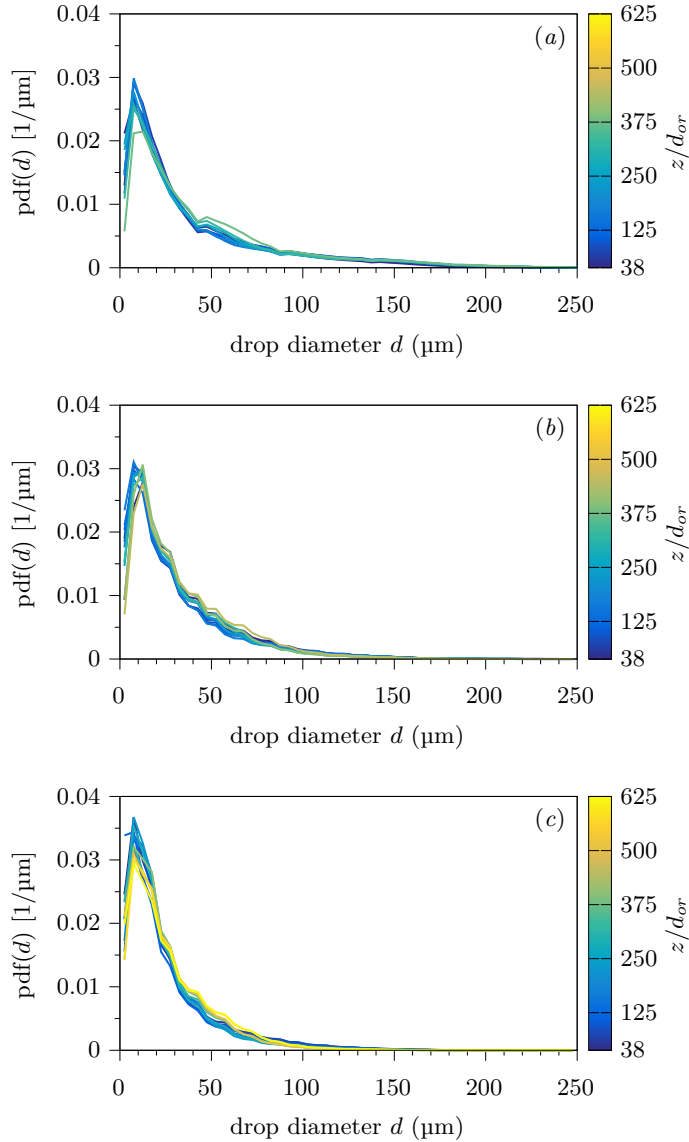


Figure 4.7: Global drop size spectra of (a) spray 1, (b) spray 2 and (c) spray 3.

number-mean drop diameter \overline{D}_{10} is approximately constant in each spray, independent of the location of the measurement cross section. Deviations close to the orifice can be attributed to the low validation rate of the PDA in this region, see figures 4.1(b,d,f). Far downstream, deviations occur due to the lower spatial resolution of measurement points and the increasing liquid mass near the spray edge not covered by measurement points. The constant values of \overline{D}_{10} indicate that drop coalescence plays a minor role, as expected in dilute sprays such as investigated in the present study. The global Sauter

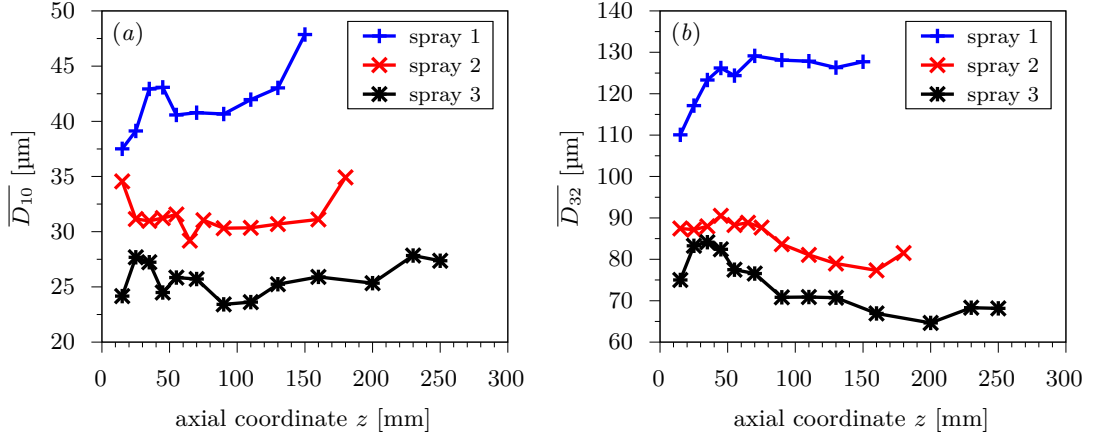


Figure 4.8: (a) Global number-mean and (b) global Sauter mean drop diameters.

mean drop diameters exhibit a similar axial evolution with approximately constant values. For sprays 2 and 3, \overline{D}_{32} decreases slightly with increasing axial distance from the orifice.

To conclude, in the sprays investigated, on the one hand, the atomization quality increases with the momentum flow rate through the orifice, i.e. with increasing Weber number (see table 3.3). On the other hand, Spray 3 exhibits the finest atomization because of the low surface tension of the liquid used, resulting in a larger Ohnesorge number than in the two other sprays. Changes in drop size due to drop coalescence and drop evaporation are of minor importance in the present sprays, see figures 4.7 and 4.8. Thus, the local profiles of the mean drop size (see figure 4.2) are mainly determined by the convective propagation of the drops in the two-phase liquid-gas flow downstream.

Liquid mass and momentum flow rates

The results obtained from the PDA measurements for the local axial liquid mass and momentum fluxes (see figures 4.4 and 4.5) can be integrated over the spray cross section to calculate the global mass and momentum flow rates, $\dot{m}_l(z)$ and $\mathcal{I}_l(z)$. For this purpose, we sum the local axial mass and momentum fluxes, (3.26) and (3.28), respectively, weighted with the representative local annular cross-sectional area (3.33), yielding

$$\dot{m}_l(z) = \sum_{i=1}^I \phi_z(r_i, z) A_m(r_i) \quad \text{and} \quad (4.1)$$

$$\mathcal{I}_l(z) = \sum_{i=1}^I \Phi_z(r_i, z) A_m(r_i). \quad (4.2)$$

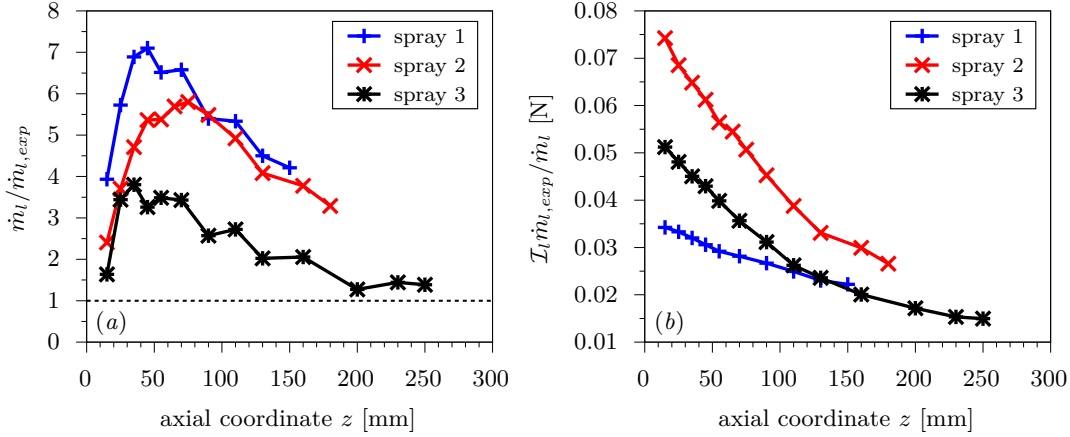


Figure 4.9: (a) Axial evolution of the liquid mass flow rate (4.1) calculated from PDA measurement data and scaled with the experimentally measured values of $\dot{m}_{l,exp}$ (see table 3.3). (b) Liquid momentum flow rate (4.2) obtained from PDA measurement data versus z . The values of \mathcal{I}_l are scaled to compensate for the overestimation of the liquid mass flow rate by the PDA.

Figure 4.9(a) shows the axial evolution of the liquid mass flow rate \dot{m}_l , as defined by (4.1), normalized with the experimentally measured liquid mass flow rate $\dot{m}_{l,exp}$. The value of $\dot{m}_l / \dot{m}_{l,exp}$ is expected to be equal to unity and to be independent of the z coordinate. The values of $\dot{m}_{l,exp}$ are obtained by collecting the liquid of the sprays during a certain period of time, 100 s in the present case. It can be observed that, depending on the spray and the axial distance from the orifice, the liquid mass flow rate is overestimated by the PDA up to 600%. This is due to inaccuracies in the computation of mass fluxes from PDA data. Especially the determination of the drop-size dependent effective probe-volume cross section is prone to uncertainties (Albrecht et al. 2003; Sipperley et al. 2018). The data of spray 1 exhibits the largest overestimation of the liquid mass flow rate, and the data of spray 3 the lowest. This is consistent with the expectation of a larger error in coarse sprays than in fine sprays since $\dot{m}_l \propto d^3$. Overestimates of flux terms calculated from PDA measurements in this order of magnitude are well reported in the literature (Tropea 2011; Bade and Schick 2011). With increasing axial distance from the orifice, the axial evolution of the liquid mass flow rate reaches first a plateau, and then it decreases slightly farther downstream in all three sprays. Close to the orifice, the overestimation is not as pronounced as farther downstream. This can be explained by the lower validation rates of the drop diameter in this region (see figure 4.1(b,d,f)), where large deformed drops are possibly not validated at a higher probability. An additional source of error is introduced by the fact that the measurement locations do not cover the entire spray cross section up to the edge of the spray (see section 3.1). Thus, far downstream, liquid mass is systematically overlooked. This error increases with the axial distance from the

orifice since the gap between the edge of the measurement positions and the spray edge increases. However, it partly compensates the overestimation of the mass flux by the PDA measurement data, and therefore contributes to the decrease of \dot{m}_l with increasing z , as shown in figure 4.9(a).

Next, we discuss the evolution of the liquid momentum flow rate \mathcal{I}_l , calculated from PDA measurement data by (4.2). The obtained values are prone to the same errors as the results of the liquid mass flow rate. Therefore, we scale \mathcal{I}_l at each axial position with the error reported for \dot{m}_l (see figure 4.9(a)) to include the correct axial trend of the liquid mass flow rate into liquid momentum flow rate. Figure 4.9(b) depicts the resulting axial evolution of the corrected liquid momentum flow rate. In all three sprays, the rate of liquid momentum flow through each cross section decreases with increasing axial distance from the atomizer. This is due to the transfer of momentum from the fast droplets to the slower gas phase.

4.2 Flow field of the gas phase

The motion of a liquid drop, or a particle, suspended in a continuous gaseous flow field is characterized by the nondimensional Stokes number. This number represents the ratio of the characteristic relaxation time scale of the particle t_p to the characteristic relaxation time of the continuous phase t_f , and is defined as

$$St = \frac{t_p}{t_f}. \quad (4.3)$$

For Stokes numbers much smaller than unity, i.e. $t_p \ll t_f$, the particles quickly adapt to velocity changes in the surrounding flow field and therefore may be used as tracer particles to represent the flow field of the continuous phase. For large Stokes numbers the opposite is true, particles are only weakly influenced by velocity changes in the ambient flow field.

The characteristic relaxation time scale of a particle is obtained from Stokes flow (Stokes 1851) and reads

$$t_p = \frac{\rho_p d_p^2}{18\mu}, \quad (4.4)$$

where ρ_p denotes the particle density, d_p the particle diameter and μ the dynamic viscosity of the continuous phase. The determination of a characteristic time scale for the continuous phase requires characteristic length and velocity scales. However, selection of appropriate values for these two quantities is not always straightforward, especially in two-phase spray flow. In theory, the smallest scales of turbulent motion are defined by

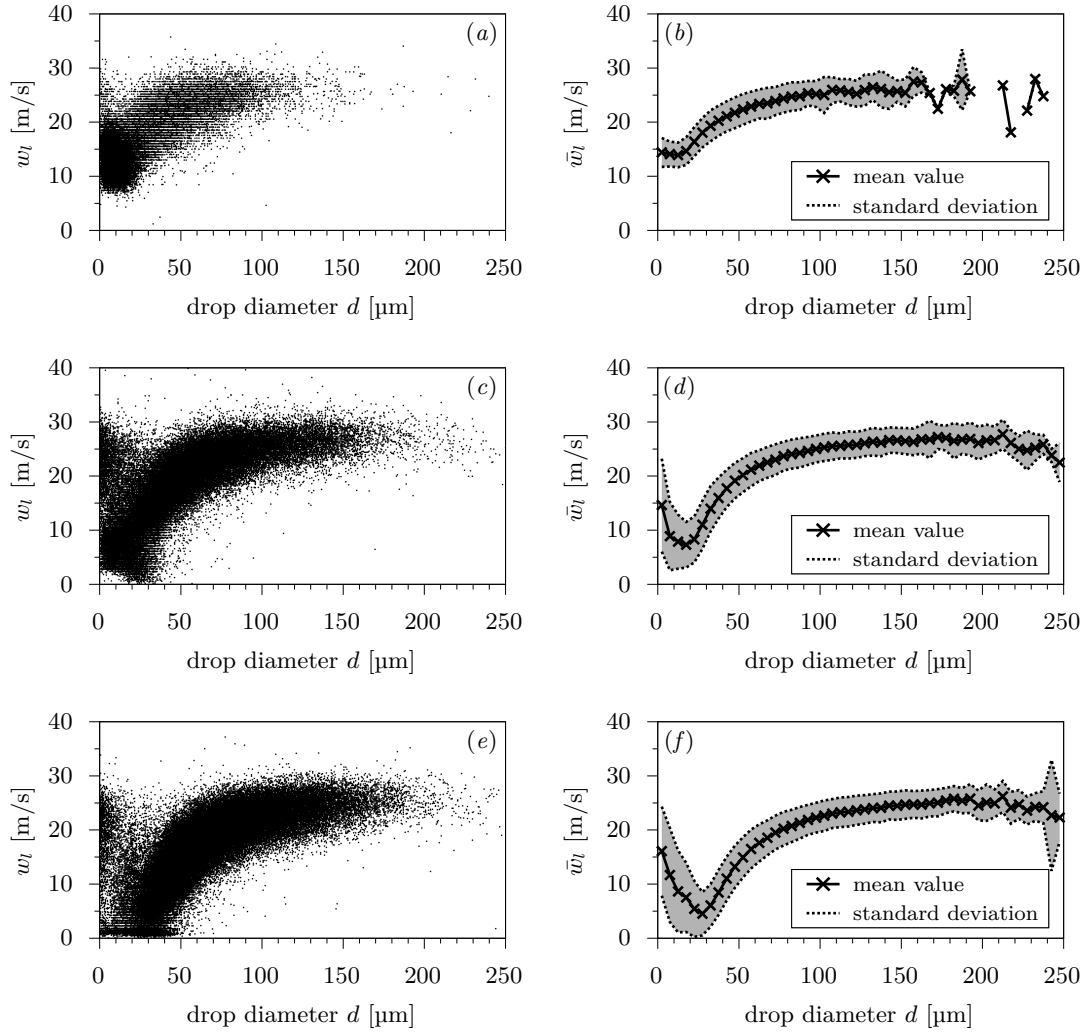


Figure 4.10: (a,c,e) Drop diameter-velocity correlations and (b,d,f) size-class number-mean drop velocity as a function of the drop size at the three different measurement positions $z = 25$ mm; $r = 0, 7, 14$ mm (top to bottom) for spray 2.

the Kolmogorov microscales (Pope 2000). In practice, however, to determine the velocity of the gas phase in spray flows from PDA measurements, usually the smallest drops in the local ensemble are assumed to have relaxation time scales, and therefore Stokes numbers, small enough to represent the mean velocity of the gas flow field. To ensure a proper representation of the gas flow field, a threshold droplet size must be defined, which depends on the turbulence of the gas flow field, the liquid density of the drop and the dynamic viscosity of the gas phase (see equations (4.3) and (4.4)). Detailed analysis of the experimental PDA data yields the threshold drop size.

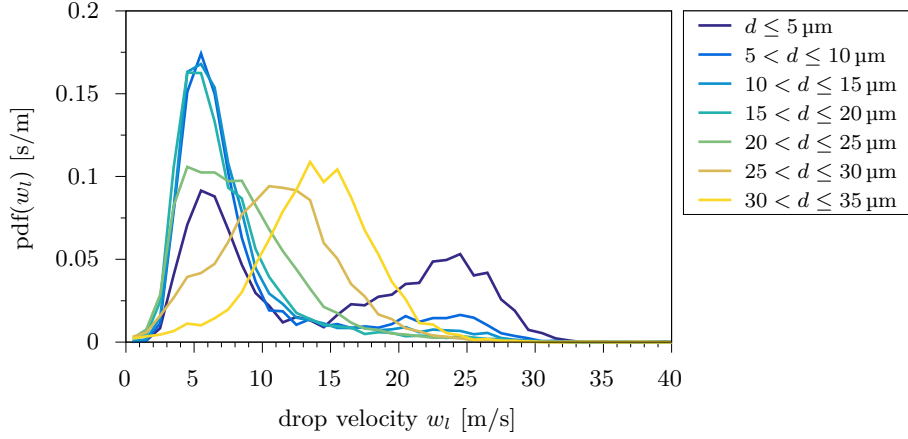


Figure 4.11: Bimodal velocity spectra observed for small droplets in spray 2 at $z = 25$ mm and $r = 7$ mm.

In figure 4.10, on the left-hand side, scatter plots of the diameter-velocity correlation of droplets measured at three different radial positions $r = 0, 7, 14$ mm (a, c, e) in the cross section $z = 25$ mm of spray 2 are shown. It can be observed that the drop velocity increases with the drop size. This is characteristic for sprays injected into a stagnant gaseous medium. The smallest droplets, with approximately $d < 20$ μm , however, deviate from this trend. A secondary cloud of data points at unexpectedly high velocities is found. The number-mean drop velocities \bar{w}_l in each size class d_d , corresponding to data in the scatter plots, are depicted in figures 4.10(b, d, f). According to the physical expectation, the mean velocity of the drops increases with the drop diameter. For small droplets, here smaller than approximately 25 μm in size, however, the opposite trend is observed. This is an unexpected finding, since we expect the smallest droplets to decelerate fastest to the velocity of the ambient gas phase. This effect, which we call the *teaspoon effect*, due to the shape of the profiles of the mean drop velocities at varying drop size, was observed in all three sprays investigated. It has been reported by others already, but not explained (Li et al. 1991; Li and Tankin 1992). We are sure that this effect is not an artifact of the PDA measurements and, therefore, requires further investigation.

Figure 4.11 provides a spectral view of the *teaspoon effect*. It shows the probability density function of the drop velocity, $\text{pdf}(w_l)$, for drops in the seven smallest drop size classes. The data corresponds to the results of figure 4.10(c, d). For drops with approximately $d < 10$ μm , the PDF exhibits two peaks. One at a relatively low velocity of $w_l \approx 6$ m/s and a second one at a larger velocity of $w_l \approx 25$ m/s. The two modes of the PDF indicate that two different physical mechanisms influence the velocity spectra of these droplets. We attribute the first peak, at the lower drop velocity, to the mean velocity of the ambient gas flow field. It represents the drops which follow the mean gas flow tightly due to drag. All drop size classes with $d < 20$ μm show this peak at

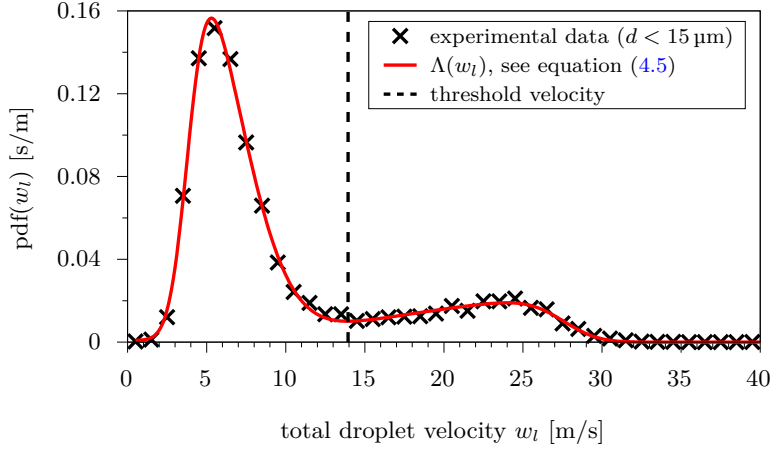


Figure 4.12: Bimodal velocity spectra of drops with $d < 15 \mu\text{m}$ obtained in spray 2 at $z = 25 \text{ mm}$ and $r = 7 \text{ mm}$.

approximately the same velocity. For the second peak in the bimodal distributions of the smallest drops, at the higher drop velocity, a satisfactory explanation has yet to be found. A detailed analysis of the PDA data revealed a higher probability of the detection of these small fast droplets directly after a large fast droplet was detected. This may be an indication for a grouping effect, keeping the velocities of small drops high due to the wake of larger drops. However, the statistical reliability of these results is low since they require pairs of validated drops in the data set where a large fast drop directly precedes a small drop. As shown in figure 4.11, for drop size classes with drop diameters $d > 20 \mu\text{m}$, only unimodal probability density functions are observed. With increasing drop size, the peaks shift to larger velocities, indicating that these drops move faster than the ambient gas flow.

For the correct determination of the mean gas velocity from the bimodal velocity distributions observed in the present sprays, we exclude the in this sense unphysically high drop velocities from the data analysis. Accordingly, we define a threshold velocity, below which the velocities of the small droplets represent the gas velocity at each measurement location. For this purpose, we determine the PDF of the drop velocity for all drops smaller than $15 \mu\text{m}$. Then, we fit this experimental data with a skewed probability density function of the form

$$\Lambda(x) = q\lambda_1(x) + (1 - q)\lambda_2(x) \quad \text{with} \quad (4.5)$$

$$\lambda_i(x) = \frac{2}{\omega_i \sqrt{2\pi}} \exp\left(-\frac{(x - \xi_i)^2}{2\omega_i^2}\right) \int_{-\infty}^{\hat{\alpha}_i \frac{x - \xi_i}{\omega_i}} \exp\left(\frac{-\tau^2}{2}\right) d\tau. \quad (4.6)$$

4 MEASUREMENT RESULTS

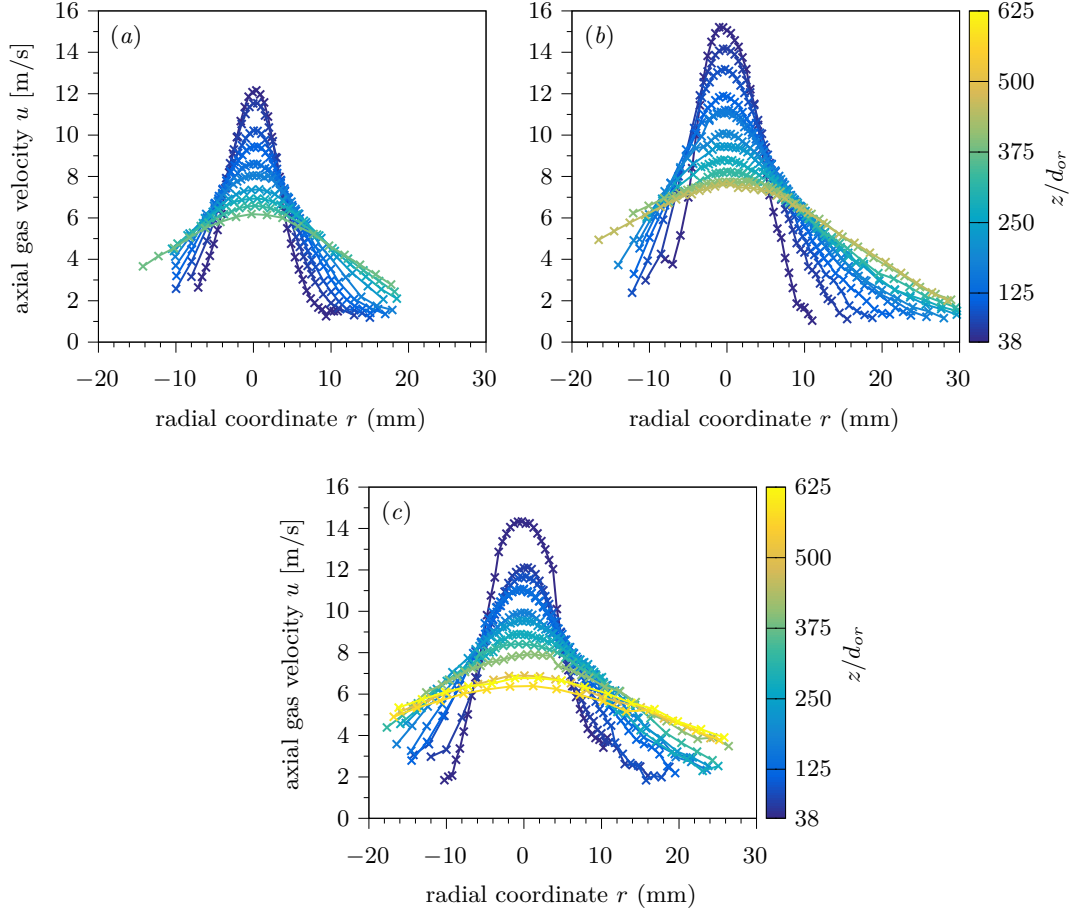


Figure 4.13: Axial velocity profiles of the gas flow field in the sprays, deduced from the mean velocities of small droplets. (a) Spray 1, (b) spray 2 and (c) spray 3.

Here, q is a weighting factor taking values between 0 and 1, ξ_i represents an arithmetic mean, ω_i^2 corresponds to a variance and $\hat{\alpha}_i$ defines the skewness of the distribution. As an example, figure 4.12 shows that the fit curve (4.5) (solid line) and the experimental data (symbols) are in excellent agreement. The data corresponds to the results shown in figure 4.10(c,d). We define the local minimum between the two peaks of the PDF, indicated by the dashed vertical line, as the threshold velocity. Only drops with $d < 15 \mu\text{m}$ and velocities smaller than the threshold velocity are taken into account for the calculation of the mean gas velocity. Using smaller drop size ranges, for example $d < 10 \mu\text{m}$, did not change the mean gas velocities obtained significantly.

With the method described above, we deduce the gas velocities from the PDA measurement data. The resulting axial gas velocity profiles are depicted in figure 4.13 for (a) spray 1, (b) spray 2 and (c) spray 3. In all three cases, bell-shaped profiles, with

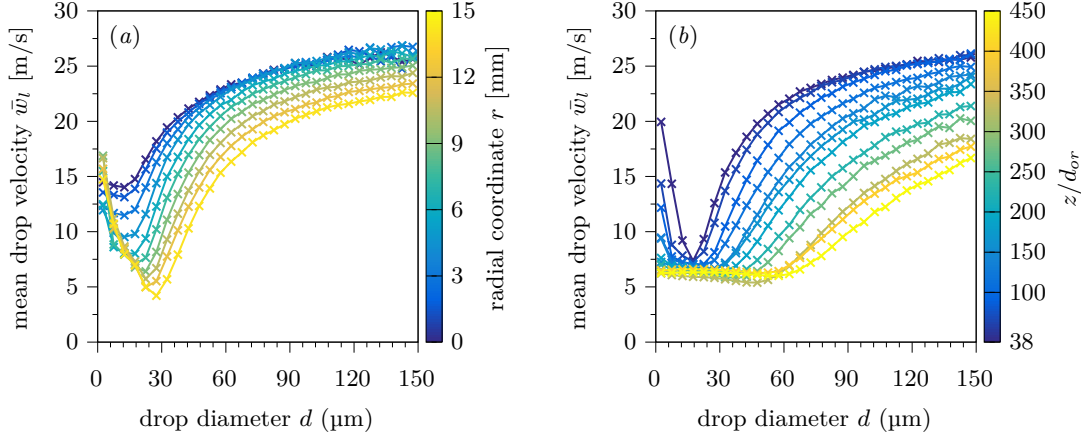


Figure 4.14: (a) Radial evolution of the *teaspoon effect* at $z = 35$ mm and (b) axial evolution of the *teaspoon effect* at $r = 7$ mm in spray 2.

their peaks at the spray axis, are obtained. The maximum value of the velocity on the symmetry axis decreases with increasing axial distance from the orifice. As the spray propagates in the ambient air downstream, its cross-sectional area increases. The radial expansion is evident from the downstream increase of the axial gas velocity at larger radial distances from the symmetry axis. The self-similar description of these velocity profiles is the main objective of the present work and discussed in chapter 5.

Note, the bimodal velocity distributions shown in figures 4.11 and 4.12 do not occur at all measurement positions in the sprays. Far downstream from the atomizer, the *teaspoon effect* vanishes and only unimodal distributions are observed. As an example, figure 4.14 shows (a) the radial evolution in a given cross section and (b) the axial evolution at a given radial position of this phenomenon in spray 2. In figure 4.14(a), in the cross section $z = 35$ mm, close to the atomizer, the *teaspoon effect* exists at all radial positions. In figure 4.14(b), it vanishes with increasing axial distance from the orifice. These findings support the wake-based explanation of this phenomenon. Since the spatial drop concentration decreases with increasing distance from the orifice, see figures 4.6(a,c,e), the potential interaction of drop motions in the spray reduces. An in-depth analysis of the *teaspoon effect* is beyond the scope of this work and, certainly, also beyond the capabilities of the utilized optical measurement method. To shed light on this effect, individual droplets and their change in velocity need to be resolved along their trajectories in the spray.

Beside the works of Li et al. (1991) and Li and Tankin (1992), who already reported the phenomenon of the *teaspoon effect*, a similar effect has also been observed for jets in crossflow. There, the liquid jet is subjected to the aerodynamic forces from the, typically very fast, gaseous crossflow. As a consequence, the liquid jet is bent perpendicular to

its symmetry axis by the interaction with the gas flow and subsequently disintegrates into liquid droplets. In comparison to the sprays in the presents study, the roles of the liquid and gas phases are reversed. At the nozzle exit, the undisturbed liquid jet exhibits no velocity component in the direction of the high-speed gaseous crossflow. The formed droplets are accelerated by the gas flow. Smaller droplets are expected to accelerate faster than larger droplets. Thus, a decrease of the mean drop velocity with increasing drop size is expected. However, in certain studies, the opposite trend has been reported in the smallest drop size classes. For example, Sinha et al. (2015) investigated drop size and velocity distributions of airblast sprays in crossflow. They utilized particle tracking velocimetry (PTV) and particle/droplet imaging analysis (PDIA) as measurement techniques. They reported unexpectedly small mean velocities of the smallest drop size classes at certain measurement locations (see figure 20 in Sinha et al. 2015), which may be interpreted as a "reversed *teaspoon effect*". As an explanation for this unexpected trend, they suspect a significant influence on the gas flow field by vortex shedding of the gas jet from the airblast injector. As in the present case, an in-depth analysis of this effect is yet to be done. Due to the similarity of the present pressure-atomized sprays and the airblast sprays in crossflow (one phase stagnant, the other phase at high velocity) these phenomena may be caused by the same physical mechanism.

Chapter 5

Self-similar modeling

A self-similar description of the gas- and liquid-phase flow fields of pressure-atomized sprays, accounting for momentum transfer between the two phases, is derived from boundary-layer theory. This development constitutes a generalization of the description by Schlichting (1933) for the single-phase submerged round jet, reviewed in section 2.2.

5.1 Equations of motion

For the present analysis, the sprays are treated as non-evaporating, i.e., heat and mass transfer between the liquid and the gas phases are not considered. The flow field of the gas phase in the sprays is of turbulent boundary-layer type with constant pressure throughout. For the description of the turbulent shear stress in the momentum balance, the Boussinesq eddy-viscosity concept is applied (Boussinesq 1877; Schmitt 2007). The turbulent eddy viscosity ν_t is assumed to be much greater than the molecular kinematic gas viscosity ν . Therefore, the molecular viscous contributions to the extra stresses are neglected. Moreover, the turbulent eddy viscosity ν_t is assumed to be of approximately constant value throughout the flow field, as known from the self-similar description of turbulent single-phase round jets (Tennekes and Lumley 1972; Peters 1997). Based on these assumptions, the steady-state axisymmetric boundary-layer equations in cylindrical coordinates for the gas phase read

$$\frac{\partial u}{\partial z} + \frac{1}{r} \frac{\partial(rv)}{\partial r} = 0 \quad \text{continuity gas} \quad (5.1)$$

$$u \frac{\partial u}{\partial z} + v \frac{\partial u}{\partial r} = \nu_t \frac{1}{r} \frac{\partial}{\partial r} \left(r \frac{\partial u}{\partial r} \right) + f_d \quad z\text{-momentum gas} \quad (5.2)$$

The mean gas velocities in axial and radial direction are denoted by u and v , respectively. Depending on the location in the spray and the drop size, large slip velocities occur between the drops and the gas phase. This is due to the injection of liquid into stagnant air. Therefore, we introduce the momentum source term f_d on the right-hand side of the

z -momentum equation (5.2). It represents the transfer of momentum by aerodynamic forces from the liquid to the gas phase. The radial momentum balance simplifies to the statement that the dependency of pressure on the radial coordinate in the boundary-layer flow is weak.

The equations of motion for the liquid phase describe the conservation of liquid mass and the loss of momentum due to the interaction with the gas phase. For this purpose we use the local liquid mass fluxes in axial and radial direction calculated from PDA measurement data, $\phi_{z,\underline{d}}$ and $\phi_{r,\underline{d}}$, as defined in section 3.2.2. The subscript \underline{d} denotes the \underline{d} th drop size class. We define the continuity equation and the z -momentum equation of the liquid phase as

$$\frac{\partial}{\partial z} \left(\sum_{\underline{d}=1}^{\underline{D}} \phi_{z,\underline{d}} \right) + \frac{1}{r} \frac{\partial}{\partial r} \left(r \sum_{\underline{d}=1}^{\underline{D}} \phi_{r,\underline{d}} \right) = 0 \quad \text{continuity liquid} \quad (5.3)$$

$$\frac{\partial}{\partial z} \left(\sum_{\underline{d}=1}^{\underline{D}} \bar{u}_{l,\underline{d}} \phi_{z,\underline{d}} \right) + \frac{1}{r} \frac{\partial}{\partial r} \left(r \sum_{\underline{d}=1}^{\underline{D}} \bar{u}_{l,\underline{d}} \phi_{r,\underline{d}} \right) = -\rho f_d \quad z\text{-momentum liquid} \quad (5.4)$$

The momentum equation in the radial direction is not considered due to the boundary-layer nature of the flow. In the z -momentum equation (5.4), $\bar{u}_{l,\underline{d}}$ represents the number-mean axial velocity of the drops in size class $d_{\underline{d}}$. The terms on the left-hand side of the z -momentum equation (5.4) represent the total change of axial momentum carried by the axial and radial liquid mass fluxes ϕ_z and ϕ_r , respectively. This change of momentum is balanced by the force term $-\rho f_d$ on the right-hand side. It dynamically couples the liquid-phase momentum balance (5.4) to the gas-phase momentum balance (5.2). It appears as a sink term in the liquid momentum balance due to its negative sign. The liquid momentum balance describes the net change in the axial liquid momentum flux. Liquid-liquid momentum transfer due to drop coalescence and breakup is not considered separately, and, as discussed in section 4.1.2, it is of little importance in the present sprays. Gravitation is neglected in the present analysis.

5.2 Self-similar transformation

To reveal, possibly, self-similar behavior of both the gas and the liquid phases in the pressure-atomized sprays investigated, we transform the z -momentum equation (5.2) of the gas phase into a self-similar form. For this purpose, the velocity components are represented as derivatives of the Stokesian stream function Ψ , so that the gas-phase continuity equation (5.1) is satisfied. The stream function is defined through the axial

and radial velocity components as

$$u = \frac{1}{r} \frac{\partial \Psi}{\partial r} \quad \text{and} \quad v = -\frac{1}{r} \frac{\partial \Psi}{\partial z}. \quad (5.5)$$

In terms of the stream function, the z -momentum equation of the gas phase (5.2) reads

$$\frac{1}{r} \frac{\partial \Psi}{\partial r} \frac{1}{r} \frac{\partial^2 \Psi}{\partial r \partial z} - \frac{1}{r} \frac{\partial \Psi}{\partial z} \frac{\partial}{\partial r} \left(\frac{1}{r} \frac{\partial \Psi}{\partial r} \right) = \nu_t \frac{1}{r} \frac{\partial}{\partial r} \left[r \frac{\partial}{\partial r} \left(\frac{1}{r} \frac{\partial \Psi}{\partial r} \right) \right] + f_d. \quad (5.6)$$

The self-similar coordinate η and the stream function Ψ are assumed to take the forms

$$\eta = rg(z) \quad \text{and} \quad \Psi = h(z)f(\eta), \quad (5.7)$$

where $g(z)$ is a scaling and $h(z)$ a mapping function. The function $f(\eta)$ represents the self-similar shape function. Introducing (5.7) into (5.6) yields

$$\left(\frac{h'}{\nu_t} + \frac{2}{\nu_t} \frac{g'}{g} h \right) f'^2 - \frac{h'}{\nu_t} \eta f \left(\frac{f'}{\eta} \right) = \eta \left[\eta \left(\frac{f'}{\eta} \right)' \right]' + \frac{1}{\nu_t g^4 h} \eta^2 f_d. \quad (5.8)$$

The prime denotes the derivative with respect to the coordinate η for $f(\eta)$ and with respect to the coordinate z for $g(z)$ and $h(z)$. The functions $g(z)$ and $h(z)$, as well as the source term f_d , must allow (5.8) to become an ordinary differential equation for $f(\eta)$. We therefore require

$$\frac{h'}{\nu_t} = \text{constant} := \tilde{A}, \quad (5.9)$$

$$\frac{h'}{\nu_t} + \frac{2}{\nu_t} \frac{g'}{g} h = \text{constant} := \tilde{C}, \quad (5.10)$$

yielding the functions $h(z)$ and $g(z)$ as

$$h(z) = \tilde{A} \nu_t z + \tilde{B}, \quad (5.11)$$

$$g(z) = \tilde{D} \left(\tilde{A} \nu_t z + \tilde{B} \right)^{(\tilde{C}-\tilde{A})/2\tilde{A}} = \tilde{D} h(z)^{(\tilde{C}-\tilde{A})/2\tilde{A}} \quad (5.12)$$

with the four constants \tilde{A} , \tilde{B} , \tilde{C} and \tilde{D} . To ensure independence of the axial coordinate z in (5.8), the source term f_d is assumed to take the form

$$f_d(r, z) = \nu_t \tilde{A} g(z)^4 h(z) \Omega(\eta), \quad (5.13)$$

where $\Omega(\eta)$ is a yet unknown self-similar shape function. For convenience, we introduce the constants

$$\alpha := -\frac{\tilde{C} - \tilde{A}}{2\tilde{A}}, \quad z_0 := -\frac{\tilde{B}}{\tilde{A}\nu_t}, \quad C := \tilde{A}\nu_t, \quad D := \tilde{D} \left(\tilde{A}\nu_t \right)^{(\tilde{C}-\tilde{A})/2\tilde{A}}. \quad (5.14)$$

Thus, the ansatz for self-similarity (5.7) and for the momentum source term (5.13) become

$$\eta = D \frac{r}{(z - z_0)^\alpha}, \quad \Psi = C(z - z_0)f(\eta), \quad f_d = C^2 D^4 (z - z_0)^{1-4\alpha} \Omega(\eta), \quad (5.15)$$

where z_0 marks the virtual origin of the self-similar flow field, α is an exponent, and C and D are constants required for dimensional reasons. The z -momentum equation (5.8) transformed into the self-similar coordinate η becomes

$$(1 - 2\alpha)f'^2 - \eta f \left(\frac{f'}{\eta} \right)' = \frac{\nu_t}{C} \eta \left[\eta \left(\frac{f'}{\eta} \right)' \right]' + \eta^2 \Omega(\eta). \quad (5.16)$$

For $\alpha = 1$ and $\Omega(\eta) = 0$, this equation reduces to the self-similar momentum equation of the single-phase round jet (see section 2.2). The axial and radial velocity components (5.5) turn into

$$u = g^2 h \frac{f'}{\eta} = CD^2 (z - z_0)^{1-2\alpha} \frac{f'}{\eta} \quad \text{and} \quad (5.17)$$

$$v = -gh' \frac{f}{\eta} - g'hf' = CD(z - z_0)^{-\alpha} \left(\alpha f' - \frac{f}{\eta} \right). \quad (5.18)$$

In general, the solution of (5.16) is subject to three boundary conditions for the gas flow field. The first two read

$$u|_{\eta \rightarrow 0} = \text{finite} \quad \Rightarrow \quad f'(0) = 0 \quad (5.19)$$

$$v|_{\eta \rightarrow 0} = 0 \quad \Rightarrow \quad f(0) = 0 \quad (5.20)$$

where we made use of the formulation of the velocity components with the self-similar function $f(\eta)$ in (5.17) and (5.18). The third boundary condition cannot be determined from general considerations on the velocity components of the flow field. As shown by Schlichting (1933), from the self-similar shape function of single-phase round jets follows that $f''(0)$ depends on global parameters of the flow field, such as the global momentum flow rate and the fluid properties. We expect a similar relation in the present case. To fully describe the self-similar gas flow field, and solve equation (5.16) for $f(\eta)$, the

quantities z_0 , α , ν_t , C , D and $\Omega(\eta)$ must be determined. The determination of these quantities, as well as the solution obtained for $f(\eta)$, are discussed in the subsequent sections 5.3 to 5.6.

5.3 Scaling variables

The virtual origin z_0 and the exponent α , and additional constraints relating to the self-similar solution, are determined from the self-similar representation (5.15). For this purpose, we link the self-similar transformed flow quantities to the experimental data. We specifically make use of three measured trends of the gas-flow field. These are the decrease of the axial gas velocity, $u_0(z) = u(0, z)$, on the symmetry axis of the spray, the increase of the axial momentum flow rate, $\mathcal{I}(z)$, and the scaled axial gas velocity, $u(r, z)/u_0(z)$.

For self-similarity these measured trends must meet the following constraints

$$u_0(z) = U_{exp}(z - z_0)^{1-2\alpha}, \quad (5.21)$$

$$\mathcal{I}(z) = M_{exp}(z - z_0)^{2-2\alpha}, \quad (5.22)$$

$$\frac{u(r, z)}{u_0(z)} = \text{constant} \quad \text{for} \quad r = R_{exp}(z - z_0)^\alpha. \quad (5.23)$$

Their derivation is discussed in the following sections 5.3.1 to 5.3.3. Here, unknowns are the model parameters z_0 and α , and the constants U_{exp} , M_{exp} and R_{exp} . These unknowns are determined by best fit using the experimental data for $u(r, z)$, $u_0(z)$ and $\mathcal{I}(z)$, acquired in the present study. Each constraint has its own independent fit parameter, i.e. U_{exp} , M_{exp} and R_{exp} , while z_0 and α appear in all of them. We have to choose z_0 and α such that all three constraints are simultaneously met. For this purpose, we fit the equations (5.21) to (5.23) separately to the experimental data for a range of specified values of α . Thus, for constraint (5.21) we obtain for each value of α corresponding values of z_0 and U_{exp} by best fit. The same applies to constraint (5.22), where we obtain corresponding values of z_0 and M_{exp} . The third constraint (5.23) at first glance appears a bit more complicated, since the values of z_0 and α may also depend on the velocity ratio u/u_0 . However, for the flow field to be self-similar, z_0 and α must be independent of u/u_0 , i.e. $z_0 \neq z_0(u/u_0)$ and $\alpha \neq \alpha(u/u_0)$. We show in section 5.3.3 that this is indeed the case. As a consequence of constraint (5.23) we obtain for each value of α corresponding values of z_0 and R_{exp} by best fit, where only the value of R_{exp} changes with the velocity ratio u/u_0 . With pairs of values (z_0, α) for each constraint at hand we then determine the best value for z_0 and the best value for α to satisfy the three constraints (5.21), (5.22) and (5.23). This is shown in section 5.3.4.

5.3.1 Axial gas velocity on the spray axis

The experimentally measured axial gas velocity on the symmetry axis of the spray $u_0(z) = u(0, z)$, where $r = 0$, i.e. $\eta = 0$, is represented by the formulation in equation (5.17). It reads

$$u_0(z) = \underbrace{CD^2 f''(0)}_{=:U_{exp}} (z - z_0)^{1-2\alpha}, \quad (5.24)$$

where the constant factor U_{exp} represents the product of the indicated quantities. The exponent α determines the axial decrease of u_0 . We expect a value of $\alpha > 0.5$, since the experimental data show a velocity decrease along the spray axis (see figure 4.13). We fit equation (5.24) to the experimental data (u_0, z) for α ranging between 0.5 and 1. For each α , the values of U_{exp} and z_0 are determined by best fit.

Figure 5.1(a) depicts the resulting fit curves in spray 2 for different values of the exponent α . Very good agreement can be observed for $\alpha \approx 0.7$. Conducting the same fitting process for sprays 1 and 3 as well, the results reveal that the experimental data agrees well with (5.24) for values of α in the range $0.6 < \alpha < 0.75$. Figure 5.1(b) shows the coefficient of determination R^2 of the best fits versus α for all three sprays. The dependency of the fitted values of the virtual origin z_0 on α is depicted in figure 5.1(c). Its values are close to zero for $\alpha \approx 0.62$ and decrease with increasing α . Figure 5.1(d) shows the best fit of U_{exp} as a function of α in the three sprays. Its values decrease with increasing α .

5.3.2 Gas momentum flow rate

The self-similar solution must meet the axial dependency of the momentum flow rate of the gas phase $\mathcal{I}(z)$, deduced from the experimental PDA data. In general, and in self-similar coordinates, the rate of axial momentum transport through a plane $z = \text{constant}$ is defined by

$$\mathcal{I}(z) = 2\pi\rho \int_{r=0}^{\infty} u^2 r \, dr = 2\pi\rho C^2 D^2 \underbrace{\int_{\eta=0}^{\infty} \frac{f'^2}{\eta} \, d\eta}_{=:M_{exp}} (z - z_0)^{2-2\alpha}. \quad (5.25)$$

Here, ρ is the density of the gas phase and the constant parameter M_{exp} represents the product of the indicated quantities. In contrast to the single-phase jet, the momentum flow rate of the gas phase is not constant, but it increases with the z coordinate due to momentum transfer from the liquid to the gas phase. The exponent α determines the axial scaling of the momentum flow rate. With increasing distance from the orifice, we

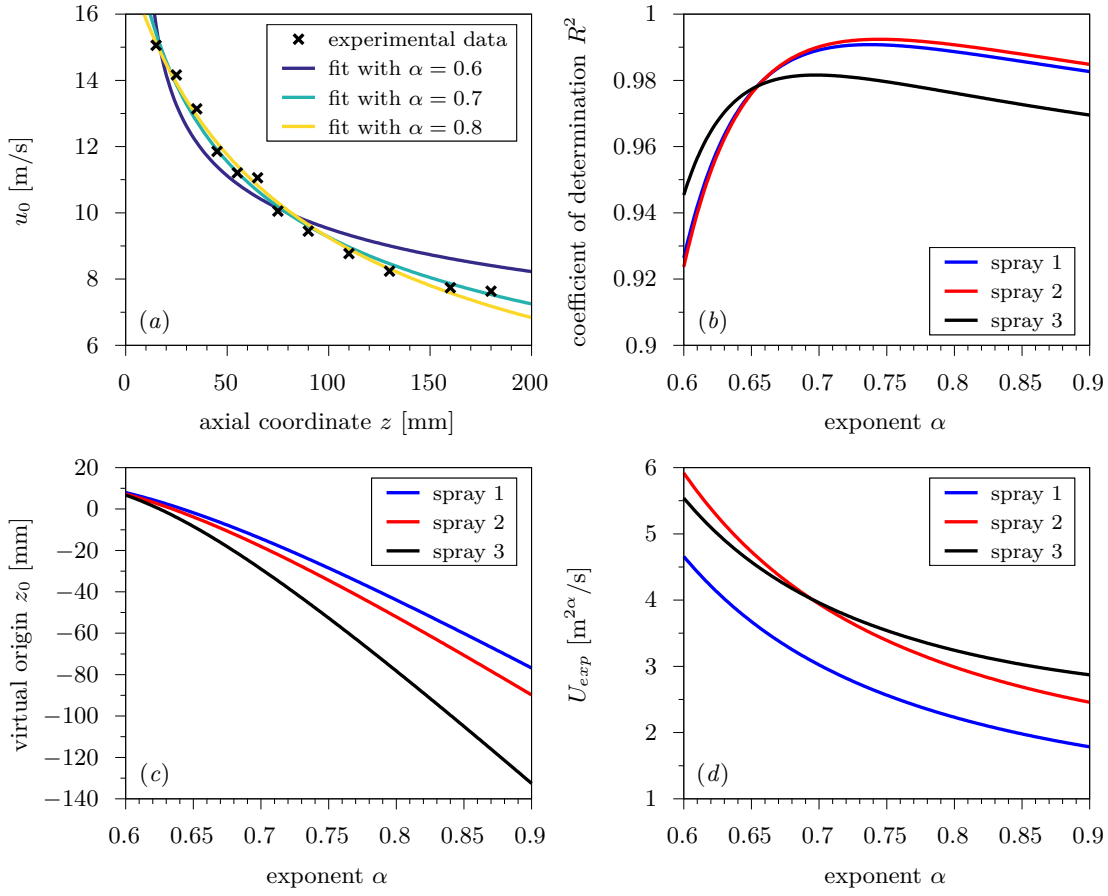


Figure 5.1: Best fit of the axial gas velocity at the spray axis (5.24) for different values of α in (a) spray 2. (b) The coefficient of determination R^2 , (c) the virtual origin z_0 and (d) the parameter U_{exp} versus α for the three sprays.

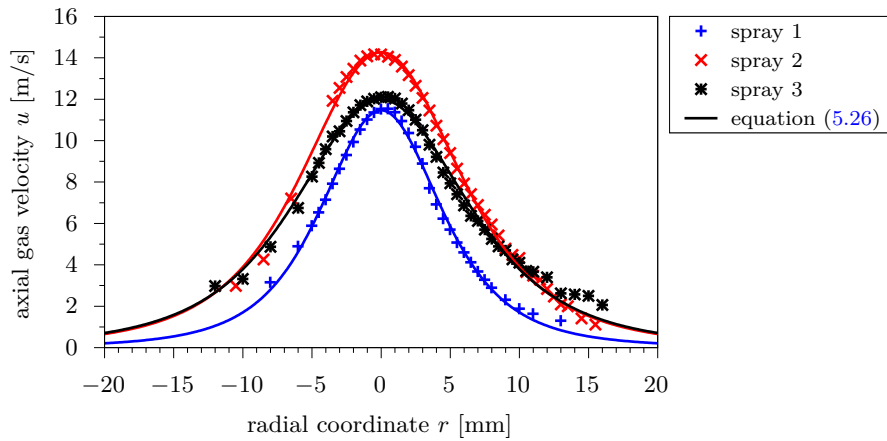


Figure 5.2: Experimental and fitted axial gas velocity profiles in the cross section at $z = 25$ mm.

expect the momentum flow rate to increase, but, on the other hand, its rate of change to decrease, i.e. $0 < \alpha < 1$. To calculate the experimental momentum flow rate of the gas phase \mathcal{I} from the PDA data, we require an analytical expression of the axial gas velocity u obtained experimentally at discrete positions r_i (see figure 4.13). For this purpose, the measured axial gas velocity profiles of each cross section are fitted with a bell-shaped function of the form

$$u(r, z) = \frac{A_1(z)}{(1 + A_2(z) r^2)^2}, \quad (5.26)$$

with the two independent functions $A_1(z)$ and $A_2(z)$. The function $A_1(z)$ represents the axial gas velocity at the spray axis. The obtained velocity profiles (5.26) are in excellent agreement with the experimental data, as exemplarily depicted in figure 5.2 at $z = 25$ mm. With the velocity profiles (5.26), the evolution of the experimental values of \mathcal{I} is calculated from (5.25) to

$$\mathcal{I}(z) = \frac{\pi}{3} \rho \frac{A_1(z)^2}{A_2(z)}. \quad (5.27)$$

With knowledge of the gas momentum flow rate \mathcal{I} , we determine the parameters M_{exp} and z_0 in equation (5.25) by curve fitting. As an example, figure 5.3(a) shows the resulting fit curves in spray 2 for different values of α . For each α , z_0 and M_{exp} are determined by best fit. In figure 5.3(b), the coefficient of determination of the fits is depicted as a function of α for all three sprays. Similar to the velocity decrease along the spray axis, as discussed in the previous section 5.3.1, excellent agreement of the experimental data for \mathcal{I} with (5.25) can be observed for values of α around 0.7. The dependencies of the virtual origin z_0 and parameter M_{exp} on α are shown in figures 5.3(c) and 5.3(d), respectively. The values of virtual origin z_0 increase with α , whereas the opposite is true for the parameter M_{exp} . For a given value of α , the fit results in sprays 1 and 3 exhibit the smallest and the largest values of M_{exp} , respectively.

5.3.3 Normalized axial gas velocity

The concept of self-similarity requires the normalized axial gas velocities u/u_0 to satisfy

$$\frac{u(r, z)}{u_0(z)} = \text{constant} \quad \text{for} \quad \eta = D \frac{r}{(z - z_0)^\alpha} = \text{constant}. \quad (5.28)$$

From our experimental data we compute the (r, z) coordinates in each cross section for a given velocity ratio u/u_0 . For this purpose, we use the fitted velocity profiles (5.26) in order to also consider small velocity ratios near the spray edge, not covered by the

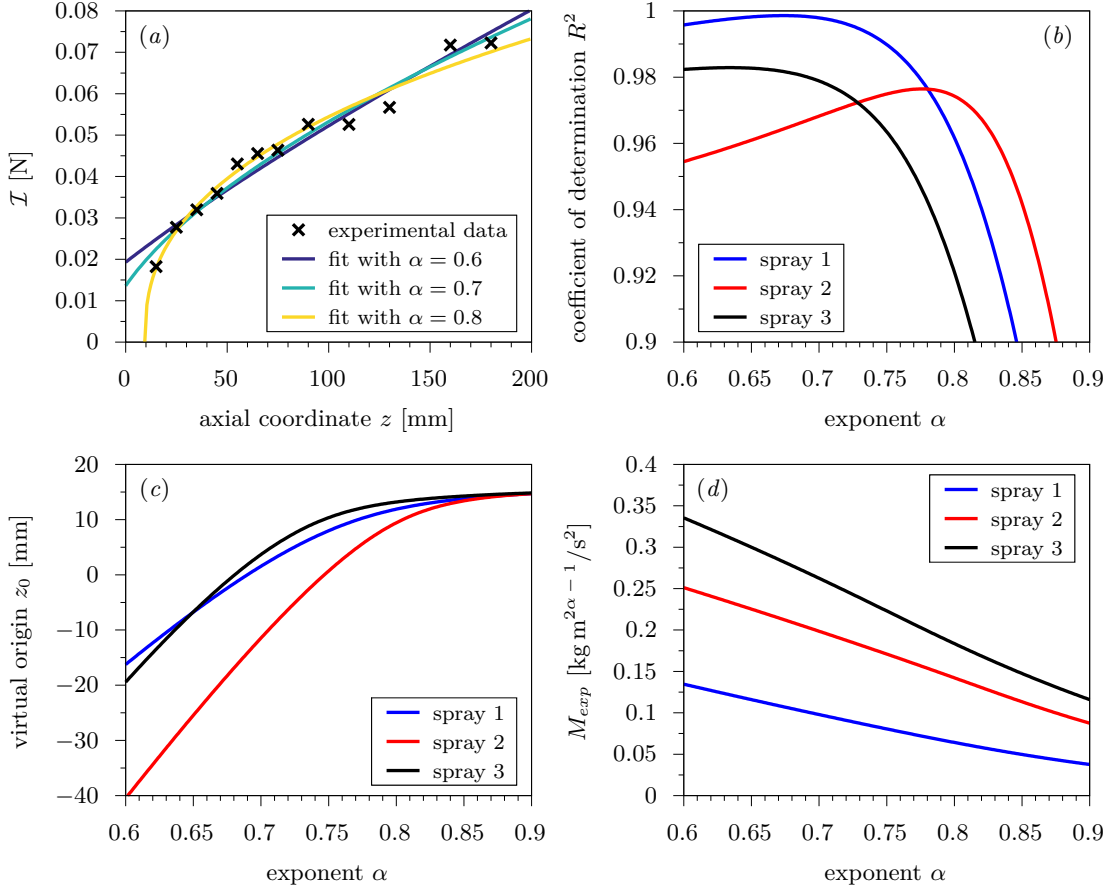


Figure 5.3: Best fit of the gas momentum flow rate according to equation (5.25) for different values of α in (a) spray 2. The experimental momentum flow rate is obtained from (5.27). (b) The coefficient of determination R^2 , (c) the virtual origin z_0 and (d) the parameter M_{exp} versus α in the three sprays.

measurements. Rewriting (5.28) for r yields

$$\frac{u(r, z)}{u_0(z)} = \text{constant} \quad \text{for} \quad r = \underbrace{\frac{\eta}{D}}_{=: R_{exp}} (z - z_0)^\alpha, \quad (5.29)$$

where R_{exp} represents the ratio η/D . For a given velocity ratio u/u_0 , with known (r, z) coordinates, we fit the virtual origin z_0 and parameter R_{exp} to (5.29) for a range of given values of α . For spray 2, the obtained results are shown in figure 5.4(a). It depicts the (r, z) coordinates of four corresponding velocity ratios u/u_0 between 0.3 and 0.9. The solid lines are obtained by curve fitting of (5.29) with $\alpha = 0.7$. The virtual origin z_0 and the parameter R_{exp} are parameters determined by the fit. Excellent agreement between fit curves and experimental data can be observed.

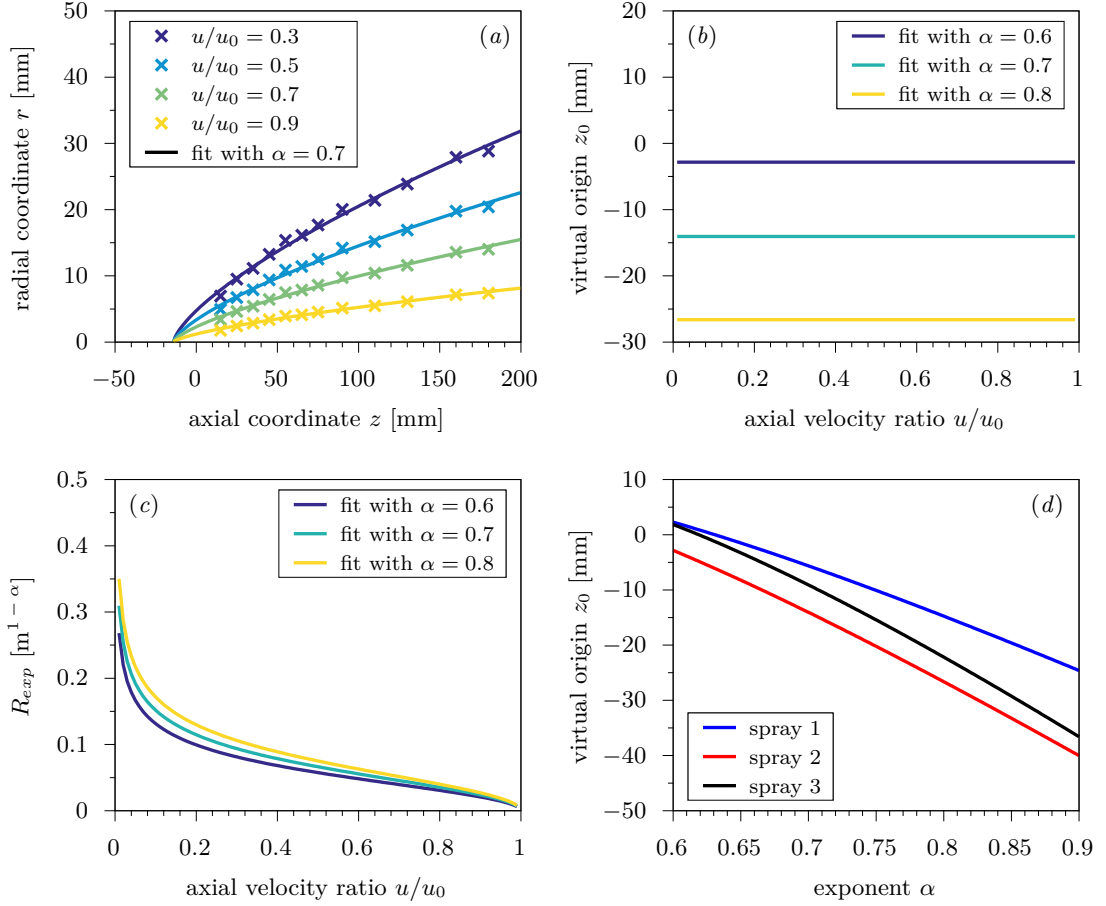


Figure 5.4: (a) Best fit of the coordinates corresponding to constant velocity ratios u/u_0 according to equation (5.29) for $\alpha = 0.7$ in spray 2. Evolution of (b) z_0 and (c) the parameter R_{exp} with u/u_0 for different values of α in spray 2. (d) Dependency of z_0 on α in all three sprays.

For the flow field to be self-similar, the value of the virtual origin z_0 and the value of the exponent α must be identical for all velocity ratios u/u_0 in a given spray. This is indeed the case, as shown in figure 5.4(b) for spray 2. For a given value of α , we obtain uniform values for z_0 as a result of the fitting process, independent of the velocity ratio u/u_0 . This fact can also be observed in 5.4(a), where lines $\eta = \text{constant}$ corresponding to different velocity ratios u/u_0 intersect in a single point, the virtual origin. Thus, only the ratio R_{exp} changes with u/u_0 , which is shown in figure 5.4(c) for three different values of α in spray 2. The fact that the virtual origin z_0 changes with α only was also observed in the two other sprays investigated. Figure 5.4(d) depicts the evolution of z_0 with α obtained by curve fitting of the experimental data to (5.29). In all three sprays, z_0 decreases with increasing α .

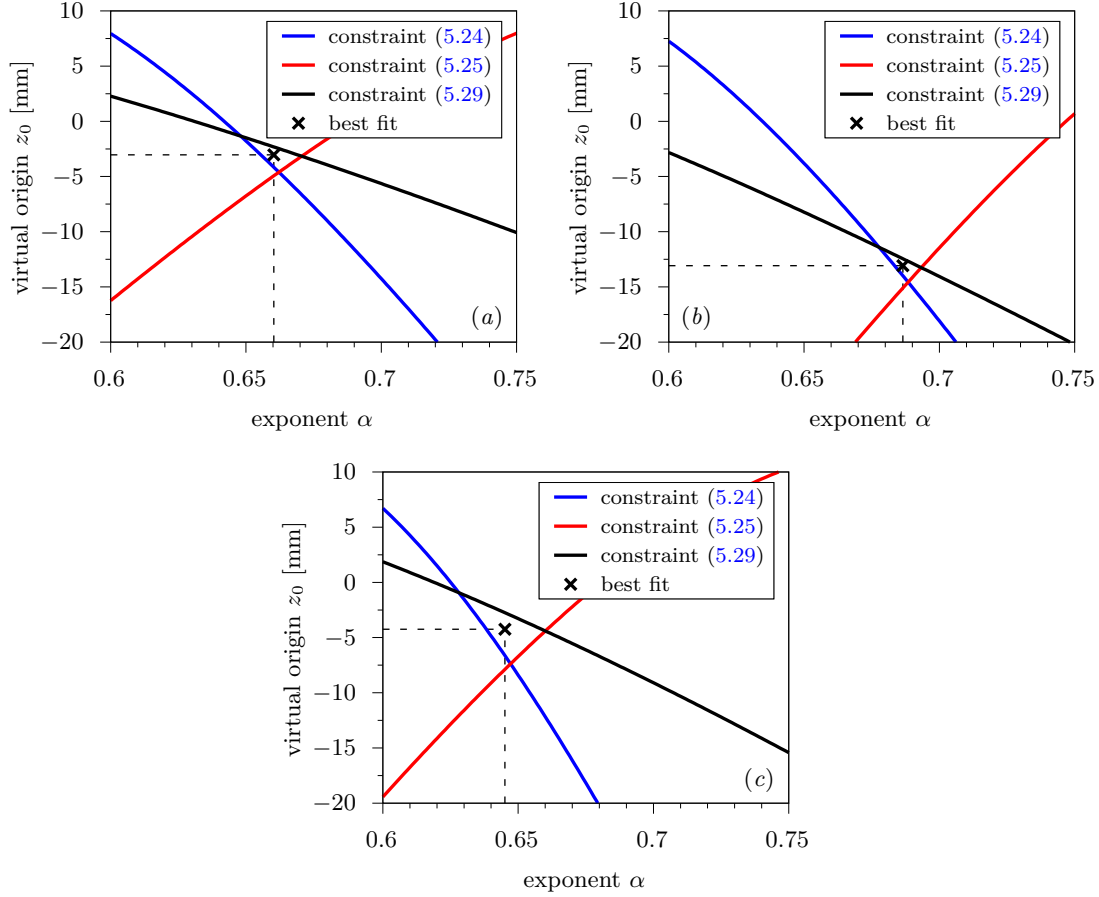


Figure 5.5: Determination of the exponent α and the virtual origin z_0 for (a) spray 1, (b) spray 2 and (c) spray 3.

5.3.4 Results

In the previous sections 5.3.1 to 5.3.3, we linked the experimental data to the mathematical self-similar description of the gas flow field. By means of curve fitting, the parameters z_0 , U_{exp} and M_{exp} were obtained from the three different constraints (5.24), (5.25) and (5.29) for a range of values of α . The virtual origin z_0 and the exponent α appear in all of these three constraints. Therefore, in each spray, the values of z_0 and α satisfying all three constraints need to be determined.

For this purpose, we compare the evolution of z_0 with α for the axial velocity decrease along the spray axis (see figure 5.1(c), constraint (5.24)), for the increase of the gas momentum flow rate (see figure 5.3(c), constraint (5.25)) and for the scaled axial velocity profiles (see figure 5.4(d), constraint (5.29)). This can be seen in figure 5.5 for each individual spray. If the gas flow fields of the sprays are truly self similar, we expect the

	Spray 1	Spray 2	Spray 3
α	0.66	0.69	0.65
z_0 [mm]	-3.0	-13.1	-4.2
U_{exp} [m ² α /s]	3.49	4.10	4.58
M_{exp} [kg m ² α ⁻¹ /s ²]	0.114	0.208	0.309

Table 5.1: Best values of the listed parameters.

three curves, corresponding to the constraints (5.24), (5.25) and (5.29), to intersect in a single point (z_0, α) . This is indeed almost the case in each spray, as the three binary intersection points of the three curves lie very close together. We determine the best values of α and z_0 by calculating the mean of their values in the three binary intersection points. The result corresponds to the centers of mass of the triangles enclosed by the three lines, which are marked by the black crosses in figure 5.5.

Table 5.1 lists the values of z_0 and α , and of the corresponding quantities U_{exp} and M_{exp} . The values of U_{exp} and M_{exp} were determined by curve fitting to (5.24) and (5.25) using the values z_0 and α obtained from figure 5.5. In contrast to the single-phase round jet, where its value is unity, the exponent α is close to a value of $2/3$ for all the three sprays investigated. As a result, the lines $\eta = \text{constant}$ are no longer straight lines, as in the single-phase case, but curved in the (r, z) space due to the acceleration of the gas phase by the liquid drops. This corresponds to the physical process of momentum transfer from the liquid to the gas phase. The virtual origins are located inside the nozzle, as indicated by the negative values obtained.

The values of U_{exp} and M_{exp} increase with the Weber and the Ohnesorge number (see table 3.3). A higher Weber number reflects a larger injected momentum flow rate, resulting in a larger velocity at the spray axis, i.e. a larger value of U_{exp} . In addition, the rate of momentum transfer from the liquid to the gas phase is increased, as indicated by a larger value of M_{exp} . At a high Ohnesorge number (spray 3), the liquid is finer atomized, resulting in smaller droplets (see figures 4.7 and 4.8(a)). Due to the increase in total liquid surface area, the momentum transfer to the gas phase is more intense, resulting in larger values of U_{exp} and M_{exp} . As indicated in equations (5.24) and (5.25), the two parameters U_{exp} and M_{exp} relate to the self-similar function $f(\eta)$ as per

$$U_{exp} = CD^2 f''(0) \quad \text{and} \quad M_{exp} = 2\pi\rho C^2 D^2 \int_{\eta=0}^{\infty} \frac{f'^2}{\eta} d\eta. \quad (5.30)$$

Equation (5.30) represents the constraints for determining the model constants C and D . In order to compute their values, the self-similar shape function $f(\eta)$ is required.

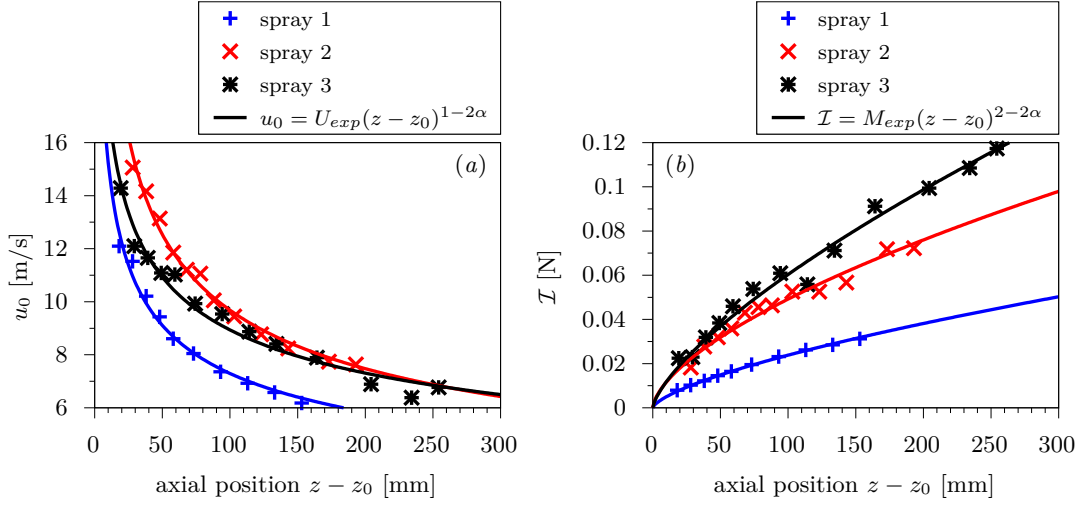


Figure 5.6: (a) Axial gas velocity on the spray axis as a function the axial position. (b) Axial evolution of the global gas momentum flow rate. The parameters of the fit curves are listed in table 5.1.

Figure 5.6(a) shows the velocity decrease along the spray axis, as introduced in section 5.3.1, and figure 5.6(b) depicts the axial evolution of the gas momentum flow rate, as discussed in section 5.3.2. In both cases, the fit curves, which relate to the mathematical description per (5.30), are in excellent agreement with the experimental data. The axial gas velocity decreases due to the widening of the flow field. The gas momentum flow rate increases with the axial distance from the orifice due to the momentum transfer from the liquid to the gas phase. The scaled experimental axial gas velocity profiles u/u_0 , as discussed in section 5.3.3, are depicted in figure 5.7. They collapse very well when plotted against the self-similar coordinate η/D , confirming the values obtained for α and z_0 . Minor deviations are observed for sprays 2 and 3 in the cross section closest to the atomizer (at $z/d_{or} = 38$). In this region, the self-similar behavior of the spray flow may not be fully developed yet. This is a well-known behavior of self-similar boundary-layer flows. In addition, the collapse of the radial gas velocity profiles is shown in figure 5.8. The radial gas velocity v is scaled with its axial dependency $(z - z_0)^{-\alpha}$, as defined in equation (5.18). In comparison to the self-similar axial gas velocity profiles, their scatter is larger due to the larger influence of the measurement uncertainty on the relatively small radial velocity components.

5.4 Self-similar shape function

The determination of the shape function $f(\eta)$ requires the coupled solution of the self-similar transformed z -momentum equation of the gas phase (5.16), together with the

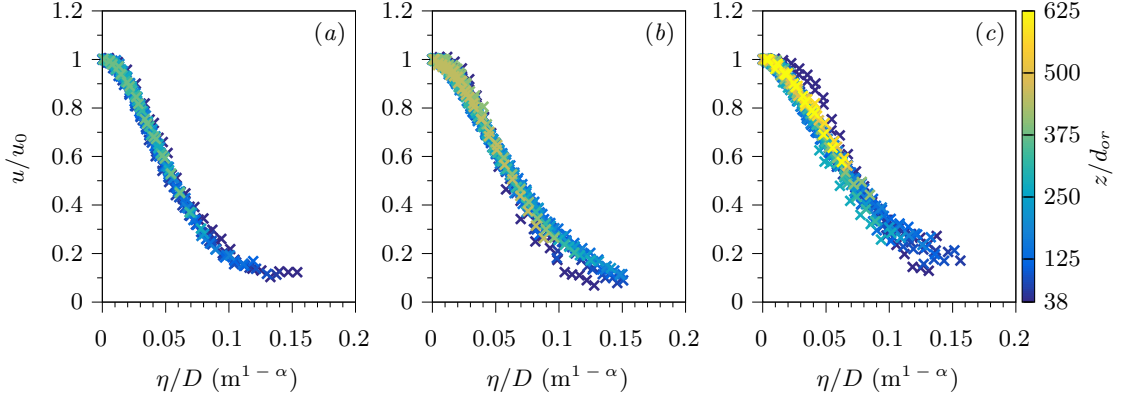


Figure 5.7: Self-similar profiles of the axial gas velocity for (a) spray 1, (b) spray 2 and (c) spray 3.

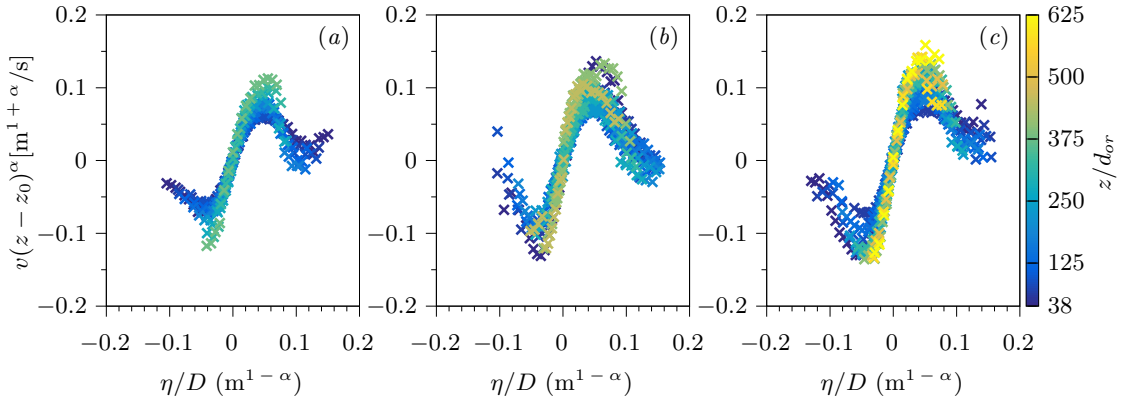


Figure 5.8: Self-similar profiles of the radial gas velocity for (a) spray 1, (b) spray 2 and (c) spray 3.

self-similar equivalents of the equations of motion of the liquid phase, (5.3) and (5.4). For this purpose, we require a functional description of the shape function $\Omega(\eta)$ of the momentum source term f_d . Such a description for $\Omega(\eta)$ could be deduced from the PDA measurement data. The determination of momentum fluxes from PDA data, however, is inaccurate, as known from the literature (Roisman and Tropea 2001; Bade and Schick 2011) and discussed in section 4.1.2 (see figure 4.9(a)). For this reason, we propose a different approach.

From the self-similar description of the axial gas velocity (5.17) follows that the scaled axial gas velocity profiles u/u_0 , as depicted in figure 5.7, relate to the self-similar shape function $f(\eta)$ per

$$\frac{u}{u_0} = \frac{1}{f''(0)} \frac{f'(\eta)}{\eta}. \quad (5.31)$$

	Spray 1	Spray 2	Spray 3
We_l	1395	2974	2921
Oh_l	0.0059	0.0059	0.0099
C [m ² /s]	0.00328	0.00511	0.00678
D [m ^{α} -1]	23.05	20.04	18.38

Table 5.2: Model parameters C and D obtained from (5.34) with the parameters listed in table 5.1.

As it turned out, the experimental self-similar velocity profiles are in fact best represented by the self-similar velocity profile obtained by Schlichting (1933) for the single-phase round jet. We therefore assume that the self-similar shape function $f(\eta)$ is of the form

$$f(\eta) = \frac{\eta^2}{1 + \eta^2/4}, \quad (5.32)$$

which yields the expression

$$\frac{u}{u_0} = \frac{1}{f''(0)} \frac{f'(\eta)}{\eta} = \frac{1}{(1 + \eta^2/4)^2} \quad (5.33)$$

for the self-similar axial gas velocity profile (5.31) (with $f''(0) = 2$).

Using the self-similar shape function (5.32), the constants C and D are calculated from (5.30) to

$$C = \frac{3}{8\pi} \frac{M_{exp}}{\rho U_{exp}}, \quad D = 2U_{exp} \sqrt{\frac{\pi}{3} \frac{\rho}{M_{exp}}}. \quad (5.34)$$

Their values are listed in table 5.2. The constant D corresponds to the width of the spray flow field. As indicated by equation 5.29, at a given axial position ($z - z_0$) and for given values of η and α , a smaller value of D yields a larger radial coordinate r . Thus, smaller values of D reflect a wider spray and vice versa. The value of D is smallest in spray 3 and largest in spray 1. Accordingly, it decreases with the Weber and the Ohnesorge number (see table 5.2). The constant C , together with the constant D , determines the velocity magnitude of the gas flow field as well as the strength of the momentum source term. C is proportional to the turbulent eddy viscosity of the gas phase, see equation (5.14), and therefore represents a diffusion coefficient, as indicated by its physical units. Its value is largest in spray 3 and smallest in spray 1 (see table 5.2). This implies that the value of C increases with the Weber and the Ohnesorge number.

With the values of the constant D known, the scaled axial gas velocity profiles of all three sprays (see figure 5.7) can be represented in a single diagram. Figure 5.9 depicts

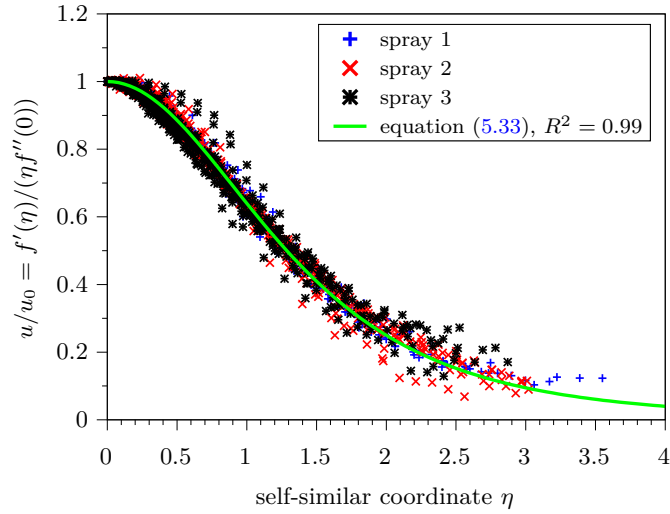


Figure 5.9: Universal self-similar axial gas velocity profile. Symbols: data from the experiments.

the universal self-similar axial gas velocity profile. The self-similar velocity profiles of all three sprays collapse excellently on the single profile given by the self-similar function (5.33), as indicated by the solid green line. As mentioned earlier, the deviations of some data points in sprays 2 and 3 correspond to the cross section closest to the orifice, where the self-similarity of the flow field may not be fully established yet.

It is interesting to note that streamlines $\Psi = \text{constant}$, see equation (5.15), are of similar shape in the present sprays and in the case without momentum transfer from the liquid phase, i.e. the single-phase round jet. In both cases, Ψ scales linearly with z and is proportional to the same self-similar shape function $f(\eta)$. The only difference emerges from different values of the constant C . Figure 5.10 depicts streamlines $\Psi = \text{constant}$ in spray 2. The value of Ψ corresponding to each streamline increases from left to right.

With the solution of the self-similar shape function $f(\eta)$ determined, the self-similar shape function of the momentum source term $\Omega(\eta)$ and the turbulent eddy viscosity ν_t remain the only unknowns in the self-similar transformed z -momentum equation (5.16). Thus, $\Omega(\eta)$ can be obtained from this equation as a function of $f(\eta)$. Before, we determine the turbulent eddy viscosity ν_t .

5.5 Turbulent eddy viscosity

We determine the turbulent eddy viscosity of the gas flow field from the PDA measurement data. The analysis is based on the Boussinesq eddy viscosity concept (Boussinesq 1877; Schmitt 2007), representing the turbulent (r, z) shear stress in boundary-layer

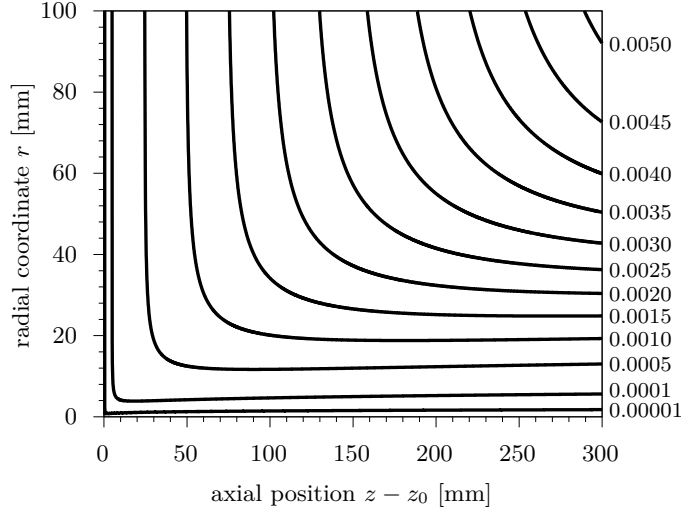


Figure 5.10: Streamlines (5.15) of the gas flow field in spray 2, calculated with the self-similar shape function (5.32). The value of Ψ , with the physical unit m^3/s , corresponding to each streamline, is given on the right-hand side of the diagram.

approximation as per

$$-\overline{u'v'} = \nu_t \frac{\partial u}{\partial r}. \quad (5.35)$$

The cross-correlation of the turbulent velocity fluctuations in axial and radial direction, is assumed as the product of the radial gradient of the mean axial gas velocity and ν_t . u' and v' denote the turbulent gas velocity fluctuations in the axial and radial directions, respectively. The cross-correlation $\overline{u'v'}$ is determined from the PDA measurement data by

$$\overline{u'v'} = \frac{\sum_{u=1}^U \sum_{v=1}^V \hat{n}_{uv} (u - u_{\underline{u}})(v - v_{\underline{v}})}{\sum_{u=1}^U \sum_{v=1}^V \hat{n}_{uv}}. \quad (5.36)$$

As in the determination of the mean gas velocity, see section 4.2, only the smallest drops with $d < 15 \mu\text{m}$ are considered in this analysis. We assume that these small drops represent the gas flow field, also under turbulent flow conditions. Therefore, in equation (5.36), \hat{n}_{uv} represents the Saffman-corrected number of drops with $d < 15 \mu\text{m}$ in the axial velocity class $u_{\underline{u}}$ with the radial velocity $v_{\underline{v}}$. The resulting experimental profiles of $\overline{u'v'}$ are depicted in figures 5.11(a,c,e). In all three sprays they are of the same order of magnitude. Their trends are similar as observed for the single-phase round jet (Hussein et al. 1994).

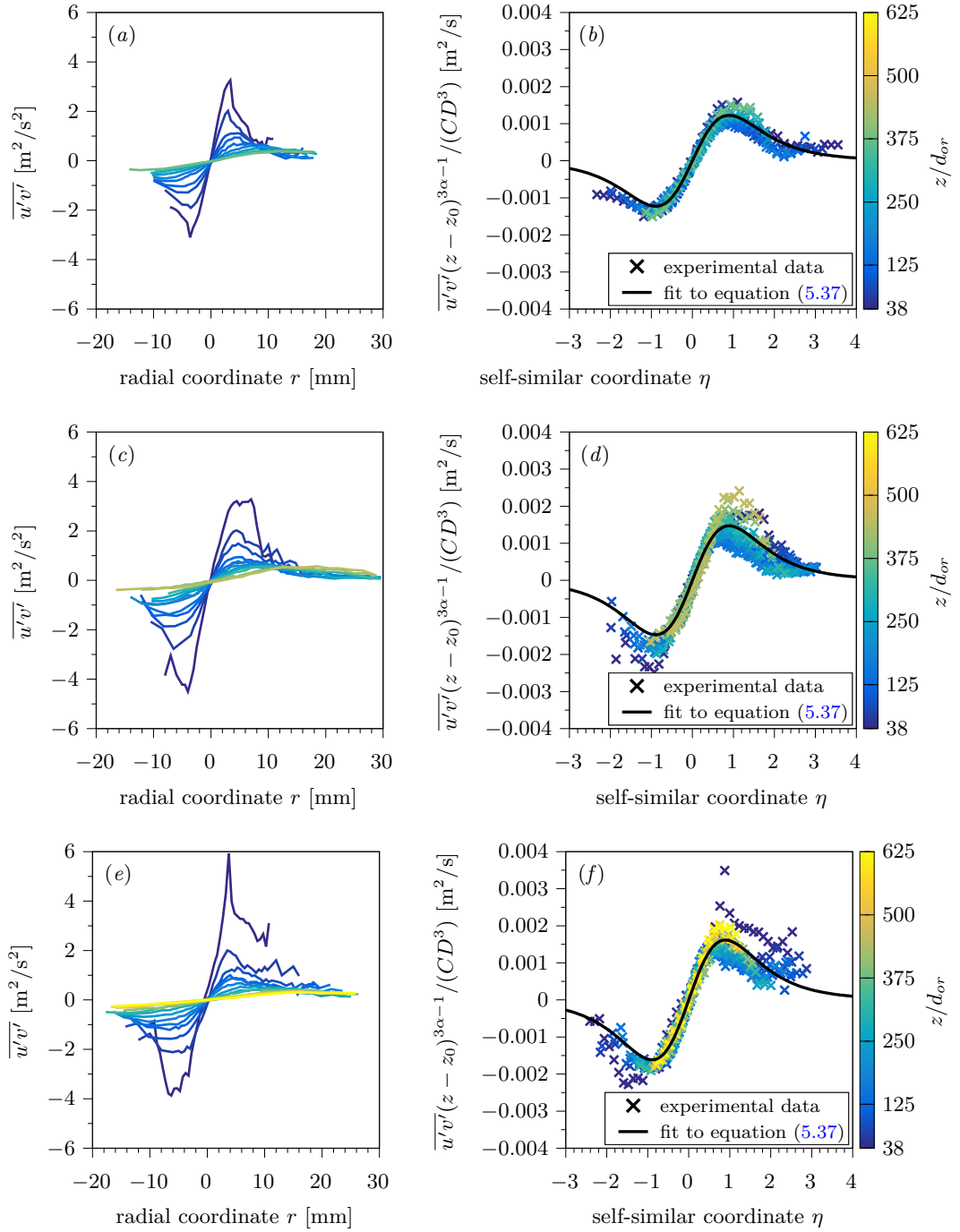


Figure 5.11: (a,c,e) Cross-correlation $\overline{u'v'}$ of the turbulent velocity fluctuations (5.36). (b,d,f) Self-similar cross-correlation of the turbulent velocity fluctuations. The black solid line corresponds to the best fit of $\nu_{t,exp}$ to the self-similar description (5.37). From top to bottom, the diagrams correspond to sprays 1, 2 and 3.

	Spray 1	Spray 2	Spray 3
$\nu_{t,exp}$ [m ² /s]	77.1 ν	92.5 ν	101.6 ν

Table 5.3: Turbulent eddy viscosity obtained from (5.37). The molecular viscosity of air at 20 °C has a value of $\nu = 15.4$ mm²/s.

Transforming (5.35) into the self-similar coordinate, we obtain

$$-\overline{u'v'} = \nu_t C D^3 (z - z_0)^{1-3\alpha} \left(\frac{f'}{\eta} \right)' \quad (5.37)$$

with the axial dependency of the cross-correlation of the turbulent velocity fluctuations on the axial coordinate given by $-\overline{u'v'} \propto (z - z_0)^{1-3\alpha}$. The cross-correlations calculated from the experimental data (equation (5.36), see figures 5.11(a,c,e)) are scaled with their axial dependency (5.37) and plotted in figures 5.11(b,d,f) against the self-similar coordinate η . The profiles collapse and match well the scaled radial gradient of the axial velocity. This confirms the earlier assumption of constant turbulent eddy viscosity. The experimental values of the turbulent eddy viscosity $\nu_{t,exp}$ are obtained by curve fitting of (5.37) to the scaled experimental data. The obtained results are listed in table 5.3. The values of $\nu_{t,exp}$ are two orders of magnitude larger than the molecular kinematic viscosity of air at 20 °C ($\nu = 15.4$ mm²/s), in a range reported for the single-phase round jet (Tennekes and Lumley 1972; Peters 1997).

5.6 Momentum source

Using the self-similar shape function $f(\eta)$, the model constants α , z_0 , C , and D , and the turbulent eddy viscosity ν_t determined in the previous sections 5.3 to 5.5, the shape function of the momentum source term $\Omega(\eta)$ remains the only unknown of equation (5.16). With the definition of the self-similar shape function $f(\eta)$, see (5.32), $\Omega(\eta)$ can be calculated from equation (5.16) as

$$\Omega(\eta) = \frac{2}{(1 + \eta^2/4)^4} \left[2(1 - 2\alpha) + \eta^2 + \frac{\nu_t}{C} (2 - \eta^2) \right]. \quad (5.38)$$

Depending on the values of the exponent α and the ratio ν_t/C , $\Omega(\eta)$ exhibits different shapes. This is illustrated in figures 5.12(a) and 5.12(b) for different values of α and ν_t/C , respectively. In the far field, i.e. $\eta \rightarrow \infty$, $\Omega(\eta)$ approaches zero. Depending on the values of α and ν_t/C , shapes with a local minimum at the spray axis (at $\eta = 0$) and an off-axis peak, or shapes with a single peak at the spray axis are obtained.

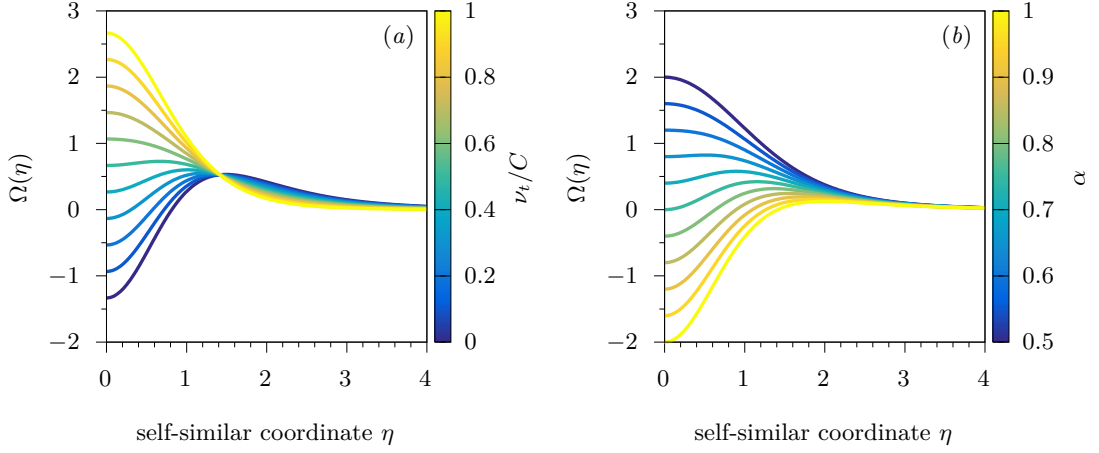


Figure 5.12: Self-similar shape function of the momentum source term (5.38) obtained with (a) $\alpha = 2/3$ and different values of ν_t/C , and (b) with $\nu_t/C = 1/2$ and a range of values of α .

To verify the theoretical description of the momentum-source shape function $\Omega(\eta)$, it is compared to measurement data. With the PDA data at hand, there are two options to determine the local gas momentum source. The first option is to compute the divergence of the drop momentum flow rate and balance it with the drag force, i.e. the momentum source term. The second option is to compute the momentum source by applying a single-drop drag law to each drop size class in the local ensemble and weight it with the local droplet-number concentration. In the following, we determine the momentum source according to both options and compare the resulting profiles to the self-similar description (5.38). As discussed earlier, flux terms calculated from PDA data are often inaccurate. As a consequence, the results obtained must be interpreted with care. We expect to obtain rather an estimate of the shape of the momentum source term from the measurements than an exact functional description.

5.6.1 Divergence of liquid momentum

The momentum source term is determined from the divergence of the axial drop momentum (5.4), where the change of liquid momentum in space is balanced by the source term. Since the momentum source is assumed to be self-similar, the two terms on the left-hand side of equation (5.4), which read

$$\Gamma_1 := \frac{\partial}{\partial z} \left(\sum_{\underline{d}=1}^{\underline{D}} \bar{u}_{l,\underline{d}} \phi_{z,\underline{d}} \right) \quad \text{and} \quad \Gamma_2 := \frac{1}{r} \frac{\partial}{\partial r} \left(r \sum_{\underline{d}=1}^{\underline{D}} \bar{u}_{l,\underline{d}} \phi_{r,\underline{d}} \right), \quad (5.39)$$

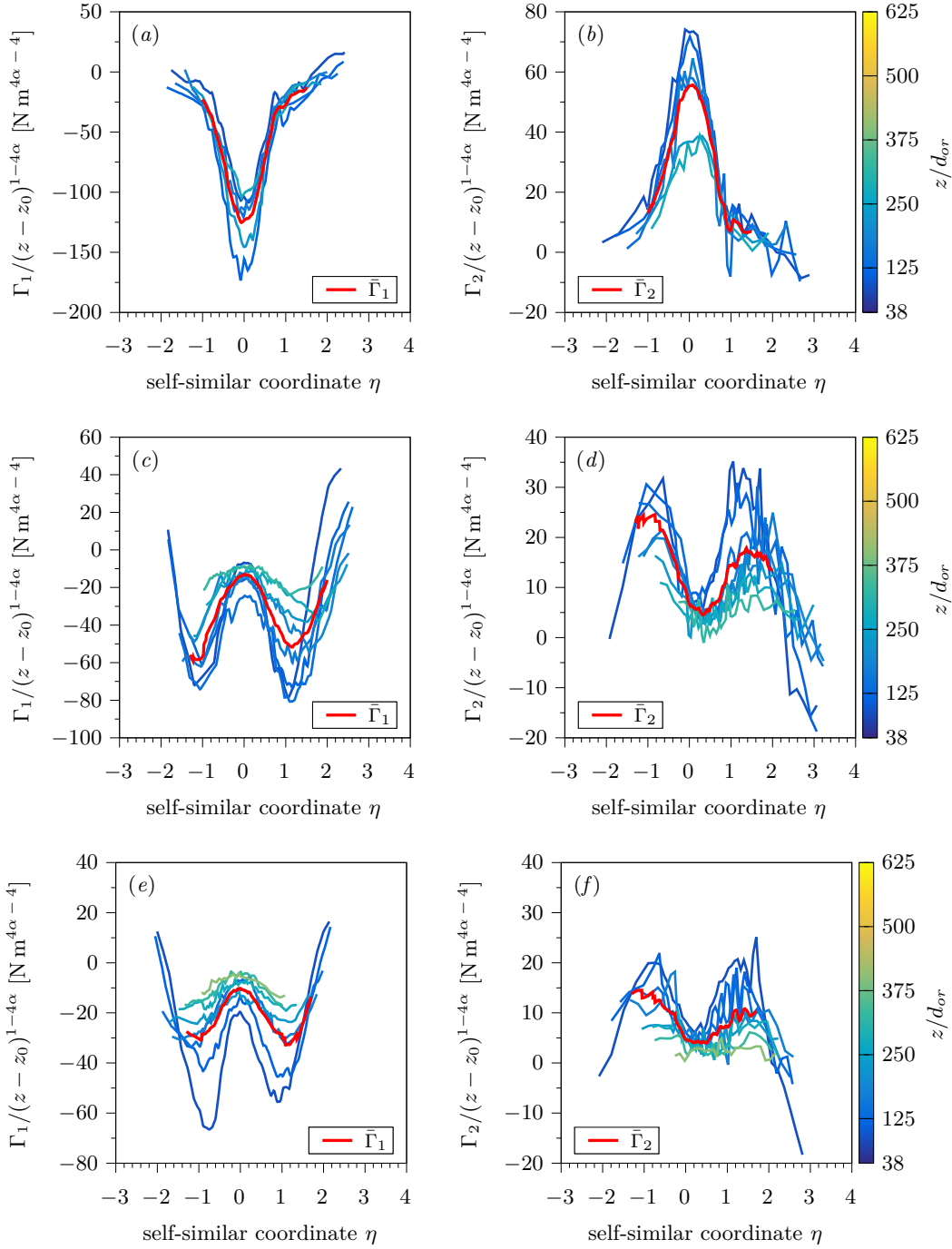


Figure 5.13: Self-similar profiles of (a,c,e) Γ_1 and (b,d,f) Γ_2 , as defined in (5.39), corresponding to the left-hand side of the liquid-phase z -momentum equation (5.4). The red line indicates the mean of the scaled profiles, denoted $\bar{\Gamma}_1$ and $\bar{\Gamma}_2$. Top: spray 1, center: spray 2 and bottom: spray 3.

must exhibit self-similarity as well. To collapse the profiles obtained for each of the two terms Γ_1 and Γ_2 , to a single self-similar profile, they are scaled with the axial dependency of the momentum source $(z - z_0)^{1-4\alpha}$, as required by the self-similar ansatz (5.15). In figures 5.13(a,c,e), the scaled profiles of Γ_1 , and in figures 5.13(b,d,f), the scaled profiles of Γ_2 , are plotted against the self-similar coordinate η . From top to bottom, the results correspond to sprays 1, 2 and 3. In view of the mentioned inaccuracies inherent to the calculation of momentum fluxes from PDA measurement results, and the fact that the axial and radial contributions of the flux terms to the divergence are evaluated as ratios of differences to calculate Γ_1 and Γ_2 , the profiles collapse well, confirming the self-similar behavior of the liquid phase. In each diagram, the red line indicates the mean of the scaled profiles, denoted by $\bar{\Gamma}_1$ and $\bar{\Gamma}_2$, respectively.

From equations (5.4) and (5.15) follows the experimental profile of the self-similar shape function of the momentum source term as

$$\Omega_{exp}^{(a)}(\eta) = -\frac{\bar{\Gamma}_1 + \bar{\Gamma}_2}{\rho C^2 D^4}, \quad (5.40)$$

which is depicted in figure 5.14 for the three sprays. The profile of spray 1 is approximately bell-shaped and exhibits a peak at the spray axis. This shape corresponds to the atomization of the not fully open tulip-stage liquid sheet. In sprays 2 and 3, the experimental profiles of $\Omega_{exp}^{(a)}(\eta)$ have an off-axis peak, with a local minimum at the spray axis. This agrees with the regime of atomization in these two sprays, as discussed in section 4.1.1. Note that the magnitudes of the profiles cannot be compared directly between the three sprays. This is due to the uncertainties associated with the determination of momentum fluxes from PDA data, which differ between the three sprays, as discussed in section 4.1.2.

5.6.2 Single-drop drag law

The momentum source term is determined from the total aerodynamic drag force acting on the average number of droplets at the local position. The drag force acting on a single spherical drop p , moving relative to its ambient medium, can be calculated from (Cossali 2001)

$$F_{d,p} = 3\pi\mu d_p \left(1 + \frac{1}{6} Re_p^{2/3}\right) (u - u_{l,p}), \quad (5.41)$$

where the drop Reynolds number is defined as

$$Re_p = \frac{d_p |u - u_{l,p}|}{\nu}. \quad (5.42)$$

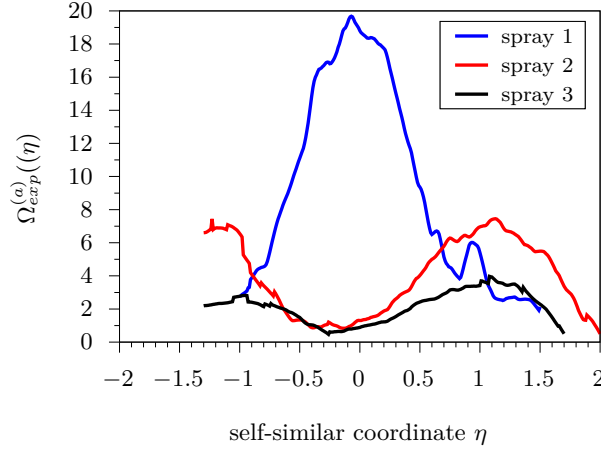


Figure 5.14: Experimental self-similar shape function of the momentum source term (5.40), determined from the divergence of the axial liquid momentum flow rate.

With the drop-number concentration c_n obtained from the PDA measurements, see figures 4.6(a,c,e), the drag force per unit volume relates to the momentum source of the gas phase per

$$\rho f_d = - \sum_{\underline{d}=1}^{\underline{D}} c_{n,\underline{d}} F_{d,\underline{d}}. \quad (5.43)$$

Here, $c_{n,\underline{d}}$ is local drop-number concentration in drop size class $d_{\underline{d}}$ and $F_{d,\underline{d}}$ denotes the average drag force acting on a drop in this size class. Consequently, the local momentum source term reads

$$f_d = -3\pi\nu \sum_{\underline{d}=1}^{\underline{D}} c_{n,\underline{d}} d_{\underline{d}} \left(1 + \frac{1}{6} Re_{\underline{d}}^{2/3} \right) (u - u_{l,\underline{d}}), \quad (5.44)$$

where $u_{l,\underline{d}}$ represents the mean axial drop velocity in drop size class $d_{\underline{d}}$. This representation of f_d does not consider the contribution of the radial velocity component to the drag force, since it is expected to be negligible.

We compute f_d from (5.44) in each cross section and scale it with the axial dependency $(z - z_0)^{1-4\alpha}$ required by the self-similar ansatz (5.15). Figure 5.15 shows the resulting profiles as a function of the self-similar coordinate η . The profiles collapse reasonably well, again confirming the self-similarity of the momentum source. The mean of the scaled profiles $f_d/(z - z_0)^{1-4\alpha}$ is denoted by \bar{f}_d and depicted by the red line. The experimental

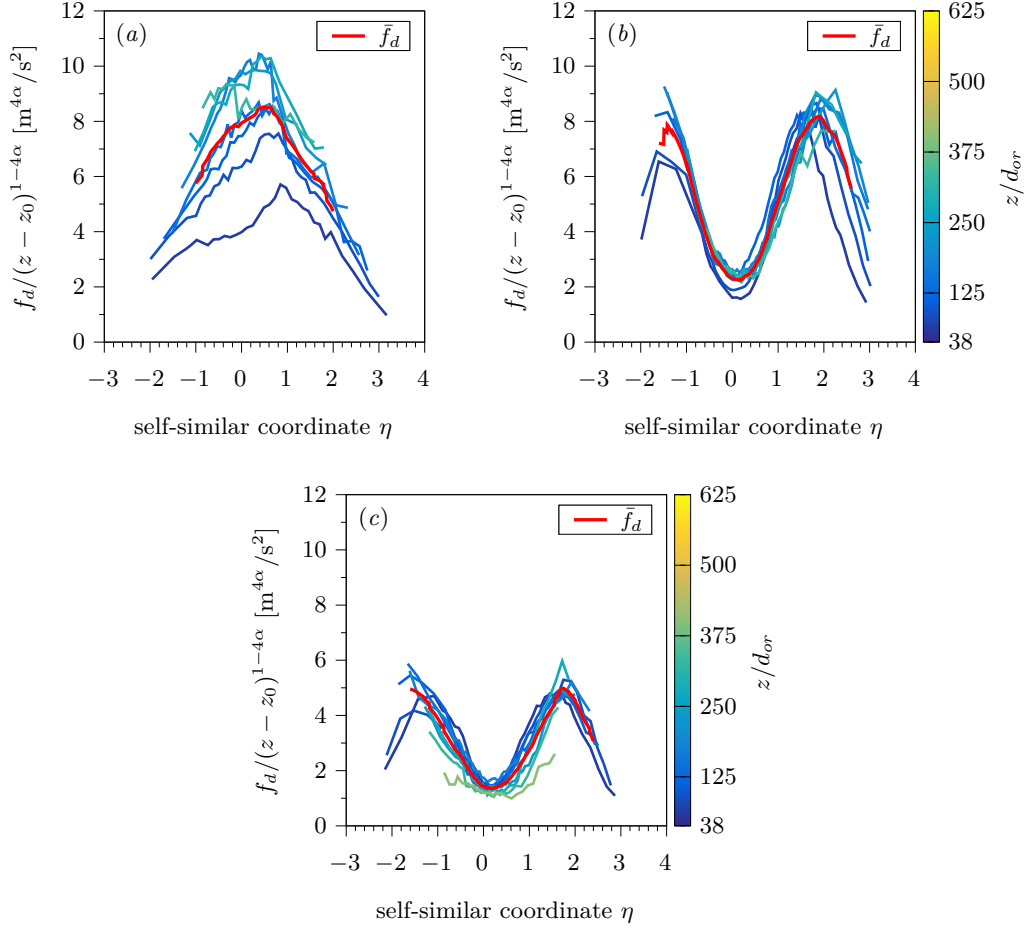


Figure 5.15: Self-similar profiles of the momentum source (5.44). The red line, denoted by \bar{f}_d , indicates the mean of the scaled profiles. (a) Spray 1, (b) spray 2 and (c) spray 3.

profiles of the self-similar shape function of the momentum source are calculated from

$$\Omega_{exp}^{(b)}(\eta) = \frac{\bar{f}_d(\eta)}{C^2 D^4}. \quad (5.45)$$

Figure 5.16 depicts the self similar shape functions of the momentum source obtained from (5.45). Their trends are similar to those obtained from the divergence of the liquid momentum flow rate (see figure 5.14). However, in the profiles obtained with the single-drop drag law, the off-axis peaks in sprays 2 and 3 appear at slightly larger values of η . In spray 1, the decrease of $\Omega_{exp}^{(b)}(\eta)$ with increasing η is less pronounced as in the profile reported in figure 5.14.

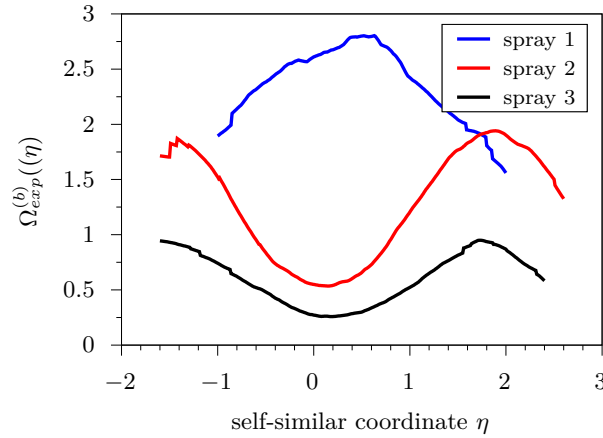


Figure 5.16: Experimental self-similar shape function of the momentum source term (5.45), determined by the application of a single-drop drag law.

5.6.3 Comparison

The analytical expression of the self-similar shape function of the momentum source (5.38) is compared to the experimental shape functions, as obtained in the previous sections 5.6.1 and 5.6.2. In Figure 5.17, the experimental shape functions of the momentum source are depicted by dotted and dashed lines, corresponding to equations (5.40) and (5.45), respectively. Since we are interested in the shape of the profiles only, they are rescaled to meet the analytical solution. This is required, due to the earlier discussed inaccuracies in the determination of momentum fluxes from PDA data. Table 5.4 lists the scaling factors applied to the experimental profiles of each spray, depending on the method it was determined. Their values are in a range reported by others (Tropea 2011; Bade and Schick 2011). The overestimation of the source term appears less pronounced by the results obtained on the basis of the single-drop drag law. The corresponding analytical profiles of $\Omega(\eta)$, given by equation (5.38), are depicted in figure 5.17 as solid lines. At large radial coordinates, i.e. large values of η , they approximately capture the trend of the experimental profiles. However, close to the sprays axis, around $\eta = 0$, the profiles deviate. In sprays 2 and 3, $\Omega(\eta)$ even exhibits negative values, indicating momentum transfer from the gas to the liquid phase. This is not physical in the present sprays, since momentum transfer goes from the liquid to the gas phase exclusively.

This discrepancy can be explained by the underestimation of the turbulent eddy viscosity of the gas phase ν_t based on the PDA data. After increasing the experimentally obtained values of $\nu_{t,exp}$ by 50%, effectively increasing the ratio ν_t/C in equation (5.38), the experimental and analytical profiles agree reasonably well. This is shown in figure 5.18 for (a) spray 1, (b) spray 2 and (c) spray 3. In each diagram, the experimental

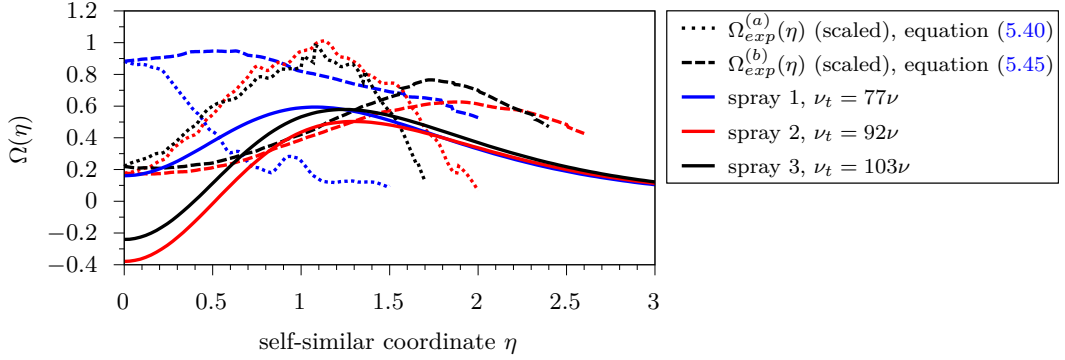


Figure 5.17: Self-similar shape functions of the momentum source obtained from the self-similar description (5.38) (solid lines) and estimated from PDA data (dotted and dashed lines). The scaling factors are listed in table 5.4.

	Spray 1	Spray 2	Spray 3
Scaling factor for $\Omega_{exp}^{(a)}(\eta)$ obtained by equation (5.40)	21.3	7.4	4.0
Scaling factor for $\Omega_{exp}^{(b)}(\eta)$ obtained by equation (5.45)	3.0	3.1	1.2

Table 5.4: Scaling factors for the experimental profiles of the momentum source. They are required due to the overestimation of momentum fluxes by PDA measurement data.

profiles are depicted as gray and black solid lines. The mathematical description (solid red line) exhibits the same trends as observed in the corresponding experimental profiles and agrees very well with the mean of the two experimental profiles (dashed black line) in all three cases. Their underestimation of $\nu_{t,exp}$ is attributed to the fact, that it is determined from the velocity fluctuations of the smallest droplets in the sprays, which, however, cannot be considered as perfect tracer particles. Due to their finite mass, they can follow turbulent fluctuations only up to a threshold fluctuation frequency. As a consequence, we only observe the fluctuations of large-scale turbulent structures, resulting in values of $\nu_{t,exp}$ in the correct order of magnitude. High-frequency turbulent fluctuations in the turbulent energy spectrum, however, are not captured. This phenomenon, justifying the increase of $\nu_{t,exp}$ by 50%, is analyzed in detail in the following section.

5.6.4 Underestimation of the turbulent eddy viscosity

The motion of a liquid drop in an ambient gaseous medium is governed by the Stokes number (see section 4.2). Drops with $St < 1$ quickly adapt to changes in the motion of the ambient phase and may be used as tracer particles to determine the magnitude of its mean motion. For drops to represent the turbulent motion of the gas phase, even the high-frequency turbulent fluctuations, their Stokes number is required to be much smaller

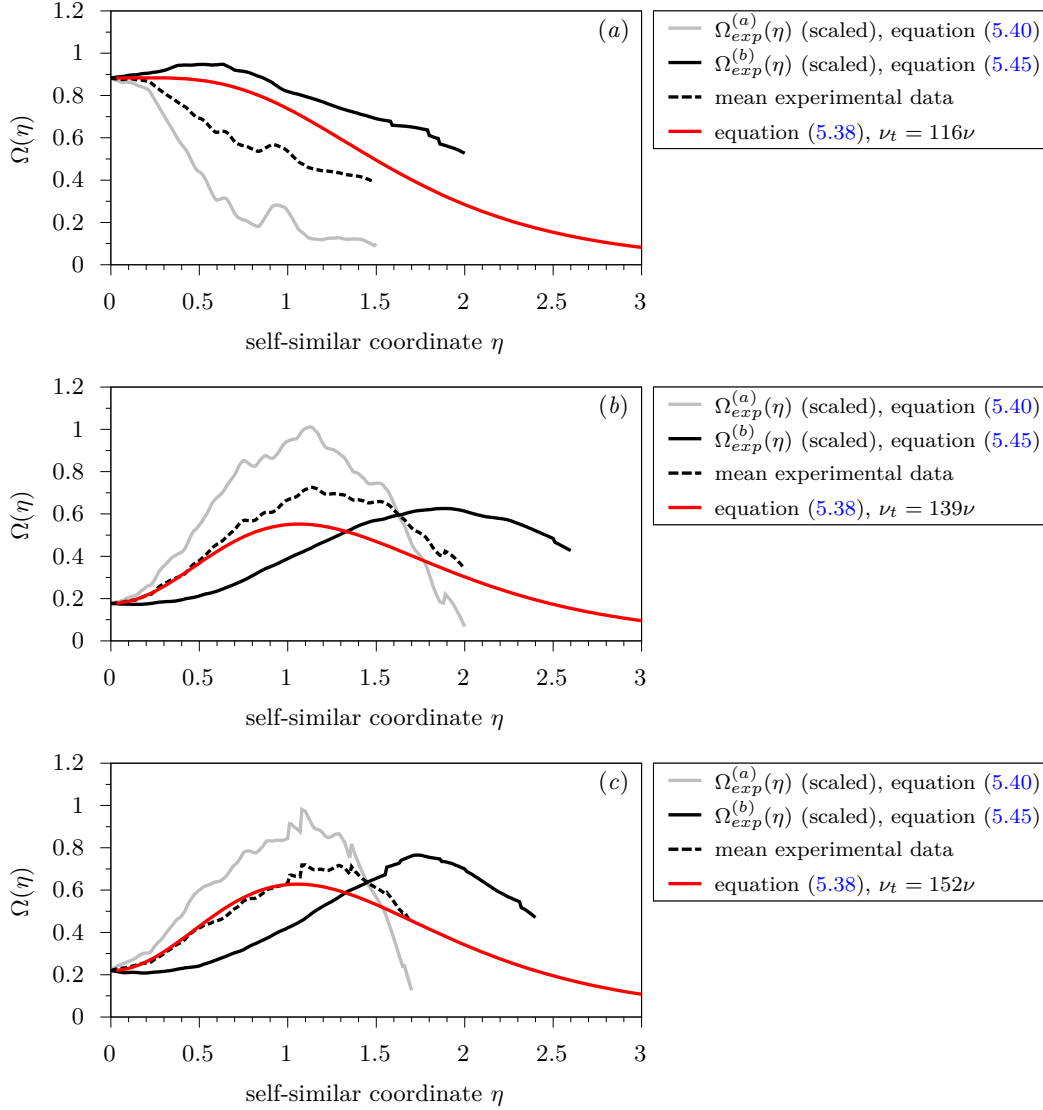


Figure 5.18: Self-similar shape function of the momentum source term (5.38) (red solid line) of (a) spray 1, (b) spray 2 and (c) spray 3, obtained after increasing the turbulent eddy viscosity $\nu_{t,exp}$ by 50%. The scaling factors for the experimental profiles (black and gray solid lines) are listed in table 5.4. The dashed black line depicts the mean of the two scaled experimental profiles.

than unity, $St \ll 1$. To determine to which extent the drops used as tracer particles in the present sprays represent the turbulent motion of the gas phase, we follow the analysis of Chao (1964). In this way, we analyze if the drops used to determine the cross-correlation $\overline{u'v'}$, and therefore the turbulent eddy viscosity ν_t , see equation (5.37), fully represent all frequencies of the gas-phase turbulent energy spectrum, yielding the correct value of ν_t .

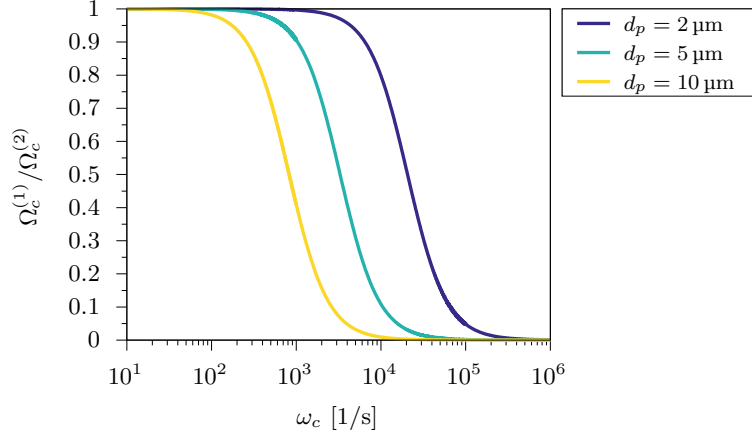


Figure 5.19: Spectral energy ratio (5.48) according to the work of Chao (1964) for spherical water droplets of different size in ambient air.

In his work, Chao (1964) analyzed the transport behavior of a single particle in a dilute turbulent suspension. He solved a linearized Lagrangian equation, describing the particle motion in a turbulent flow field, by means of a Fourier transformation. The obtained expression for the particle velocity allows the determination of the kinetic energy ratio of a given particle, in a given continuous phase, as a function of the turbulent fluctuation frequency of the continuous phase. The kinetic energy ratio of the particle provides a measure for the ability of the particle to follow closely the turbulent fluctuations of the ambient phase. Its derivation is discussed below.

The analysis is based on the assumption of a locally uniform flow field near the particle. The expression obtained for the Fourier-transformed particle velocity $u_{p,c}$ reads (Chao 1964)

$$u_{p,c} = \frac{[\alpha_c + (3\alpha_c\omega_c/2)^{1/2}] + i[\omega_c + (3\alpha_c\omega_c/2)^{1/2}]}{[\alpha_c + (3\alpha_c\omega_c/2)^{1/2}] + i[\omega_c/\beta_c + (3\alpha_c\omega_c/2)^{1/2}]} u_c. \quad (5.46)$$

The subscript c in these variables refers to the work of Chao (1964). $u_{p,c}$ is proportional to the Fourier-transformed velocity of the continuous phase u_c , i.e. the gas phase in the present sprays, and depends on two constant parameters, α_c and β_c , as well as the turbulent angular fluctuation frequency ω_c . i denotes the imaginary unit. The parameters α_c and β_c depend on properties of the particle and the continuous phase, and are defined as (Chao 1964)

$$\alpha_c = \frac{3\nu}{d_p^2} \quad \text{and} \quad \beta_c = \frac{3\rho}{2\rho_p + \rho}. \quad (5.47)$$

Here, ρ_p and ρ are the densities of the particle and the continuous phase, respectively. ν denotes the molecular kinematic viscosity of the continuous phase and d_p is the particle diameter. Thus, β_c may be interpreted as a density ratio, whereas α_c has the dimension of a frequency.

With the conjugate complex Fourier-transformed velocities $u_{p,c}^*$ and u_c^* , one can calculate the ratio of the spectral kinetic energies (Chao 1964)

$$\frac{u_{p,c}u_{p,c}^*}{u_cu_c^*} = \frac{\Omega_c^{(1)}}{\Omega_c^{(2)}}, \quad (5.48)$$

with (Chao 1964)

$$\Omega_c^{(1)} = \left(\frac{\omega_c}{\alpha_c}\right)^2 + \sqrt{6}\left(\frac{\omega_c}{\alpha_c}\right)^{3/2} + 3\left(\frac{\omega_c}{\alpha_c}\right) + \sqrt{6}\left(\frac{\omega_c}{\alpha_c}\right)^{1/2} + 1 \quad (5.49)$$

and (Chao 1964)

$$\Omega_c^{(2)} = \frac{1}{\beta_c^2}\left(\frac{\omega_c}{\alpha_c}\right)^2 + \frac{\sqrt{6}}{\beta_c}\left(\frac{\omega_c}{\alpha_c}\right)^{3/2} + 3\left(\frac{\omega_c}{\alpha_c}\right) + \sqrt{6}\left(\frac{\omega_c}{\alpha_c}\right)^{1/2} + 1. \quad (5.50)$$

The spectral energy ratio $\Omega_c^{(1)}/\Omega_c^{(2)}$ is a measure for the ability of a particle to exhibit turbulent fluctuations at a given turbulent fluctuation frequency ω_c . For $\Omega_c^{(1)}/\Omega_c^{(2)} = 1$, the instantaneous particle velocity perfectly agrees with the instantaneous velocity of the continuous phase. At ratios lower than unity, there is a slip velocity between the particle and the continuous phase because the particle oscillates at a frequency different from the continuous phase. A ratio of zero indicates that the turbulent fluctuations at this frequency are too weak to influence the motion of the particle. For illustration, figure 5.19 depicts $\Omega_c^{(1)}/\Omega_c^{(2)}$ as a function of the angular turbulent frequency ω_c for spherical water droplets of different diameters in ambient air. For a given drop diameter, at low frequencies ω_c , the spectral energy ratio is unity. With increasing ω_c , the spectral kinetic energy ratio decreases and approaches zero. For smaller drops, $\Omega_c^{(1)}/\Omega_c^{(2)}$ approaches zero at higher frequencies ω_c . This implies that smaller droplets may follow turbulent fluctuations of higher frequencies, which was to be expected due to their lower mass.

To determine to which extent the smallest drops in the present sprays can follow the turbulent fluctuations of the gas phase tightly, we need to estimate the fluctuation frequencies of the smallest turbulent structures, i.e. the highest turbulent fluctuation frequencies, occurring in the flow field. The smallest scales in turbulent flow are defined by the Kolmogorov microscales (Pope 2000). At this scale, the viscous forces dominate,

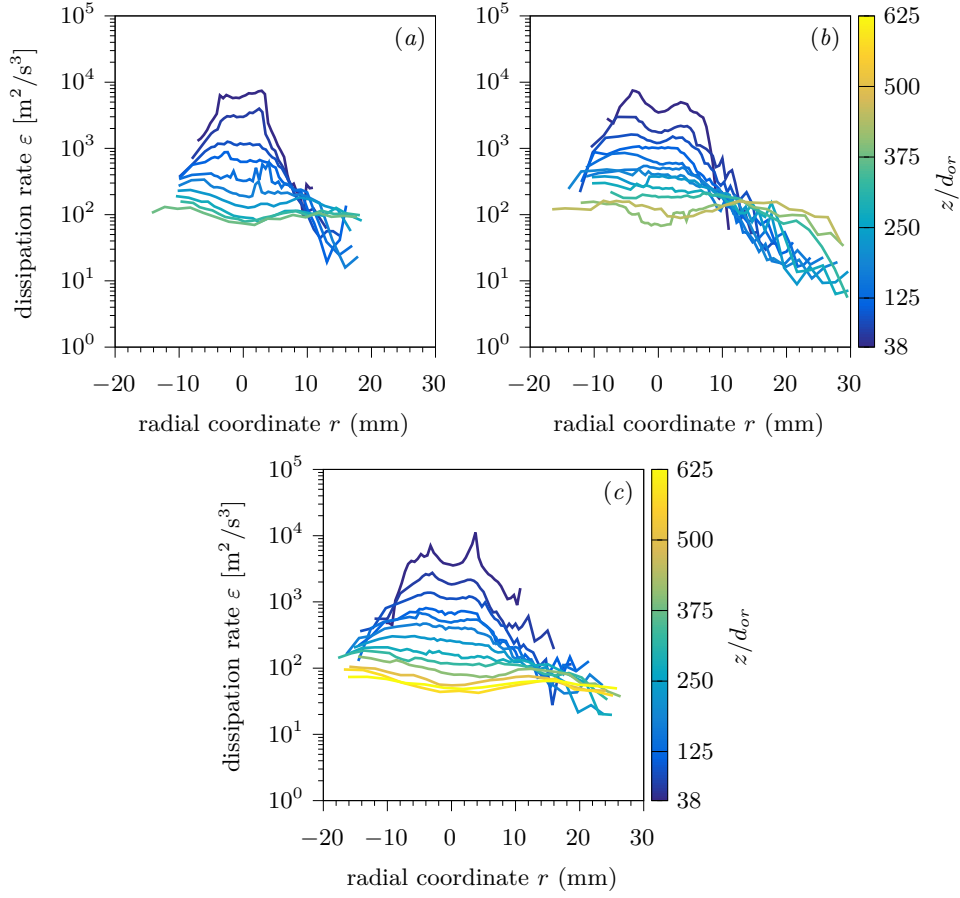


Figure 5.20: Viscous dissipation rate according to (5.56) in (a) spray 1, (b) spray 2 and (c) spray 3.

dissipating the turbulent kinetic energy into heat. The Kolmogorov time scale is defined as

$$\tau_\mu = \left(\frac{\nu}{\varepsilon} \right)^{1/2} \quad (5.51)$$

and depends on the kinematic viscosity ν and the viscous dissipation rate per unit mass ε . On the other hand, the characteristic turbulence time scale is given by the eddy turnover time (Pope 2000), which is considered as the time scale of large-scale turbulent structures. It is defined by

$$\tau_t = \frac{k}{\varepsilon}, \quad (5.52)$$

where k denotes the turbulent kinetic energy. Naturally, the eddy turnover time scale is larger than the Kolmogorov time scale.

The calculation of the characteristic time scales (5.51) and (5.52) in the spray flow fields requires the viscous dissipation rate ε and the turbulent kinetic energy k . We calculate the latter by

$$k = \frac{1}{2} (\overline{u'^2} + 2\overline{v'^2}) , \quad (5.53)$$

where the mean squared velocity fluctuations in radial direction $\overline{v'^2}$ are multiplied by two to account for the velocity fluctuations in azimuthal direction. $\overline{u'^2}$ and $\overline{v'^2}$ are computed from the PDA measurement data, similar to the cross-correlation $\overline{u'v'}$, as defined in equation (5.36). Again, only drops with $d < 15 \mu\text{m}$, representing the mean gas velocity (see section 4.2), are considered for this analysis. Assuming local equilibrium between production and dissipation, $\mathcal{P} = \varepsilon$, so that

$$-\overline{u'v'} \frac{\partial u}{\partial r} = \varepsilon , \quad (5.54)$$

and an approximately constant ratio

$$C_\mu^{1/2} = \frac{\overline{u'v'}}{k} \approx 0.3 , \quad (5.55)$$

the viscous dissipation rate ε can be estimated recalling the eddy viscosity ansatz (5.35) as

$$\varepsilon = C_\mu \frac{k^2}{\nu_t} , \quad (5.56)$$

with the empirical constant $C_\mu = 0.09$ (Pope 2000). The profiles obtained for the viscous dissipation rates in the three sprays are shown in figure 5.20. In a given cross section, ε is of approximately constant value, except near the edge of the spray, where its values are lower. Moreover, it decreases with increasing axial distance from the orifice. We take the largest value of ε occurring in each cross section, ε_{max} , and plot it against the axial distance from the virtual origin, as shown in figure 5.21. This axial evolution of the viscous dissipation rate is compared to the experimental results of Friehe et al. (1971), who found the following relation for the dissipation rate in the self-similar region of turbulent single-phase round jets (Su 1998)

$$\varepsilon = 0.075 \frac{u_0^3}{\delta_{0.05}} . \quad (5.57)$$

$\delta_{0.05}$ denotes the full width of the jet at the 5% points of the axial velocity profile. The

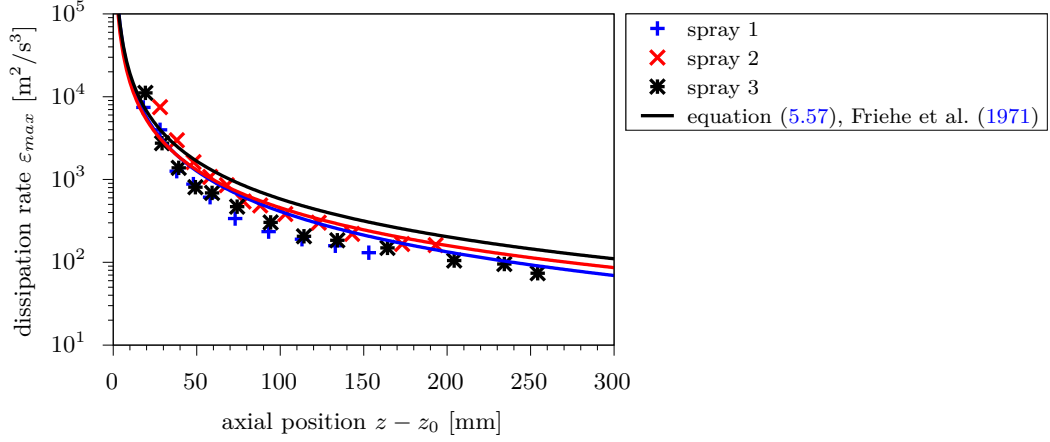


Figure 5.21: Axial evolution of the viscous dissipation rate. The data points correspond to the three sprays and the solid lines correspond to expression (5.57), obtained by Friehe et al. (1971) and Su (1998).

full width for the present sprays can be determined from equation (5.33) by solving

$$\frac{u}{u_0} = \frac{1}{(1 + \eta^2/4)^2} := \frac{5}{100} \quad (5.58)$$

for η . Consequently, the full width of the gas flow fields in the sprays reads

$$\delta_{0.05}(z) = \frac{4}{D} (2\sqrt{5} - 1)^{1/2} (z - z_0)^\alpha. \quad (5.59)$$

Although derived for the single-phase round jet, (5.57) shows good agreement with the dissipation rate in the present sprays (see figure 5.21), calculated from (5.56). This indicates universal small-scale behavior of fully developed turbulence in this type of free shear flow, which is described by the parameters u_0 and $\delta_{0.05}$ exclusively. Note that the relation (5.57) implies that the viscous dissipation rate scales with $\varepsilon \propto (z - z_0)^{3-7\alpha}$. In the present two-phase spray flow, ε decreases more slowly than in the case of the single-phase round jet, where, with $\alpha = 1$, $\varepsilon \propto (z - z_0)^{-4}$ is obtained (Djenidi et al. 2016).

With the dissipation rate ε_{max} known, the turbulent time scales (5.51) and (5.52) of the spray flow fields can be determined. Their values are depicted in figure 5.22 as functions of the axial position. Both time scales increase with the axial distance from the orifice, reflecting the decrease of the viscous dissipation rate. The turbulence time scale of large-scale structures, τ_t , is more than an order of magnitude larger than the Kolmogorov time scale, τ_μ , representing the smallest turbulent structures. The inverse of the time scales yields the corresponding fluctuation frequencies.

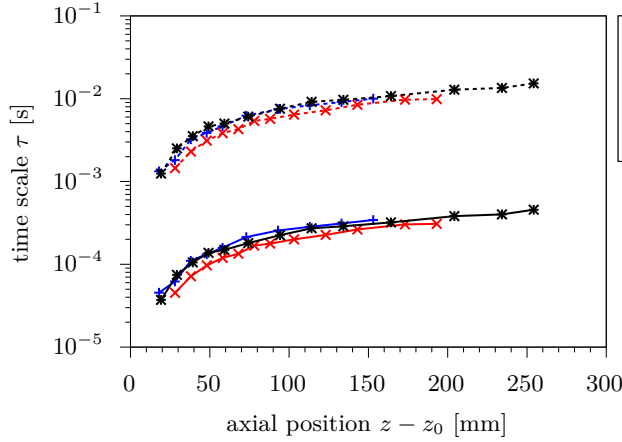


Figure 5.22: Turbulent time scales of the gas flow field, τ_μ and τ_t , obtained from (5.51) and (5.52), respectively.

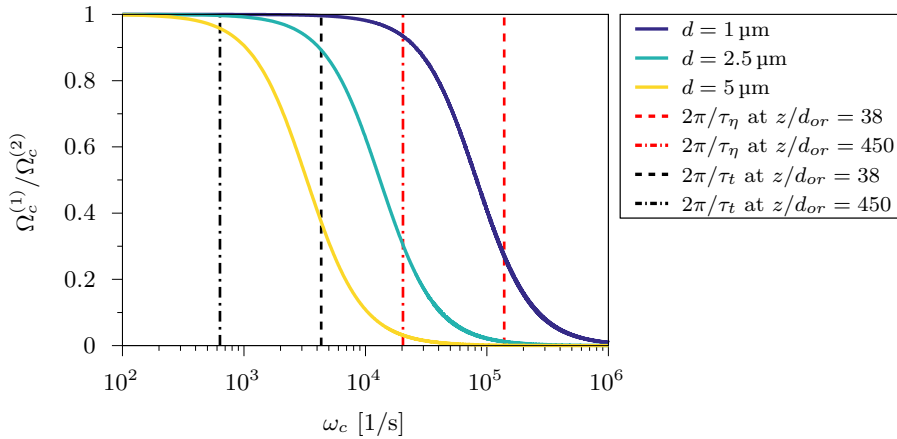


Figure 5.23: Spectral energy ratio (5.48) according to the work of Chao (1964), for droplets of different size in spray 2. The dashed and dash-dotted lines indicate the fluctuation frequencies at the Kolmogorov time scale τ_μ (red lines) and at the turbulence time scale τ_t (black lines), respectively.

The values of the turbulent eddy viscosity $\nu_{t,exp}$ were obtained from the cross correlation of the velocity fluctuations $\overline{u'v'}$ of the smallest drops in the sprays (see section 5.5). For this purpose, the same measurement data was used as for the determination of the mean gas velocity (see section 4.2), namely the data of drops with diameter $d < 15 \mu\text{m}$. The smallest drop size class included drops with diameters $0 < d < 5 \mu\text{m}$. Figure 5.23 shows the spectral energy ratios (5.48), as obtained from the mathematical formulation of Chao (1964), for drops of different diameter in spray 2. The kinetic energy ratios for drops with

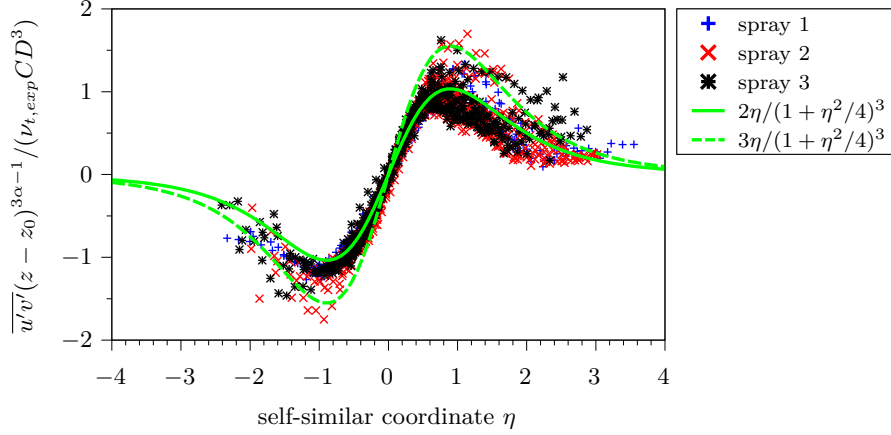


Figure 5.24: Self-similar profile of the cross-correlation $\overline{u'v'}$. The solid line indicates the corresponding self-similar description obtained from equation (5.37). The dashed line illustrates the relation between the self-similar description and the experimental data when $\nu_{t,exp}$ is increased by 50%, as required by the mathematical description of the momentum source.

the mean diameter and the upper limit of the smallest drop size class, i.e. $d = 2.5 \mu\text{m}$ and $d = 5 \mu\text{m}$, respectively, and for much smaller drops with $d = 1 \mu\text{m}$, are depicted. The vertical lines denote the large-scale and the small-scale turbulent fluctuation angular frequencies obtained from the respective time scales τ_t and τ_μ (see figure 5.22). For each time scale, two lines are depicted. One corresponds to a cross section very close to the atomizer and the other to a cross section farther downstream. Drops of $5 \mu\text{m}$ in diameter are representative for fluctuation frequencies in the turbulent energy spectrum of up to $\omega_c = 10^3 \text{ Hz}$. Smaller drops with $d = 2.5 \mu\text{m}$, fully capture turbulent fluctuations up to frequencies in an order of magnitude corresponding to the large-scale turbulence time scale. However, for fluctuations at the Kolmogorov scales, the spectral energy ratio $\Omega_c^{(1)}/\Omega_c^{(2)}$ is close to zero for a drop of this size. As a consequence, even smaller droplets, i.e. tracer particles of $d < 1 \mu\text{m}$, would be required to fully resolve turbulent fluctuations at the smallest scales. Hussein et al. (1994) used droplets of approximately $1 \mu\text{m}$ in diameter as tracer particles for laser-Doppler measurements in turbulent single-phase jet flow.

The analysis carried out in the present section strongly suggests that the values of the turbulent eddy viscosity $\nu_{t,exp}$, obtained from the present PDA data, are underestimated due to the relatively high inertia of the larger droplets used as tracer particles. The data captures large scale turbulent structures in the gas phase, resulting in values of $\nu_{t,exp}$ in the correct order of magnitude. In turn, small-scale turbulent fluctuations are not fully adopted by all the tracer particles used. An investigation of the exact magnitude of the underestimation of ν_t is beyond the scope of the present analysis. The

analytical expression for the shape function of the momentum source (5.38) suggests an underestimation by approximately 33 % (see figure 5.18), and therefore justifies the increase of the experimentally obtained values by 50 %, i.e. $\nu_t = 1.5\nu_{t,exp}$.

Figure 5.24 depicts the universal self-similar profile of the cross-correlation of the turbulent velocity fluctuations $\overline{u'v'}$ (solid line). The experimental data corresponds to the results presented in figure 5.11 and collapses reasonably well to the profile of the self-similar description (solid line). The dashed line illustrates the discrepancy between the turbulent eddy viscosity obtained from the experiments, $\nu_{t,exp}$, and the increased eddy viscosity $\nu_t = 1.5\nu_{t,exp}$, as required by the self-similar description of the momentum source.

The analytical self-similar description of the gas flow in the sprays is hereby fully consistent with the experimental data. In the next section, the scope and limitations of the self-similar model are discussed.

5.7 Scope and limitations

Based on PDA measurement data, a model for the self-similar description of the two-phase flow fields of pressure-atomized sprays was developed. It is built on an axisymmetric boundary-layer approximation of the gas flow field, accounting for momentum transfer from the liquid to the gas phase. As a consequence, the analytical description of the gas flow field is valid downstream from a certain distance of the atomizer only, where the self-similar behavior of the flow field is fully developed. This is connected to the slenderness of the flow field, required for the boundary-layer approximation to be applicable, and well known from other boundary-layer type flows (Schlichting and Gersten 2017). In the present case, the minimum distance from the atomizer where experimental data is available is $z/d_{or} = 38$. At this axial distance, the analytical description already agrees very well with the measurement data in spray 1 and exhibits small deviations in sprays 2 and 3 (see figures 5.7 and 5.9). This distance corresponds to approximately two times (spray 1) and three times (sprays 2 and 3) the breakup length of the liquid sheet (see figure 3.10).

The limit of the self-similar description downstream is set by the mathematical structure of the analytical solution. The main characteristic of the self-similar solution is the dependency of all flow field properties on the axial coordinate z following a power law $(z - z_0)^\kappa$. For the momentum flow rate of the gas phase through every plane $z = \text{constant}$, the exponent κ is given in equation (5.25) by $2 - 2\alpha$ and therefore positive (see figure 5.6(b)). Consequently, the momentum flow rate of the liquid phase must exhibit a negative exponent κ (see figure 4.9(b)). However, the increase of the gas momentum flow rate can only persist as long as the drop velocities are higher than the gas velocity. This fact sets the limit to the validity of the present self-similar description. Due to the

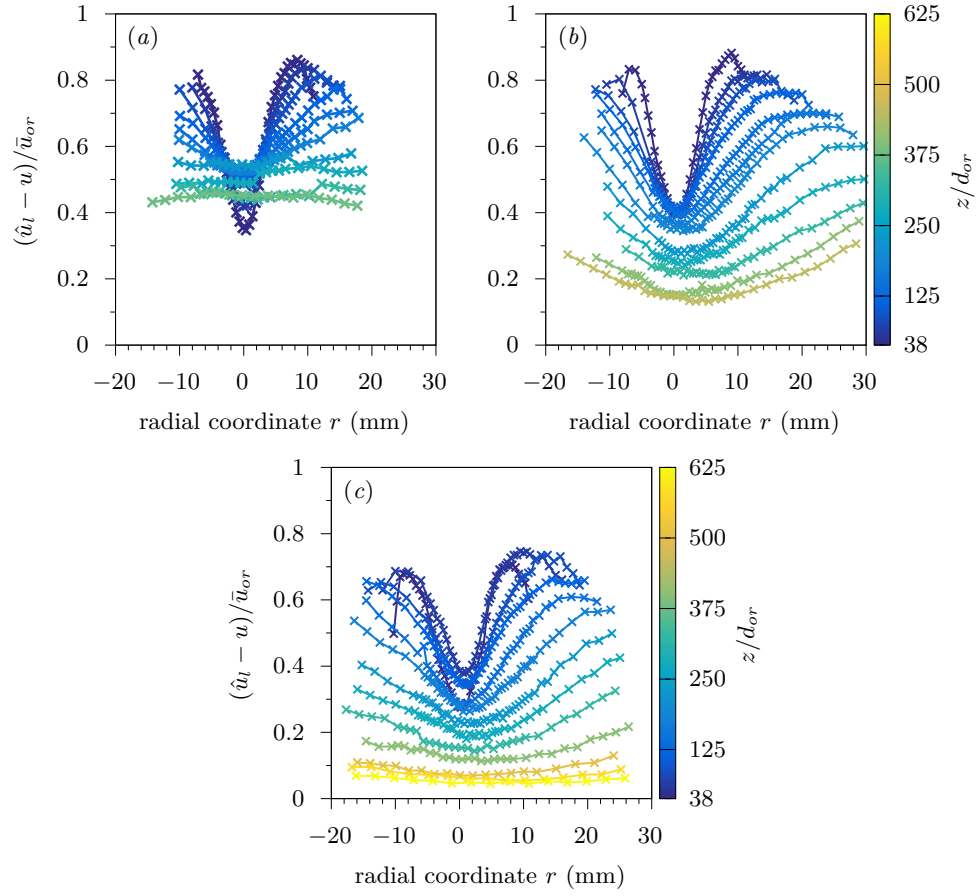


Figure 5.25: Downstream limitation criterion (5.60) of the self-similar description of the spray flow field. (a) Spray 1, (b) spray 2 and (c) spray 3.

nature of the solution in the form of a power law, this limit does not emerge from the asymptotics of the applied mathematical description.

As a limiting criterion we propose the difference of the volume-mean liquid velocity \hat{u}_l and the gas velocity u , normalized by the liquid velocity through the orifice \bar{u}_{or} , i.e.

$$\frac{\hat{u}_l(r, z) - u(r, z)}{\bar{u}_{or}} > 0, \quad (5.60)$$

where the volume-mean liquid velocity is calculated by

$$\hat{u}_l = \frac{\sum_{u=1}^U \sum_{d=1}^D u_{l,u} d_d^3 \psi_{ud}}{\sum_{u=1}^U \sum_{d=1}^D d_d^3 \psi_{ud}}. \quad (5.61)$$

	Spray 1	Spray 2	Spray 3
U_{exp} [$\text{m}^{2\alpha}/\text{s}$]	3.49	4.10	4.58
M_{exp} [$\text{kg m}^{2\alpha-1}/\text{s}^2$]	0.114	0.208	0.309
$\nu_{t,exp}$ [m^2/s]	77.1ν	92.5ν	101.6ν
α	0.66	0.69	0.65
z_0 [mm]	-3.0	-13.1	-4.2
C [m^2/s]	0.00328	0.00511	0.00678
D [$\text{m}^{\alpha-1}$]	23.05	20.04	18.38
ν_t [m^2/s]	$1.5\nu_{t,exp}$	$1.5\nu_{t,exp}$	$1.5\nu_{t,exp}$

Table 5.5: Summary of the model constants. The molecular viscosity of air at 20 °C has a value of $\nu = 15.4 \text{ mm}^2/\text{s}$.

Here, ψ_{ud} represents the drop number flux in the drop velocity class $u_{l,\underline{u}}$ with the diameter $d_{\underline{d}}$ (see section 3.2.2). As long as the ratio (5.60) is sufficiently larger than zero, momentum is transferred from the liquid to the gas phase. Thus, the downstream boundary of the self-similar model described by (5.60) is located at an axial position, where the velocity difference between the two phases is small compared to the mass-flux equivalent liquid velocity inducing the two-phase flow field. Figure 5.25 depicts the criterion (5.60) in the sprays investigated. Its values are well above zero, indicating that the self-similar theory holds. The ratio (5.60) decreases with increasing axial distance from the atomizer and its corresponding profiles flatten out, showing the progression of the spray flow towards an equilibrium state. In the equilibrium state, the liquid-gas mixture is characterized by a mixture density moving at a mixture velocity. This so-called locally homogeneous flow is described by others (Shearer et al. 1979; Desantes et al. 2011). Additional thought on the transition from the state governed by momentum transfer to the equilibrium state is given in section 7.2.

5.8 Summary

The constants of the self-similar model listed in tables 5.1, 5.2 and 5.3 are summarized in table 5.5.

Chapter 6

Predictions

Certain predictions of the model derived in chapter 5 are compared against results reported in the literature. In section 6.1 we discuss the rate of mass entrainment into the sprays. Section 6.2 compares the gas-flow turbulent Reynolds number of the present sprays to the results reported for the single-phase round jet.

6.1 Rate of mass entrainment

The rate of mass entrainment describes the mass of ambient gas entrained into the spray flow. It is of interest in many technical applications, since the entrainment rate relates to the mixing of the liquid and the gas phases. In the present sprays, the definition of the gas mass flow rate, with constant gas density ρ , reads in its general form

$$\dot{m}(z) = 2\pi\rho \int_{r=0}^{\infty} u(r, z)r \, dr. \quad (6.1)$$

Using the self-similar description of the gas flow field, see section 5.2, we obtain

$$\dot{m}(z) = 2\pi\rho C(z - z_0) \int_{\eta=0}^{\infty} f' \, d\eta = 8\pi\rho C(z - z_0). \quad (6.2)$$

The mass flow rate depends on the gas density ρ , the constant C and the axial distance from the virtual origin only. It increases linearly with $z - z_0$. The linear increase emerges from the mathematical structure of the equation and the ansatz for self-similarity (5.15). The exponent α does not appear in (6.2), indicating that the linear trend is universal for boundary-layer type flow described by equation (5.16).

The axial evolution of the entrained mass is usually represented in the form of a nondimensional entrainment rate, which is the ratio of the entrained mass flow rate, $\dot{m} - \dot{m}_{or}$, to initial mass flow rate \dot{m}_{or} . According to Medrano et al. (2017), who considered

two-phase jets with the phases in dynamic equilibrium, it is defined as

$$\dot{m}^+(z) = \frac{\dot{m}(z) - \dot{m}_{or}}{\dot{m}_{or}} = K_e \left(\frac{z}{d_{or}} \right) \left(\frac{\rho}{\rho_{or}} \right)^{1/2}, \quad (6.3)$$

where \dot{m}_{or} is the mass flow rate through the nozzle orifice, z the axial distance from the orifice, d_{or} the orifice diameter, ρ_{or} the density of the ejected fluid and ρ the density of the ambient gas. K_e represents the nondimensional entrainment rate coefficient. Ricou and Spalding (1961) measured the entrainment rate coefficient for different combinations of jet gas and ambient gas in the region $25 < z/d_{or} < 400$. They found a constant value of $K_e = 0.32$ for non-reacting isothermal jets. From (6.2) and (6.3) we calculate the entrainment rate coefficients of the present sprays as

$$K_e = 8\pi\rho C \left(\frac{d_{or}}{\dot{m}_{l,exp}} \right) \left(\frac{\rho_l}{\rho} \right)^{1/2}, \quad (6.4)$$

where we replaced the ratio $(\dot{m} - \dot{m}_{or})/\dot{m}_{or}$ by $\dot{m}/\dot{m}_{l,exp}$, since the initial gas flow rate \dot{m}_{or} is zero, and the axial distance from the orifice z with the axial distance from the virtual origin of the self-similar flow field $z - z_0$. The values obtained for K_e are 0.57, 0.61 and 0.95 for sprays 1, 2 and 3, respectively and therefore much larger than the entrainment rate coefficient reported by Ricou and Spalding (1961). This is reasonable since the presence of the droplets results in a more pronounced widening of the spray flow compared to the single-phase round jet. Notably, the values for sprays 1 and 2 are almost identical. This suggests that the entrainment rate coefficient only weakly depends on the Weber number We_l , and is mainly determined by the Ohnesorge number Oh_l of the spray (see table 3.3).

In sprays, the entrainment rate coefficient is not necessarily of constant value, but may also change with the axial distance from the orifice. Its modified definition, according to Cossali et al. (1996), reads

$$\hat{K}_e(z) = \frac{d\dot{m}}{dz} \left(\frac{d_{or}}{\dot{m}_{or}} \right) \left(\frac{\rho_{or}}{\rho} \right)^{1/2}. \quad (6.5)$$

In the present sprays, however, the entrainment rate \hat{K}_e reduces to the result given in (6.4) since $\dot{m} \propto (z - z_0)$. In other type of sprays, however, entrainment rate coefficients depending on the axial distance from the orifice were reported. Ruff et al. (1989) found \hat{K}_e to be axially increasing for pressure atomization of water jets. They measured entrainment rates in sprays generated with two different nozzles of 9.5 mm and 19.1 mm in diameter. The reported entrainment rate coefficients were of much lower value as in the present sprays, and also lower than the value reported by Ricou and Spalding (1961)

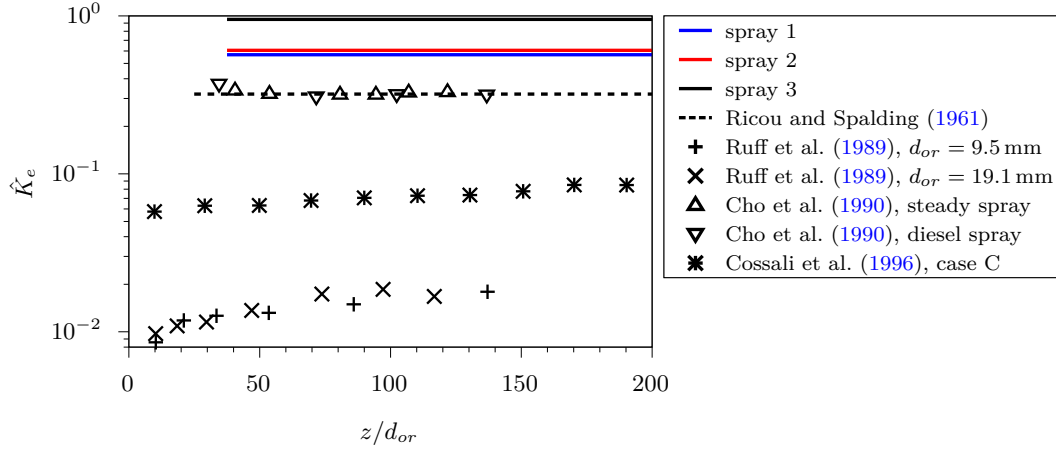


Figure 6.1: Entrainment rate coefficient of the three sprays investigated (solid lines) compared to results reported in the literature (symbols). The dashed line indicates the constant entrainment rate coefficient in the far-field of turbulent single-phase round jets. From the work of Cossali et al. (1996), the case C is depicted where the condition of the ambient atmosphere is closest to our experiments.

for the single-phase round jet, but increasing with its axial position. The difference in scaling and magnitude of \hat{K}_e to the sprays of the present work can be attributed to the different types of sprays investigated. Ruff et al. (1989) atomized liquid jets resulting in very slim and dense sprays. Cho et al. (1990) reported a constant entrainment coefficient $\hat{K}_e = 0.32$ for a steady water spray with an elliptical nozzle cross section ($3 \text{ mm} \times 4 \text{ mm}$) and a diesel spray, originating from a circular nozzle of 0.29 mm in diameter, injected into a high pressure environment. Cossali et al. (1996), on the other hand, reported an axial increase of the entrainment rate coefficient in unsteady full-cone sprays. In contrast to the linear scaling of the entrained gas mass in the present sprays, their results showed an axial scaling of $\dot{m} \propto (z - z_0)^{3/2}$. This difference may be attributed to the different interaction between the liquid and the gas phases in their unsteady full-cone sprays, as compared to the sprays investigated the present study. Figure 6.1 depicts the entrainment rate coefficients \hat{K}_e of sprays 1, 2 and 3, as well as the ones of the studies discussed above. The values of \hat{K}_e in the present sprays are evidently much larger than the results selected from the literature. This is due to the different types of spray flows.

6.2 Gas-flow turbulent Reynolds number

The Reynolds number relates inertial forces to viscous forces. In self-similar turbulent free shear flow, the gas-phase turbulent Reynolds number is usually defined as the ratio of the product of a characteristic velocity scale times a characteristic length scale to the

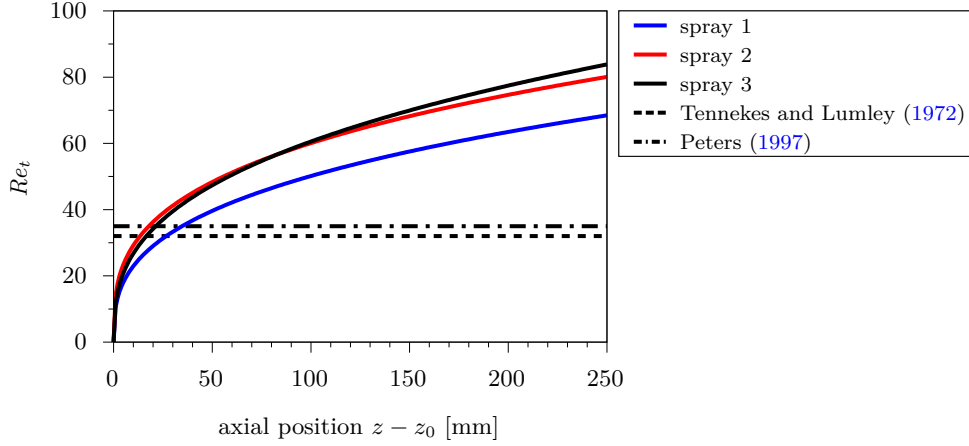


Figure 6.2: Axial evolution of the gas-phase Reynolds number (6.7) in the three sprays. The data of Tennekes and Lumley (1972) and Peters (1997) corresponds to turbulent single-phase round jets.

turbulent eddy viscosity (Pope 2000). For the single-phase round jet it is defined as

$$Re_t = \frac{u_0(z) \ell_{0.5}(z)}{\nu_t} \quad (6.6)$$

with $\ell_{0.5}(z)$ representing the half-width of the jet, i.e. the radial distance of the 50% point of the axial velocity profile from the jet axis (Tennekes and Lumley 1972). Tennekes and Lumley (1972) reported a constant turbulent Reynolds number throughout the flow field in single-phase round jets of $Re_t = 32$, and Peters (1997) reported a similar value of $Re_t = 35$. In the single-phase round jet $\ell_{0.5}(z) \propto (z - z_0)$ and the velocity at the jet axis scales $u_0(z) \propto (z - z_0)^{-1}$. From the value of the constant Reynolds number (6.6), the constant turbulent eddy viscosity can be calculated. In the present two-phase spray flow, the turbulent Reynolds number of the gas flow reads

$$Re_t = \frac{u_0(z) \ell(z)}{\nu_t} = 4 \left(\sqrt{2} - 1 \right)^{1/2} \frac{CD}{\nu_t} (z - z_0)^{1-\alpha}, \quad (6.7)$$

where the half-width of the axial velocity profile is calculated from

$$\frac{u}{u_0} = \frac{1}{(1 + \eta^2/4)^2} := \frac{1}{2} \quad (6.8)$$

as

$$\ell(z) = 2 \left(\sqrt{2} - 1 \right)^{1/2} \frac{(z - z_0)^\alpha}{D}. \quad (6.9)$$

With $\alpha \approx 2/3$ in the present sprays, equation (6.7) suggests that the gas-phase Reynolds number is not of constant value as in the single-phase round jet, but increases with the axial distance from the virtual origin. In light of the increasing momentum flow rate of the gas phase, this finding is plausible. Figure 6.2 compares the gas-phase Reynolds numbers of the three sprays with the constant Reynolds numbers obtained in the single-phase round jet by Tennekes and Lumley (1972) and by Peters (1997). The values of the constant prefactor $4(\sqrt{2} - 1)^{1/2}CD/\nu_t$ in the definition of the Reynolds number (6.7), are different in all three sprays (spray 1: $109.6 \text{ m}^\alpha \text{ s}^{-1}$, spray 2: $123.7 \text{ m}^\alpha \text{ s}^{-1}$, spray 3: $137.1 \text{ m}^\alpha \text{ s}^{-1}$). Its value is smallest in spray 1 and largest in spray 3. From this it follows that the turbulent gas-flow Reynolds number increases with the Weber number We_l and the Ohnesorge number Oh_l (see table 3.3).

Chapter 7

Implications

The self-similar model developed in chapter 5 allows for a convenient description of the gas phase in non-evaporating two-phase axisymmetric spray flow. In the following, we will extend this analysis to heat and mass transport, and discuss other possible applications in two-phase flow fields, which may be the subject of future scientific efforts.

7.1 Heat and mass transport

The self-similar analysis of the gas flow field is extended to describe heat and mass transport in evaporating sprays. Both problems, the transport of heat and mass, are subject to similar equations, but with different characteristic numbers. Thus, we will describe mass transport only and define the corresponding variables in the case of heat transport. The cylindrical axisymmetric equation for the transport of the mass concentration ϱ_j of the vapor component j , obtained from boundary-layer theory, reads

$$u \frac{\partial \varrho_j}{\partial z} + v \frac{\partial \varrho_j}{\partial r} = \mathcal{D}_t \frac{1}{r} \frac{\partial}{\partial r} \left(r \frac{\partial \varrho_j}{\partial r} \right) + S_j. \quad (7.1)$$

Similar to the self-similar analysis of the gas flow field in chapter 5, the turbulent effective diffusion coefficient \mathcal{D}_t is assumed to be of constant value throughout the flow field and much larger than the contribution of molecular diffusion. S_j represents a source term of vapor mass, accounting for the evaporation of the liquid component j . u and v are the velocity components of the self-similar gas flow field, (5.17) and (5.18). To facilitate a self-similar description, the present analysis neglects the influence of the evaporating component both on the velocity field and on the physical properties of the gas flow field, i.e. ρ , μ and σ . As a consequence, it may be applicable to weakly evaporating sprays with low vapor concentrations only. The mass transport equation (7.1) is applicable to heat transport as well. For this purpose, the following quantities need to be replaced

$$\varrho_j \rightarrow T, \quad \mathcal{D}_t \rightarrow a_t \quad \text{and} \quad S_j \rightarrow S_h. \quad (7.2)$$

T denotes the local temperature of the gas flow field, a_t the effective thermal diffusivity and S_h the heat source term.

To transform the transport equation (7.1) into the self-similar coordinate, we choose the following ansatz for the self-similar vapor concentration field

$$\varrho_j(r, z) - \varrho_{j,\infty} = t(z)\Theta(\eta), \quad (7.3)$$

where $t(z)$ is a scaling function, $\Theta(\eta)$ represents the self-similar vapor concentration profile and η is the same coordinate as in the dynamic analysis. $\varrho_{j,\infty}$ denotes the ambient concentration of the vapor component ϱ_j in the undisturbed far field of the spray. For the transport of heat, $\varrho_{j,\infty}$ is replaced by the temperature in the far field T_∞ . Introducing the ansatz (7.3) and the velocity components (5.17) and (5.18) into the mass transport equation (7.1) yields

$$h \frac{t'}{t} f' \Theta - h' f \Theta' = \mathcal{D}_t (\eta \Theta)' + \frac{\eta}{g^2 t} S_j. \quad (7.4)$$

The functions $h(z)$ and $t(z)$, as well as the source term S_j , must allow equation (7.4) to become an ordinary differential equation for $\Theta(\eta)$. With $h' = C$ (see equations (5.9) and (5.14)), we require

$$h \frac{t'}{t} = \text{constant} := \tilde{E} \quad (7.5)$$

resulting in

$$t(z) = F(z - z_0)^{\tilde{E}/C} \quad (7.6)$$

with the two unknown constants \tilde{E} and F . Moreover, we require the vapor source to be of the form

$$S_j(r, z) = \mathcal{D}_t g(z)^2 t(z) \Phi_j(\eta) \quad (7.7)$$

for equation (7.4) to be independent of z . $\Phi_j(\eta)$ denotes a yet unknown self-similar shape function of the vapor source. Introducing the constant

$$\beta := \frac{\tilde{E}}{C}, \quad (7.8)$$

the self-similar ansatz for the concentration field (7.3) and the vapor source (7.7) turn into

$$\varrho_j(r, z) - \varrho_{j,\infty} = F(z - z_0)^\beta \Theta(\eta) \quad \text{and} \quad (7.9)$$

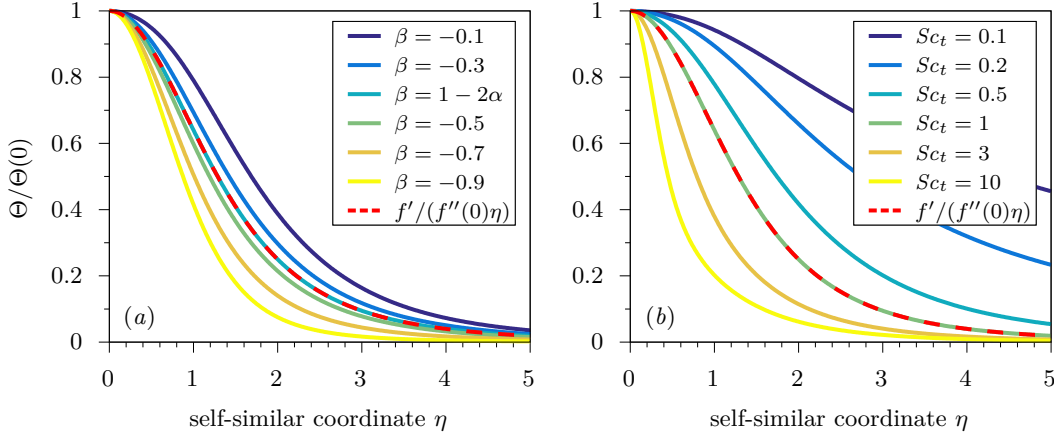


Figure 7.1: Self-similar shape function of the vapor concentration profile calculated from equation (7.12) for (a) $Sc_t = 1$ and different values of the exponent β , and (b) for $\beta = 1 - 2\alpha$ and a range of different turbulent Schmidt numbers Sc_t . For the computation of $\Theta(\eta)$, the self-similar shape function of the vapor source term $\Phi_j(\eta)$ is assumed to be equal to the self-similar shape function of the momentum source term (5.38). The parameters of spray 2 are used. The dashed red line represents the self-similar axial velocity profile of the gas phase.

$$S_j(r, z) = \mathcal{D}_t D^2 F (z - z_0)^{\beta - 2\alpha} \Phi_j(\eta), \quad (7.10)$$

respectively. Here, the exponent β determines the axial dependency of the vapor concentration. F is a constant required for dimensional reasons with the physical unit $\text{kg}/\text{m}^{3+\beta}$. In the case of heat transport, the physical unit of the constant F is K/m^β . Introducing the turbulent Schmidt number

$$Sc_t = \frac{\nu_t}{\mathcal{D}_t}, \quad (7.11)$$

which relates the coefficients of turbulent momentum and turbulent diffusive mass transport, the self-similar transform of the mass transport equation (7.4) reads

$$Sc_t \frac{C}{\nu_t} (\beta f' \Theta - f \Theta') = (\eta \Theta')' + \eta \Phi_j. \quad (7.12)$$

For $\beta = -1$ and $\Phi_j = 0$, (7.12) reduces to the equation of the single-phase round jet (Tropea et al. 2007). To describe heat transport, the turbulent Schmidt number Sc_t is replaced by the turbulent Prandtl number Pr_t . Two boundary conditions are required to determine the solution of (7.12). They are given by

$$\left. \frac{\partial \Theta_j}{\partial \eta} \right|_{\eta \rightarrow 0} = 0 \quad \Rightarrow \quad \Theta'(0) = 0, \quad (7.13)$$

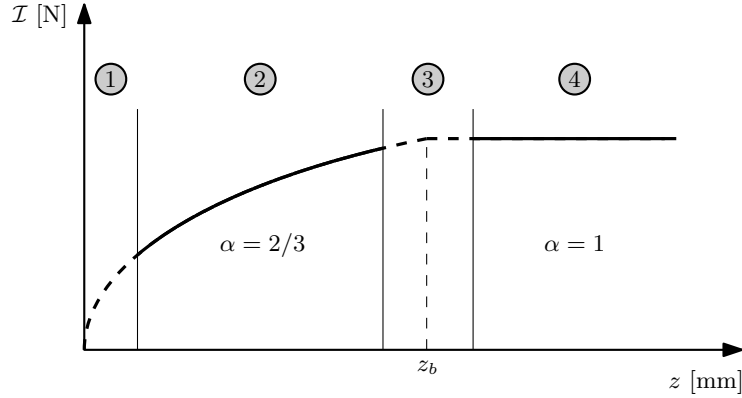


Figure 7.2: Schematic sketch of the axial evolution of the gas-phase momentum flow rate.

$$\varrho_j|_{\eta \rightarrow \infty} = \varrho_{j,\infty} \quad \Rightarrow \quad \Theta(\eta \rightarrow \infty) = 0. \quad (7.14)$$

The first one considers the symmetry of the vapor concentration field. The second one refers to the ambient vapor concentration in the far field.

To solve equation (7.12) for $\Theta(\eta)$ and determine the concentration field (7.9), the constants β , F and Sc_t , as well as the shape function of the self-similar vapor source term $\Phi_j(\eta)$, are required. For the turbulent Schmidt number, Tominaga and Stathopoulos (2007) suggest a value of $Sc_t = 0.9$ in turbulent free shear flow. The determination of the remaining parameters, the exponent β , the constant F , and the self-similar shape function of the vapor source $\Phi_j(\eta)$, is not feasible with the experimental PDA data at hand and therefore beyond the scope of this work. Measurement of the concentration fields in such sprays, as investigated in the present study, is required to derive these model parameters.

The exponent β relates to the global mass flow rate of the vapor component j per

$$\mathcal{M}_j(z) = 2\pi \int_{r=0}^{\infty} u(\varrho_j - \varrho_{j,\infty})r \, dr = 2\pi CF(z - z_0)^{1+\beta} \int_{\eta=0}^{\infty} f'\Theta \, d\eta. \quad (7.15)$$

Due to the evaporation of the liquid component j , with the density $\rho_{l,j}$, we expect the vapor mass flow rate \mathcal{M}_j to increase with the axial distance from the orifice. Thus, the lower limit for the exponent β is given in equation (7.15) by $\beta > -1$. In the case of heat transport, the global enthalpy balance has to be considered

$$\mathcal{H}(z) = 2\pi\rho c_p \int_{r=0}^{\infty} u(T - T_\infty)r \, dr, \quad (7.16)$$

where c_p denotes the specific isobaric heat capacity of the gas.

As an example, we numerically calculate the self-similar concentration profile from (7.12) by means of a shooting method. For this purpose, we assume similarity between mass and momentum transfer, i.e. $\Phi_j(\eta) := \Omega(\eta)$. Figure 7.1, depicts the solutions for various values of (a) β and (b) Sc_t in spray 2. As expected, larger Schmidt numbers result in more slender profiles of $\Theta(\eta)$. A stronger axial decrease in the momentum source term, i.e. smaller values of β , also results in more slender self-similar concentration profiles. For total analogy between mass and momentum transport ($Sc_t = 1$ and $\beta = 1 - 2\alpha$), the self-similar concentration profile collapses with the self-similar axial velocity profile. The latter is depicted as the dashed red lines in figure 7.1.

7.2 Transition to equilibrium

The self-similar model of the gas flow field developed in chapter 5 covers the region of large slip velocities between the phases, i.e. the region where momentum is transferred from the liquid to the gas phase. After the droplets transferred their excess momentum to the gas phase, both phases are in an equilibrium state. In the far field, the spray flow propagates similar to a single-phase jet, but with a variable mixture density due to the presence of the droplets. In this so-called locally homogeneous flow (LHF), the two-phase mixture propagates at a mixture velocity (Faeth 1983; Desantes et al. 2011). Figure 7.2 schematically depicts the axial evolution of the momentum flow rate of the gas phase in the present sprays. The initial entry region ① is succeeded by a region of self-similar liquid-gas momentum transfer ② as reported in the present work (see chapter 5). In the far field ④, the spray flow behaves similar to a single-phase jet flow. Little is known about the transition from the regime of self-similar momentum transfer to the regime of self-similar momentum conservation (region ③). In the following, we propose a simple model to transfer the scaling variables of self-similar liquid-gas momentum transfer ② to self-similar constant momentum flow rate regime ④.

The gas-flow field in both regimes is in general described by the same self-similar equation (5.16), with $\Omega(\eta) = 0$ in the regime ④, and which is in both cases satisfied by the same solution (5.32) for the self-similar shape function. We base our analysis on two assumptions. First, the transition occurs at a discrete axial location z_b , i.e., at $z = z_b$ the exponent switches from $\alpha = 2/3$ to $\alpha = 1$. This implies a kink in the axial evolution of the momentum flow rate of the gas at this point, where it is therefore not continuously differentiable with respect to the z coordinate. Second, for simplicity, we assume that the density of the two-phase mixture in the far field regime ④ is equal to the density of the gas phase, neglecting the presence of the liquid drops. In the following, we denote parameters corresponding to the regimes of liquid-gas momentum transfer and constant momentum flow rate with the subscripts 2 and 4, respectively.

In the cross section of transition between the two regimes, at z_b , the gas momentum flow rate is conserved. From its definition (5.25) we obtain, with $\alpha_4 = 1$, the relation

$$C_2^2 D_2^2 (z_b - z_{0,2})^{2-2\alpha_2} = C_4^2 D_4^2, \quad (7.17)$$

implying that the velocity profiles $u_2(\eta, z_b)$ and $u_4(\eta, z_b)$ are equal as well. Moreover we demand at z_b that $\eta_2 = \eta_4$ and $r_2 = r_4$, respectively, yielding the relation

$$\frac{D_2}{(z_b - z_{0,2})^{\alpha_2}} = \frac{D_4}{(z_b - z_{0,4})} \quad (7.18)$$

from the definition (5.15) of the self-similar coordinate η . The velocity profiles and the lines of constant self-similar coordinates are assumed to be continuously differentiable at z_b , i.e.

$$\left. \frac{\partial u_2}{\partial z} \right|_{z \rightarrow z_b} = \left. \frac{\partial u_4}{\partial z} \right|_{z \rightarrow z_b} \quad \text{and} \quad (7.19)$$

$$\left. \frac{\partial \eta_2}{\partial z} \right|_{z \rightarrow z_b} = \left. \frac{\partial \eta_4}{\partial z} \right|_{z \rightarrow z_b}. \quad (7.20)$$

Using the definitions of the self-similar coordinate η and the axial gas velocity u , (5.15) and (5.17), the constraints (7.19) and (7.20) result in the requirements

$$(1 - 2\alpha)C_2 D_2^2 (z_b - z_{0,2})^{-2\alpha_2} = -C_4 D_4^2 (z_b - z_{0,4})^{-2} \quad \text{and} \quad (7.21)$$

$$\frac{\alpha D_2}{(z_b - z_{0,2})^{1+\alpha_2}} = \frac{D_4}{(z_b - z_{0,4})^2}, \quad (7.22)$$

respectively. Equations (7.17), (7.18), (7.21) and (7.22) represent four constraints for the parameters C_4 , D_4 and $z_{0,4}$. Since this system of equations is overdetermined, only either the continuity of the velocity profiles (7.21) or the continuity of the lines of constant self-similar coordinates (7.22) can be ensured. This is due to the earlier assumption of a sudden transition between the two regimes at z_b , resulting in the kink in the axial evolution of the momentum flow rate. In the following, the results corresponding to (7.21) are labeled with subscript I and the results for (7.22) are labeled with subscript II.

From (7.17), (7.18) and (7.21), left column, and from (7.17), (7.18) and (7.22), right column, we obtain the expressions

$$z_{0,4\text{-I}} = z_b - \frac{z_b - z_{0,2}}{2\alpha_2 - 1} \quad z_{0,4\text{-II}} = z_b - \frac{z_b - z_{0,2}}{\alpha_2} \quad (7.23)$$

$$C_{4\text{-I}} = (2\alpha_2 - 1)C_2 \quad C_{4\text{-II}} = \alpha_2 C_2 \quad (7.24)$$

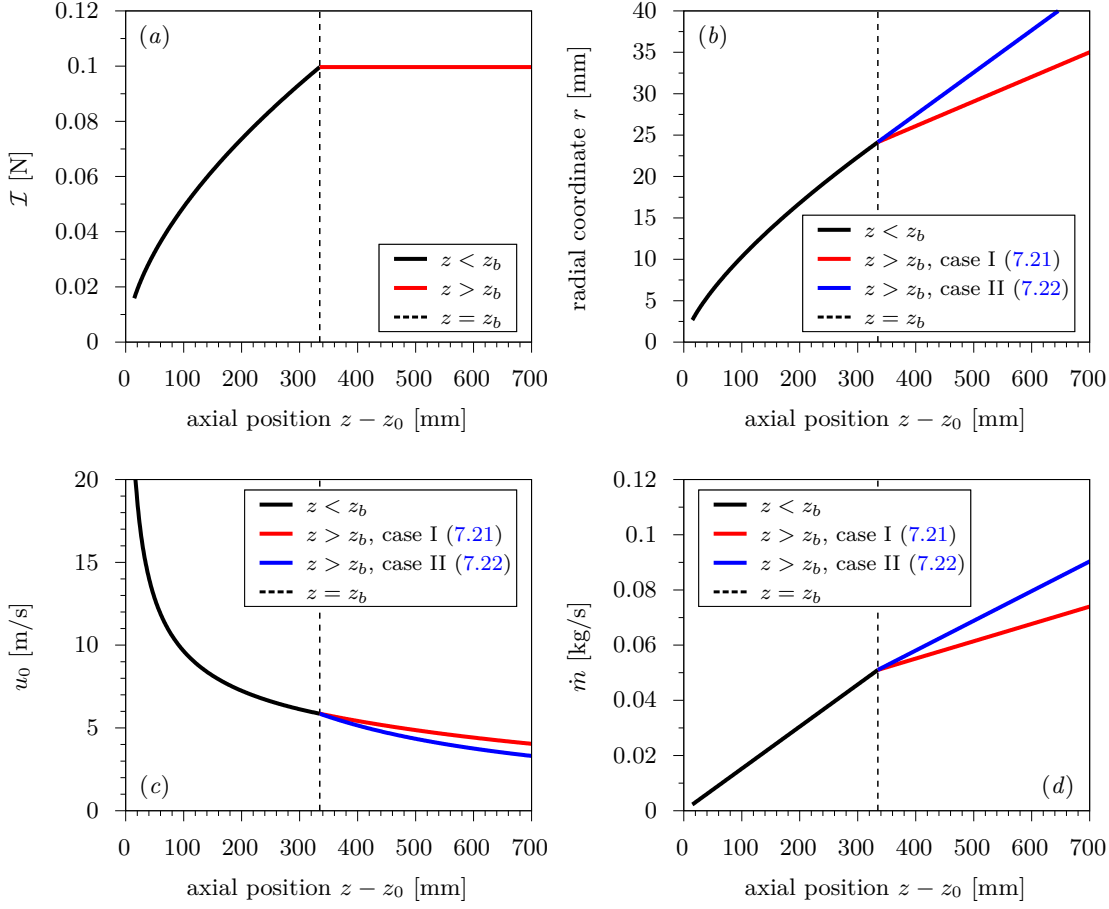


Figure 7.3: Transition from the regime of momentum transfer to jet-like momentum conservation. (a) Momentum flow rate, (b) lines of the self-similar coordinate $\eta = 1$, (c) axial gas velocity at the spray axis and (d) gas mass flow rate. The assumed cross section of transition is indicated by the dashed vertical line at z_b . The data corresponds to spray 2.

$$D_{4-I} = D_2 \frac{(z_b - z_{0,2})^{1-\alpha_2}}{2\alpha_2 - 1} \quad D_{4-II} = D_2 \frac{(z_b - z_{0,2})^{1-\alpha_2}}{\alpha_2} \quad (7.25)$$

for the parameters C_4 , D_4 and $z_{0,4}$. Note that the virtual origin $z_{0,4}$ is not located in the vicinity of the orifice ($z = 0$), but rather at large negative distances of z .

As an example, figure 7.3 depicts the transition to the equilibrium state in spray 2 using the constants given in (7.23) to (7.25). We assume the axial position of transition to be at $z_b = 320$ mm ($z/d_{or} = 800$). This value is purely hypothetical and chosen for illustration purposes only. In practice, the axial position z_b is determined by the limiting criterion (5.60), which sets the limit to the regime with liquid-gas momentum transfer. In figure 7.3(a) the evolution of the momentum flow rate with a kink at z_b is depicted.

Figure 7.3(b) shows lines $\eta = \text{constant}$ in the (r, z) space. In case I (7.21), a kink in the line can be observed at z_b , whereas the profile is smooth in case II (7.22). Figure 7.3(c) shows the decrease of the gas velocity at the spray axis $u_0(z)$. For case I (7.21), a smooth transition between the regimes can be observed. The evolution of the gas mass flow rate is depicted in figure 7.3(d). It exhibits a change in the entrainment rate in both cases, as indicated by the different slopes before and after z_b . The axial scaling is linear in both regimes.

In real spray flows, the scaling variables describing the spray propagation in the far field may be in between the results corresponding to the two different cases reported in (7.23) to (7.25). Experimental data is required to reveal the details of the transition from regime ② to regime ④, i.e. regime ③ (see figure 7.2). This may be an interesting subject for future studies.

7.3 Self-similarity of the liquid phase

The present analysis revealed self-similarity of the z -momentum equation of the liquid phase (5.4), by showing that both terms on its left-hand side are self-similar in the sprays investigated (see section 5.6). From this finding followed the self-similarity of the momentum source f_d . In the present section, we present further evidence for the self-similar behavior of the liquid phase. We take the profiles of the liquid mass concentration, c_l , see figures 4.6(b,d,f), scale them with the concentration at the spray axis, $c_{l,0}$, and plot them against the self-similar coordinate η . The resulting profiles are shown in figure 7.4. They collapse quite well on a single curve in each spray, with some deviations in spray 2 for the profile closest to the orifice. This indicates that not only the liquid momentum equation behaves self-similar, but also the concentration of the liquid mass.

This finding raises the question if there exist self-similar mean velocity profiles of the liquid phase as well, and if they can be described mathematically. In fact, Yeung (1982) suggested a similarity solution for axisymmetric spray flow. Instead of considering the liquid as an ensemble of discrete droplets for the equations of motions, as in the present study, see (5.3) and (5.4), he treated the liquid phase as a continuum

$$\frac{\partial}{\partial z} (c_l \check{u}_l) + \frac{1}{r} \frac{\partial}{\partial r} (r c_l \check{v}_l) = 0 \quad \text{continuity liquid} \quad (7.26)$$

$$\frac{\partial}{\partial z} (c_l \check{u}_l^2) + \frac{1}{r} \frac{\partial}{\partial r} (r c_l \check{u}_l \check{v}_l) = -\rho f_{d,z} \quad z\text{-momentum liquid} \quad (7.27)$$

$$\frac{\partial}{\partial z} (c_l \check{u}_l \check{v}_l) + \frac{1}{r} \frac{\partial}{\partial r} (r c_l \check{v}_l^2) = -\rho f_{d,r} \quad r\text{-momentum liquid} \quad (7.28)$$

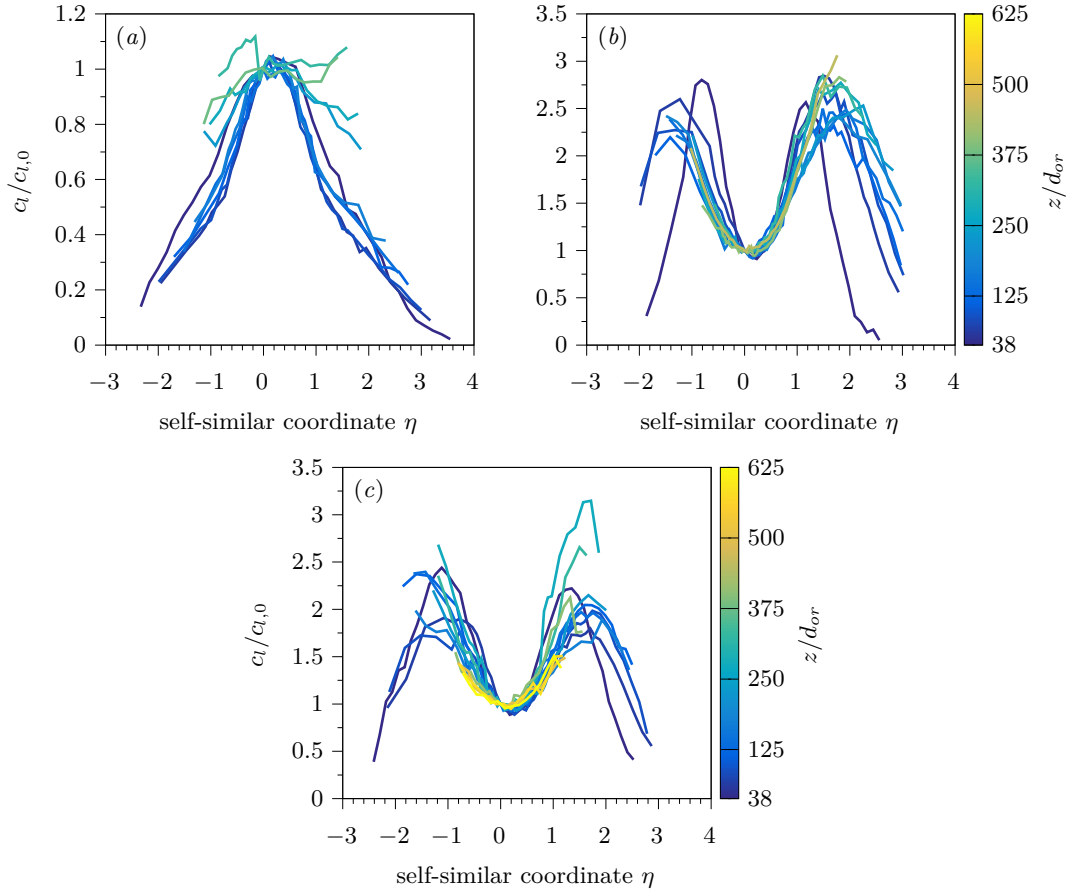


Figure 7.4: Self-similar profiles of the concentration of liquid mass. The liquid mass concentration at the spray axis is denoted by $c_{l,0}$. (a) Spray 1, (b) spray 2 and (c) spray 3.

Here, \check{u}_l and \check{v}_l denote the mean velocities in axial and radial directions of the liquid phase, respectively. Yeung (1982) coupled these equations of motion of the continuous liquid phase to the equations of motion of the gas phase. The latter are defined similar to (5.1) and (5.2).

There are certainly many open questions to this approach. For example, the coupling of the liquid and gas phases through the source terms $f_{d,z}$ and $f_{d,r}$ is not straightforward, since the drag force is drop-size and drop-velocity dependent. Moreover, the momentum equation of the gas phase in radial direction is neglected due to the boundary-layer approach. But it has to be considered in the description of the liquid phase in order to obtain three equations for the determination of three unknown quantities (c_l , \check{u}_l and \check{v}_l). Despite these open questions, however, this topic may be interesting for future scientific investigations, since our measurement data clearly show the self-similarity of c_l (see figure 7.4).

7.4 Self-similar planar flows

The self-similar analysis of a boundary-layer type flow including a momentum source term, as documented in chapter 5, may be applicable to spray flows produced by other types of atomizers as well. The self-similar shape function of the momentum source (5.38) covers a range of different shapes (see figure 5.12). In theory, other combinations of $f(\eta)$ and $\Omega(\eta)$ satisfying the self-similar momentum equation (5.16) are possible. Experimental data at hand is required to carry out the analysis. In the present section, we derive the governing equation for a possibly self-similar flow field of plane sprays, for example produced by flat fan nozzles. This type of flow is well-known for its self-similar behavior in the single-phase case. In contrast to the single-phase round jet, in the single-phase plane jet, the governing equations and the resulting axial scaling functions differ between the laminar and the turbulent case. Thus, we will first investigate the simpler laminar case with a constant dynamic viscosity, and then examine the turbulent case, where the turbulent eddy viscosity may scale with the axial distance from the orifice.

7.4.1 Plane laminar two-phase flow

In plane sprays, the governing equations of the gas flow field are described in Cartesian coordinates. The equations of motion are of laminar boundary-layer type with constant pressure throughout and read

$$\frac{\partial u_q}{\partial x} + \frac{\partial v_q}{\partial y} = 0 \quad \text{continuity gas} \quad (7.29)$$

$$u_q \frac{\partial u_q}{\partial x} + v_q \frac{\partial u_q}{\partial y} = \nu_q \frac{\partial^2 u_q}{\partial y^2} + f_{d,q} \quad x\text{-momentum gas} \quad (7.30)$$

where x and u_q are the coordinate and the velocity component in streamwise direction, and y and v_q denote the coordinate and the velocity component in normal direction. $f_{d,q}$ denotes the momentum source term and ν_q the constant molecular kinematic gas viscosity. In the following, all variables corresponding to the laminar plane flow are denoted by the subscript q . We introduce the Stokesian stream function Ψ_q , which is defined through the downstream and transverse velocity components

$$u_q = \frac{\partial \Psi_q}{\partial y} \quad \text{and} \quad v_q = -\frac{\partial \Psi_q}{\partial x}, \quad (7.31)$$

respectively. The x -momentum equation (7.30) reads in terms of the stream function as follows

$$\frac{\partial \Psi_q}{\partial y} \frac{\partial \Psi_q}{\partial x \partial y} - \frac{\partial \Psi_q}{\partial x} \frac{\partial^2 \Psi_q}{\partial y^2} = \nu \frac{\partial^3 \Psi_q}{\partial y^3} + f_{d,q}. \quad (7.32)$$

We introduce the ansatz for the self-similar coordinate and the stream function

$$\eta_q = g_q(x) y \quad \text{and} \quad \Psi_q = h_q(x) f_q(\eta_q), \quad (7.33)$$

the latter depending on the self-similar shape function $f_q(\eta_q)$. $g_q(x)$ is a scaling function and $h_q(x)$ is a mapping function. Introduction of (7.33) into (7.32) yields

$$\left(\frac{h'_q}{\nu_q g_q} + \frac{g'_q h_q}{\nu_q g_q^2} \right) f_q'^2 - \frac{h'_q}{\nu_q g_q} f_q f_q'' = f_q''' + \frac{1}{\nu_q g_q^3 h_q} f_{d,q}. \quad (7.34)$$

For (7.34) to be an ordinary differential equation for the self-similar shape function $f_q(\eta_q)$ only, we require

$$\frac{h'_q}{\nu_q g_q} = \text{constant} =: \tilde{A}_q, \quad (7.35)$$

$$\frac{h'_q}{\nu_q g_q} + \frac{g'_q h_q}{\nu_q g_q^2} = \text{constant} =: \tilde{C}_q, \quad (7.36)$$

so that the functions $h_q(x)$ and $g_q(x)$ read

$$h_q(x) = \tilde{D}_q \left[\left(1 - \nu_q^2 \tilde{A}_q (\tilde{C}_q - \tilde{A}_q) \right) x + \tilde{B}_q \right]^{-[1 - \nu_q^2 \tilde{A}_q (\tilde{C}_q - \tilde{A}_q)]} \quad (7.37)$$

$$g_q(x) = \frac{\tilde{D}_q}{\nu_q \tilde{A}_q} \left[1 - \nu_q^2 \tilde{A}_q (\tilde{C}_q - \tilde{A}_q) \right] \left[\left(1 - \nu_q^2 \tilde{A}_q (\tilde{C}_q - \tilde{A}_q) \right) x + \tilde{B}_q \right]^{-[1 - \nu_q^2 \tilde{A}_q (\tilde{C}_q - \tilde{A}_q)] - 1}. \quad (7.38)$$

The constants \tilde{A}_q , \tilde{B}_q , \tilde{C}_q and \tilde{D}_q are replaced by

$$\alpha_q := - \left[1 - \nu_q^2 \tilde{A}_q (\tilde{C} - \tilde{A}_q) \right], \quad (7.39)$$

$$x_{0,q} := - \frac{\tilde{B}_q}{1 - \nu_q^2 \tilde{A}_q (\tilde{C}_q - \tilde{A}_q)}, \quad (7.40)$$

$$C_q := \tilde{D}_q \left[1 - \nu_q^2 \tilde{A}_q (\tilde{C}_q - \tilde{A}_q) \right]^{-[1 - \nu_q^2 \tilde{A}_q (\tilde{C}_q - \tilde{A}_q)]}, \quad (7.41)$$

$$D_q := \frac{\tilde{D}_q}{\nu_q \tilde{A}_q} \left[1 - \nu_q^2 \tilde{A}_q (\tilde{C}_q - \tilde{A}_q) \right] \left[1 - \nu_q^2 \tilde{A}_q (\tilde{C}_q - \tilde{A}_q) \right]^{-[1 - \nu_q^2 \tilde{A}_q (\tilde{C}_q - \tilde{A}_q)] - 1}. \quad (7.42)$$

For the momentum source term $f_{d,q}$, we require

$$f_{d,q}(x, y) := \frac{\nu_q C_q}{D_q} g_q(x)^3 h_q(x) \Omega_q(\eta_q), \quad (7.43)$$

where $\Omega_q(\eta_q)$ is a yet unknown self-similar shape function of the momentum source. With the constants (7.39) to (7.42), the ansatz for self-similarity (7.33) and the momentum source term (7.43) become

$$\eta_q = D_q \frac{y}{(x - x_{0,q})^{1-\alpha_q}}, \quad (7.44)$$

$$\Psi_q = C_q (x - x_{0,q})^{\alpha_q} f_q(\eta_q), \quad (7.45)$$

$$f_{d,r} = D_q^4 (x - x_{0,q})^{4\alpha_q - 3}. \quad (7.46)$$

The x -momentum equation transformed into the self-similar coordinate, (7.34), turns into

$$(2\alpha_q - 1)f_q'^2 - \alpha_q f_q f_q'' = \frac{\nu_q D_q}{C_q} f_q''' + \Omega_q(\eta_q). \quad (7.47)$$

The velocity components u_q and v_q become

$$u_q = g_q h_q f_q' = C_q D_q (x - x_{0,q})^{2\alpha_q - 1} f_q' \quad \text{and} \quad (7.48)$$

$$v_q = -h_q' f_q - \frac{g_q' h_q}{g_q} \eta f_q' = C_q (x - x_{0,q})^{\alpha_q - 1} \left[(1 - \alpha_q) \eta f_q' - \alpha_q f_q \right]. \quad (7.49)$$

The value of the exponent α_q depends on the global momentum flow rate. For the plane flow field of the gas phase, the momentum flow rate per unit width B reads

$$\frac{\mathcal{I}_q(x)}{B} = 2\pi\rho_q \int_{y=-\infty}^{\infty} u_q^2(x, y) dy = 2\pi\rho_q C_q^2 D_q (x - x_{0,q})^{3\alpha_q - 1} \int_{\eta_q=-\infty}^{\infty} f_q'^2 d\eta. \quad (7.50)$$

For an increasing momentum flow rate we expect $\alpha_q > 1/3$. In the single-phase plane jet, with a constant momentum flow rate, we obtain $\alpha_q = 1/3$. Together with $\Omega_q(\eta_q) = 0$, equation (7.47) simplifies to the single-phase case (Brenn 2017). Note, in laminar flow the molecular Reynolds number increases with the distance from the orifice, even for single-phase plane jets with a constant momentum flow rate

$$Re_q = \frac{u_{0,q}(x) \ell_q(x)}{\nu_q} \propto h_q(x) \propto (x - x_{0,r})^{\alpha_q}. \quad (7.51)$$

7.4.2 Plane turbulent two-phase flow

Turbulent plane jets differ significantly from their laminar counterparts. Unlike the axisymmetric case, the turbulent eddy viscosity ν_t is not constant throughout the flow field, but scales with the axial distance from the orifice (Schlichting and Gersten 2017). We expect similar behavior in plane self-similar two-phase spray flow. In this section, we present the corresponding analysis.

The equations of motion of the gas phase (7.29) and (7.30) are given in the previous section. In the turbulent case, the constant molecular kinematic viscosity ν_q is replaced with the turbulent eddy viscosity $\nu_{t,s}(x)$, depending on the axial coordinate x . In the following, variables referring to the turbulent plane spray flow are denoted by the subscript s . Introducing the Stokesian stream function Ψ_s , similar to (7.31), the velocity field satisfies the continuity equation (7.29). The ansatz for self-similarity is given by

$$\eta_s = g_s(x) y \quad \text{and} \quad \Psi_s = h_s(x) f_s(\eta_s), \quad (7.52)$$

similar to (7.33). Additionally, we require an ansatz for the non-constant turbulent eddy viscosity $\nu_{t,s}$. In turbulent single-phase plane jets, $\nu_{t,s}$ is independent of η_s and proportional to a length and velocity scale, $\ell \propto 1/g_s(x)$ and $u_0 \propto g_s(x)h_s(x)$, of the flow field, producing in a constant turbulent Reynolds number $Re_{t,s}$ (Schlichting and Gersten 2017). For example, Tennekes and Lumley (1972) reported a constant turbulent Reynolds number of $Re_{t,s} = 25.7$ in turbulent single-phase plane jets. In the axisymmetric two-phase spray flow, however, we have shown an axial increase in the turbulent gas flow Reynolds number (6.7). We expect a similar increase of $Re_{t,s}$ in the turbulent plane spray flow. With the length-scale $1/g_s(x)$ and the velocity scale $g_s(x)h_s(x)$, and the definition of the Reynolds number (6.6), our ansatz for the turbulent eddy viscosity reads

$$\nu_{t,s}(x) = \frac{h_s(x)}{k_s(x)}. \quad (7.53)$$

The scaling function $k_s(x)$ represents the a priori unknown streamwise scaling of the turbulent Reynolds number $Re_{t,s}$ of the gas phase. With (7.52) and (7.53), we transform the x -momentum equation (7.30) into the self-similar coordinate yielding

$$\left(\frac{h'_s k_s}{g_s h_s} + \frac{g'_s k_s}{g_s^2} \right) f_s'^2 - \frac{h'_s k_s}{g_s h_s} f_s f_s'' = f_s''' + \frac{k_s}{g_s^3 h_s^2} f_{d,s}. \quad (7.54)$$

To obtain an ordinary differential equation, independent of x , we require

$$\frac{h'_s k_s}{g_s h_s} = \text{constant}, \quad (7.55)$$

$$\frac{h'_s h_s}{g_s h_s} + \frac{g'_s k_s}{g_s^2} = \text{constant}. \quad (7.56)$$

The momentum source term $f_{d,s}$ must be of the form

$$f_{d,s}(x, y) := \frac{g_s(x)^3 h_s(x)^2}{k_s(x)} \Omega_s(\eta_s), \quad (7.57)$$

where $\Omega_s(\eta_s)$ is the self-similar shape function of the momentum source. The system of equations (7.55) to (7.56), to determine $g_s(x)$, $h_s(x)$ and $k_s(x)$ is, however, under-determined. Thus we follow a different approach, assuming the following power laws

$$g_s(x) = D_s (x - x_{0,s})^{\alpha_s}, \quad (7.58)$$

$$h_s(x) = C_s (x - x_{0,s})^{\beta_s}, \quad (7.59)$$

$$k_s(x) = E_s (x - x_{0,s})^{\gamma_s}, \quad (7.60)$$

as an ansatz for $g_s(x)$, $h_s(x)$ and $k_s(x)$. Consequently, the momentum equation (7.54) turns into

$$(x - x_{0,s})^{\gamma_s - \alpha_s - 1} \left[(\alpha_s + \beta_s) f'^2 - \beta_s f_s f'' \right] = \frac{D_s}{E_s} f_s''' + \frac{D_s}{E_s} \Omega_s(\eta_s), \quad (7.61)$$

where the exponents γ_s and α_s have to be chosen such that the exponent of the x coordinate vanishes. Additional information on the axial scaling of the flow field is obtained from the global momentum flow rate. We assume it to be proportional to a power function with the exponent m_s , i.e. $\mathcal{I}_s(x) \propto (x - x_{0,s})^{m_s}$ with $m_s > 0$. The axial scaling of the momentum flow rate of the gas phase in self-similar coordinates is given by

$$\mathcal{I}(z) \propto (x - x_{0,s})^{m_s} \propto (x - x_{0,s})^{\alpha_s + 2\beta_s}. \quad (7.62)$$

From (7.61) and (7.62) we obtain the following constraints for the exponents

$$\gamma_s - \alpha_s - 1 = 0, \quad (7.63)$$

$$m_s = \alpha_s + 2\beta_s. \quad (7.64)$$

Solved for α_s and β_s they read

$$\alpha_s = \gamma_s - 1, \quad (7.65)$$

$$\beta_s = \frac{1}{2} (m_s - \gamma_s + 1). \quad (7.66)$$

The axial dependency of the turbulent eddy viscosity (7.53) turns into

$$\nu_{t,s}(x) \propto (x - x_{0,s})^{\beta_s - \gamma_s} \propto (x - x_{0,s})^{(m_s - 3\gamma_s + 1)/2}. \quad (7.67)$$

Without liquid-gas momentum transfer, i.e. $\Omega_s(\eta_s) = 0$, $m_s = 0$ and $\gamma_s = 0$, we obtain the exponents $\alpha_s = -1$ and $\beta_s = 1/2$, the axial scaling $\nu_{t,s}(x) \propto (x - x_{0,s})^{1/2}$, and the self-similar momentum equation (7.61) of the turbulent single-phase plane jet (Schlichting and Gersten 2017).

Chapter 8

Summary and conclusions

Sprays generated by a prefilming consumer-type pressure atomizer were investigated in the present study. The analysis is based on phase-Doppler (PDA) measurements at a high spatial resolution in spray cross sections from 38 nozzle diameters up to 625 nozzle diameters downstream from the orifice. This region of the sprays is dominated by large slip velocities between the droplets and the gas phase. To ensure high statistical reliability, each local sample consists of 100,000 droplets. Measurements were conducted in three sprays, generated in atmospheric air. The sprays had different pairs of characteristic Weber and Ohnesorge numbers. The liquid mass flow rates were in the range of commercial consumer sprays. Demineralized water and a dilute aqueous ethanol solution were used as the test liquids. The PDA measurements revealed the effect of different sheet geometries, producing, at low Weber numbers, sprays with the liquid concentrated near the spray axis, i.e. solid-cone sprays, and hollow-cone sprays at high Weber numbers.

The motion of the gas phase in the present sprays was induced by momentum transfer from the droplets exclusively. With the PDA measurement data at hand, we determined the velocity field of the gas phase using the smallest droplets in the local ensemble as tracer particles. A procedure was developed to account for local bimodal velocity spectra, as observed for the smallest droplets. The origin of these bimodal velocity distributions remains to be explained. Our measurement data hint at possible group effects of drops of different sizes interacting with each other, since the effect was only observed in cross sections close to the atomizer where the local drop number concentration is high. We term this phenomenon, which has been reported by others before, the *teaspoon effect*, suggested by the shape of the drop size-velocity correlations. A similar effect has also been observed by others for jets in crossflow.

Based on the experimental results, we derive an analytical model for the self-similar flow field of the gas phase in the sprays, revealing the self-similarity of both the liquid and the gas phases. The self-similar mathematical description of the gas phase is derived from boundary-layer theory, accounting for momentum transfer between the droplets and the gas. Notably, despite the strong momentum transfer from the liquid to the gas phase, the obtained self-similar shape function of the velocity field is similar to the one of the axisymmetric single-phase jet. The scaling variables, however, differ significantly.

In axisymmetric free-shear boundary layer flow, the self-similar variable η is in general defined as $\eta \propto r/z^\alpha$. In the single-phase case α is unity, resulting in straight lines $\eta = \text{constant}$ in the (r, z) space. In the present sprays, α is of approximately constant value, with $\alpha = 2/3$. Thus, lines of $\eta = \text{constant}$ are curved in the (r, z) space, reflecting the axial increase of the gas momentum flow rate $\mathcal{I} \propto z^{2-2\alpha} = z^{2/3}$. As a consequence, the decrease of the axial gas velocity, which is inversely proportional to the axial distance from the orifice for the single-phase jet, turned out to be much slower in the present sprays with $u \propto z^{1-2\alpha} = z^{-1/3}$. This finding seems plausible due to the acceleration of the gas by the droplets.

The momentum source term in the z -momentum equation of the gas phase was modeled by a self-similar shape function. The model is in very good agreement with the loss of momentum of the liquid phase calculated from the PDA measurement data and thereby revealed the self-similar behavior of the liquid phase. Notably, the mathematical description of the momentum source term was able to represent both solid-cone and hollow-cone sprays. Focus was set on the determination of the turbulent eddy viscosity, which represents a model parameter of the self-similar description. As assumed beforehand, and as known from turbulent round jets, the analysis of the experimental data revealed approximately constant values for ν_t throughout the spray flow field. The values obtained for ν_t from the PDA measurement data were in the correct order of magnitude, but slightly too small for the model to represent all aspects of the measurements correctly. An increase of the measured values of ν_t by approximately 50 % yielded perfect agreement between model and experimental data. This increase was justified by demonstrating that the underestimation of ν_t is connected to the underestimation of the gas-phase turbulence intensities using the spray droplets as tracer particles.

The application of the model is limited due to the power-law dependency of the flow field variables on the axial coordinate. Thus, the model is valid in regions of the sprays with momentum transfer from the drops to the gas phase, until the two phases reach a state of dynamic equilibrium. In the equilibrium state, the spray flow can be modeled similar to a single-phase jet, but with variable density due to the non-uniform distribution of the liquid droplets. This has been demonstrated by others.

The results of the present study contribute to the understanding of droplet-driven spray flow. The self-similar analytical model, derived from boundary-layer theory, allows for a convenient description of the gas-phase velocity field. It provides a powerful basis to facilitate and enhance future spray modeling efforts.

Bibliography

- Albrecht, H.-E., Damaschke, N., Borys, M., and Tropea, C. (2003) Laser Doppler and phase Doppler measurement techniques. [Springer](#), Berlin, Heidelberg.
- Amili, O., Edgington-Mitchell, D. M., Honnery, D. R., Duke, D., and Soria, J. (2015) Pressurised metered-dose inhaler spray structure. *Ninth International Symposium on Turbulence and Shear Flow Phenomena*. Melbourne, AUS.
- Ariyapadi, S., Balachandar, R., and Berruti, F. (2003) Spray characteristics of two-phase feed nozzles. *The Canadian Journal of Chemical Engineering* **81**, pp. 923–939.
- Bade, K. M. and Schick, R. J. (2011) Phase Doppler interferometry volume flux sensitivity to parametric setting and droplet trajectory. *Atomization and Sprays* **21**, pp. 537–551.
- Barenblatt, G. I. (1996) Scaling, self-similarity, and intermediate asymptotics: Dimensional analysis and intermediate asymptotics. [Cambridge University Press](#), Cambridge.
- Barnsley, M. F. (1993) Fractals everywhere. [Academic Press](#), San Diego.
- Bayvel, L. P. and Orzechowski, Z. (1993) Liquid atomization. [Taylor & Francis](#), Washington, DC.
- Benajes, J., Salvador, F. J., Carreres, M., and Jaramillo, D. (2016) On the relation between the external structure and the internal characteristics in the near-nozzle field of diesel sprays: *Proceedings of the Institution of Mechanical Engineers, Part D: Journal of Automobile Engineering* **231**, pp. 360–371.
- Blasius, H. (1908) Grenzsichten in Flüssigkeiten mit kleiner Reibung. *Zeitschrift für Mathematik und Physik* **56**, pp. 1–37.
- Boussinesq, J. (1877) Essai sur la théorie des eaux courantes. *Mémoires présentés par divers savants à l'Académie des Sciences* **XXIII**, pp. 1–680.
- Brenn, G. (2017) Analytical solutions for transport processes. [Springer](#), Berlin, Heidelberg.
- Chao, B. T. (1964) Turbulent transport behaviour of small particles in dilute suspension. *Österreichisches Ingenieur-Archiv* **18**, pp. 7–21.
- Chen, Y.-C., Stårner, S. H., and Masri, A. R. (2006) A detailed experimental investigation of well-defined, turbulent evaporating spray jets of acetone. *International Journal of Multiphase Flow* **32**, pp. 389–412.

BIBLIOGRAPHY

- Cho, I. Y., Fujimoto, H., Ha, J. Y., Tanabe, H., and Sato, G. T. (1990) Similarity law of entrainment into diesel spray and steady spray. *SAE Technical Paper* **900447**.
- Copan, J., Balachandar, R., and Berruti, F. (2001) Droplet size-velocity characteristics of sprays generated by two-phase feed nozzles. *Chemical Engineering Communications* **184**, pp. 105–124.
- Cossali, G. E. (2001) An integral model for gas entrainment into full cone sprays. *Journal of Fluid Mechanics* **439**, pp. 353–366.
- Cossali, G. E., Gerla, A., Coghe, A., and Brunello, G. (1996) Effect of gas density and temperature on air entrainment in a transient diesel spray. *SAE Technical Paper* **960862**, pp. 105–115.
- Dafsari, R. A., Vashahi, F., and Lee, J. (2017) Effect of swirl chamber length on the atomization characteristics of a pressure-swirl nozzle. *Atomization and Sprays* **27**, pp. 859–874.
- Dantec Dynamics (2002) *BSA flow software - Installation & user's guide*.
- Desantes, J. M., Arregle, J., Lopez, J. J., and Cronhjort, A. (2006a) Scaling laws for free turbulent gas jets and Diesel-like sprays. *Atomization and Sprays* **16**, pp. 443–474.
- Desantes, J. M., Pastor, J. V., García-Oliver, J. M., and Pastor, J. M. (2009) A 1D model for the description of mixing-controlled reacting diesel sprays. *Combustion and Flame* **156**, pp. 234–249.
- Desantes, J. M., Payri, R., Garcia, J. M., and Salvador, F. J. (2007) A contribution to the understanding of isothermal diesel spray dynamics. *Fuel* **86**, pp. 1093–1101.
- Desantes, J. M., Payri, R., Salvador, F. J., and Gil, A. (2006b) Development and validation of a theoretical model for diesel spray penetration. *Fuel* **85.7**, pp. 910–917.
- Desantes, J. M., Salvador, F. J., López, J. J., and De la Morena, J. (2011) Study of mass and momentum transfer in diesel sprays based on X-ray mass distribution measurements and on a theoretical derivation. *Experiments in Fluids* **50**, pp. 233–246.
- Dhivyaraja, K., Gaddes, D., Freeman, E., Tadigadapa, S., and Panchagnula, M. V. (2019) Dynamical similarity and universality of drop size and velocity spectra in sprays. *Journal of Fluid Mechanics* **860**, pp. 510–543.
- Djenidi, L., Antonia, R. A., Lefeuvre, N., and Lemay, J. (2016) Complete self-preservation on the axis of a turbulent round jet. *Journal of Fluid Mechanics* **790**, pp. 57–70.
- Durst, F., Melling, A., and Whitelaw, J. H. (1987) *Theorie und Praxis der Laser-Doppler-Anemometrie*. Braun-Verlag, Karlsruhe.
- Durst, F. and Zaré, M. (1975) Laser Doppler measurements in two-phase flows. *Proceedings of the LDA-Symposium*. Copenhagen, DK.

- Faeth, G. M. (1983) Evaporation and combustion of sprays. *Progress in Energy and Combustion Science* **9**, pp. 1–76.
- Feldmann, O. and Mayinger, F., eds. (2001) *Optical Measurements: Techniques and Applications*. Springer-Verlag, Berlin, Heidelberg.
- Felton, P. G., Chehroudi, B., Bracco, F. V., and Onuma, Y. (1988) LDV measurements of axial drop velocity in evaporating, dense sprays. *Journal of Propulsion and Power* **4**, pp. 399–405.
- Fraser, R. P. and Eisenklam, P. (1953) Research into the performance of atomizers for liquids. *Journal of the Imperial College Chemical Engineering Society* **7**, pp. 52–68.
- Friehe, C. A., Van Atta, C. W., and Gibson, C. H. (1971) Jet turbulence: dissipation rate measurements and correlations. *AGARD Turbulent Shear Flows CP-93*, pp. 18-1–18-7.
- García-Oliver, J. M., Malbec, L.-M., Toda, H. B., and Bruneaux, G. (2017) A study on the interaction between local flow and flame structure for mixing-controlled Diesel sprays. *Combustion and Flame* **179**, pp. 157–171.
- George, W. K. (1989) The self-preservation of turbulent flows and its relation to initial conditions and coherent structures. *Advances in turbulence* (ed. by George, W. K. and Arndt, R.), pp. 39–73. Hemisphere, New York.
- Ghosh, S. and Hunt, J. C. R. (1994) Induced air velocity within droplet driven sprays. *Proceedings of the Royal Society of London. Series A. Mathematical and Physical Sciences* **444**, pp. 105–127.
- Ghosh, S., Phillips, J. C., and Perkins, R. J. (1991) Modelling the flow in droplet-driven sprays. *Advances in Turbulence 3* (ed. by Johansson, A. V. and Alfredsson, P. H.), pp. 405–413. Springer, Berlin, Heidelberg.
- Gounder, J. D., Kourmatzis, A., and Masri, A. R. (2012) Turbulent piloted dilute spray flames: Flow fields and droplet dynamics. *Combustion and Flame* **159**, pp. 3372–3397.
- Hinterbichler, H., Steiner, H., and Brenn, G. (2020) Self-similar pressure-atomized sprays. *Journal of Fluid Mechanics* **889**, A17.
- Hoeg, D. P., Wang, Z., Friedman, P. D., and Laoulache, R. N. (2008) Investigation of a coaxial air-blast atomizer using particle image velocimetry and computational fluid dynamics. *Atomization and Sprays* **18**, pp. 739–759.
- Howarth, L. (1948) Concerning the effect of compressibility on laminar boundary layers and their separation. *Proceedings of the Royal Society of London. Series A. Mathematical and Physical Sciences* **194**, pp. 16–42.
- Hussein, H. J., Capp, S. P., and George, W. K. (1994) Velocity measurements in a high-Reynolds-number, momentum-conserving, axisymmetric, turbulent jet. *Journal of Fluid Mechanics* **258**, pp. 31–75.

BIBLIOGRAPHY

- Jedelsky, J., Maly, M., Pinto del Corral, N., Wigley, G., Janackova, L., and Jicha, M. (2018) Air–liquid interactions in a pressure-swirl spray. *International Journal of Heat and Mass Transfer* **121**, pp. 788–804.
- Karpetis, A. N. and Gomez, A. (1998) An experimental investigation of non-premixed turbulent spray flames and their self-similar behavior. *Symposium (International) on Combustion* **27**, pp. 2001–2008.
- Karpetis, A. N. and Gomez, A. (1999) Self-similarity, momentum scaling and Reynolds stress in non-premixed turbulent spray flames. *Journal of Fluid Mechanics* **397**, pp. 231–258.
- Kessler, R. (2011) Engineered nanoparticles in consumer products: Understanding a new ingredient. *Environmental Health Perspectives* **119**, A120–A125.
- Khattab, I. S., Bandarkar, F., Fakhree, M. A. A., and Jouyban, A. (2012) Density, viscosity, and surface tension of water+ethanol mixtures from 293 to 323K. *Korean Journal of Chemical Engineering* **29** (6), pp. 812–817.
- Kobashi, Y., Yokogawa, K., Miyabe, H., Hase, R., and Kato, S. (2018) Flow fields and turbulent characteristics in non-evaporating diesel sprays. *Atomization and Sprays* **28**, pp. 735–749.
- Kourmatzis, A., Pham, P. X., and Masri, A. R. (2015) Characterization of atomization and combustion in moderately dense turbulent spray flames. *Combustion and Flame* **162**, pp. 978–996.
- Leboucher, N., Roger, F., and Carreau, J.-L. (2012) Characteristics of the spray produced by the atomization of an annular liquid sheet assisted by an inner gas jet. *Atomization and Sprays* **22**, pp. 515–542.
- Lefebvre, A. H. (1992) Energy Considerations in Twin-Fluid Atomization. *Journal of Engineering for Gas Turbines and Power* **114**, pp. 89–96.
- Lefebvre, A. H. and McDonell, V. G. (2017) Atomization and sprays. *CRC Press*, Boca Raton.
- Li, L. K. B., Dressler, D. M., Green, S. I., Davy, M. H., and Eadie, D. T. (2009) Experiments on air-blast atomization of viscoelastic liquids, part 1: Quiescent conditions. *Atomization and Sprays* **19**, pp. 157–190.
- Li, X., Chin, L. P., Tankin, R. S., Jackson, T., Stutrud, J., and Switzer, G. (1991) Comparison between experiments and predictions based on maximum entropy for sprays from a pressure atomizer. *Combustion and Flame* **86**, pp. 73–89.
- Li, X. and Shen, J. (1999) Experimental study of sprays from annular liquid jet breakup. *Journal of Propulsion and Power* **15**, pp. 103–110.

- Li, X. and Tankin, R. S. (1992) On the prediction of droplet size and velocity distributions in sprays through maximum entropy principle. *Particle & Particle Systems Characterization* **9**, pp. 195–201.
- Lorenz, C., Goetz, N. von, Scheringer, M., Wormuth, M., and Hungerbühler, K. (2011) Potential exposure of German consumers to engineered nanoparticles in cosmetics and personal care products. *Nanotoxicology* **5**, pp. 12–29.
- Medrano, F. F., Fukumoto, Y., Velte, C. M., and Hodžić, A. (2017) Mass entrainment rate of an ideal momentum turbulent round jet. *Journal of the Physical Society of Japan* **86**.
- Moon, S., Gao, Y., Wang, J., Fezzaa, K., and Tsujimura, T. (2014) Near-field dynamics of high-speed diesel sprays: Effects of orifice inlet geometry and injection pressure. *Fuel* **133**, pp. 299–309.
- Nazarenko, Y., Han, T. W., Lioy, P. J., and Mainelis, G. (2011) Potential for exposure to engineered nanoparticles from nanotechnology-based consumer spray products. *Journal of Exposure Science & Environmental Epidemiology* **21**, pp. 515–528.
- Ohnesorge, W. von (1936) Die Bildung von Tropfen an Düsen und die Auflösung flüssiger Strahlen. *Zeitschrift für Angewandte Mathematik und Mechanik* **16**, pp. 355–358.
- Oseen, C. W. (1910) Über die Stokes'sche Formel und über eine verwandte Aufgabe in der Hydrodynamik. *Arkiv för matematik, astronomi och fysik* **6** (29), pp. 1–20.
- Panchagnula, M. V. and Sojka, P. E. (1999) Spatial droplet velocity and size profiles in effervescent atomizer-produced sprays. *Fuel* **78**, pp. 729–741.
- Panchapakesan, N. R. and Lumley, J. L. (1993a) Turbulence measurements in axisymmetric jets of air and helium. Part 1. Air jet. *Journal of Fluid Mechanics* **246**, pp. 197–223.
- Panchapakesan, N. R. and Lumley, J. L. (1993b) Turbulence measurements in axisymmetric jets of air and helium. Part 2. Helium jet. *Journal of Fluid Mechanics* **246**, pp. 225–247.
- Park, J., Ham, S., Jang, M., Lee, J., Kim, S., Kim, S., Lee, K., Park, D., Kwon, J., Kim, H., Kim, P., Choi, K., and Yoon, C. (2017) Spatial-temporal dispersion of aerosolized nanoparticles during the use of consumer spray products and estimates of inhalation exposure. *Environmental Science & Technology* **51**, pp. 7624–7638.
- Park, J., Yoon, C., and Lee, K. (2018) Comparison of modeled estimates of inhalation exposure to aerosols during use of consumer spray products. *International Journal of Hygiene and Environmental Health* **221**, pp. 941–950.
- Payri, R., Tormos, B., Salvador, F. J., and Araneo, L. (2008) Spray droplet velocity characterization for convergent nozzles with three different diameters. *Fuel* **87**, pp. 3176–3182.

BIBLIOGRAPHY

- Payri, R., Viera, J. P., Wang, H., and Malbec, L.-M. (2016) Velocity field analysis of the high density, high pressure diesel spray. *International Journal of Multiphase Flow* **80**, pp. 69–78.
- Peters, N. (1997) *Four lectures on turbulent combustion*. Aachen, Germany: RWTH Aachen.
- Plateau, J. A. F. (1873) *Statique expérimentale et théorique des liquides soumis aux seules forces moléculaires*. Gauthier-Villars, Paris.
- Pope, S. B. (2000) *Turbulent Flows*. Cambridge University Press, Cambridge, New York.
- Quadros, M. E. and Marr, L. C. (2010) Environmental and human health risks of aerosolized silver nanoparticles. *Journal of the Air & Waste Management Association* **60**, pp. 770–781.
- Quadros, M. E. and Marr, L. C. (2011) Silver nanoparticles and total aerosols emitted by nanotechnology-related consumer spray products. *Environmental Science & Technology* **45**, pp. 10713–10719.
- Raliya, R., Saharan, V., Dimkpa, C., and Biswas, P. (2018) Nanofertilizer for Precision and Sustainable Agriculture: Current State and Future Perspectives. *Journal of Agricultural and Food Chemistry* **66**, pp. 6487–6503.
- Rayleigh, Lord (1878) On the instability of jets. *Proceedings of the London Mathematical Society* **10**, pp. 4–13.
- Rayleigh, Lord (1879) On the capillary phenomena of jets. *Proceedings of the Royal Society of London* **29**, pp. 71–97.
- Reitz, R. D. (1978) *Atomization and other breakup regimes of a liquid jet*. PhD thesis. Princeton University.
- Ricou, F. P. and Spalding, D. B. (1961) Measurements of entrainment by axisymmetrical turbulent jets. *Journal of Fluid Mechanics* **11**, pp. 21–32.
- Roisman, I. V. and Tropea, C. (2001) Flux measurements in sprays using phase Doppler techniques. *Atomization and Sprays* **11**, pp. 667–699.
- Rudd, M. J. (1969) A new theoretical model for the laser Dopplermeter. *Journal of Physics E: Scientific Instruments* **2**, pp. 55–58.
- Ruff, G. A., Sagar, A. D., and Faeth, G. M. (1989) Structure and mixing properties of pressure-atomized sprays. *AIAA Journal* **27**, pp. 901–908.
- Russo, S. and Gomez, A. (2006) Physical characterization of laminar spray flames in the pressure range 0.1–0.9 MPa. *Combustion and Flame* **145**, pp. 339–356.
- Saffman, M. (1987) Automatic calibration of LDA measurement volume size. *Applied Optics* **26** (13), pp. 2592–2597.

- Schlichting, H. (1933) Laminare Strahlausbreitung. *Zeitschrift für Angewandte Mathematik und Mechanik* **13**, pp. 260–263.
- Schlichting, H. and Gersten, K. (2017) Boundary-layer theory. Springer, Berlin, Heidelberg.
- Schmidt, D. P., Nouar, I., Senecal, P. K., Rutland, C. J., Martin, J. K., and Reitz, R. D. (1999) Pressure-swirl atomization in the near field. *SAE Technical Paper* **1999-01-0496**.
- Schmitt, F. G. (2007) About Boussinesq’s turbulent viscosity hypothesis: historical remarks and a direct evaluation of its validity. *Comptes Rendus Mécanique* **335**, pp. 617–627.
- Shearer, A. J., Tamura, H., and Faeth, G. M. (1979) Evaluation of a locally homogeneous flow model of spray evaporation. *Journal of Energy* **3**, pp. 271–278.
- Shraiber, A. A., Podvysotsky, A. M., and Dubrovsky, V. V. (1996) Deformation and breakup of drops by aerodynamic forces. *Atomization and Sprays* **6**, pp. 667–692.
- Sinha, A., Prakash, R. S., Mohan, A. M., and Ravikrishna, R. V. (2015) Airblast spray in crossflow - structure, trajectory and droplet sizing. *International Journal of Multiphase Flow* **72**, pp. 97–111.
- Sipperley, C. M., Bade, K. M., and Schick, R. J. (2018) Advanced processing for spray flux measurements using phase-Doppler interferometry. *Proc. ICLASS 2018*. Chicago, IL, USA.
- Solomon, A. S. P., Shuen, J.-S., Zhang, Q.-F., and Faeth, G. M. (1985) Structure of nonevaporating sprays. I - Initial conditions and mean properties. *AIAA Journal* **23**, pp. 1548–1555.
- Soltani, M. R., Ghorbanian, K., Ashjaee, M., and Morad, M. R. (2005) Spray characteristics of a liquid–liquid coaxial swirl atomizer at different mass flow rates. *Aerospace Science and Technology* **9**, pp. 592–604.
- Stokes, G. G. (1851) On the effect of the internal friction of fluids on the motion of pendulums. *Transactions of the Cambridge Philosophical Society* **9** (II), pp. 8–106.
- Su, L. K. (1998) *Measurements of the three-dimensional scalar dissipation rate in gas-phase planar turbulent jets*. Stanford, USA: Stanford University, Center for Turbulence Research, pp. 35–46.
- Taylor, G. (1960) Formation of thin flat sheets of water. *Proceedings of the Royal Society of London. Series A, Mathematical and Physical Sciences* **259**, pp. 1–17.
- Tennekes, H. and Lumley, J. L. (1972) A first course in turbulence. MIT Press, Cambridge, Massachusetts.

BIBLIOGRAPHY

- Tominaga, Y. and Stathopoulos, T. (2007) Turbulent Schmidt numbers for CFD analysis with various types of flowfield. *Atmospheric Environment* **41**, pp. 8091–8099.
- Tropea, C. (2011) Optical particle characterization in flows. *Annual Review of Fluid Mechanics* **43**, pp. 399–426.
- Tropea, C., Yarin, A., and Foss, J. F., eds. (2007) *Springer handbook of experimental fluid mechanics*. Springer, Berlin, Heidelberg.
- Vashahi, F. and Lee, J. K. (2018) Insight into the dynamics of internal and external flow fields of the pressure swirl nozzle. *Atomization and Sprays* **28**, pp. 1001–1028.
- Vega, M. de, Rodriguez, P., and Lecuona, A. (2000) Mean structure and droplet behavior in a coaxial airblast atomized spray: Self-similarity and velocity decay functions. *Atomization and Sprays* **10**, pp. 603–626.
- Walzel, P. (2019) Spraying and atomizing of liquids. *Ullmann's Encyclopedia of Industrial Chemistry*. Wiley-VCH.
- Weber, C. (1931) Zum Zerfall eines Flüssigkeitsstrahles. *Zeitschrift für Angewandte Mathematik und Mechanik* **11**, pp. 136–154.
- Wimmer, E. (2012) Entwicklung einer Technik zur Auswahl und Auslegung von Düsen zur Zerstäubung nicht Newtonscher Flüssigkeiten. PhD thesis. Graz University of Technology.
- Wozniak, G. (2003) Zerstäubungstechnik: Prinzipien, Verfahren, Geräte. Springer, Berlin, Heidelberg.
- Wu, K.-J., Santavicca, D. A., Bracco, F. V., and Coghe, A. (1984) LDV measurements of drop velocity in Diesel-type sprays. *AIAA Journal* **22**, pp. 1263–1270.
- Wynanski, I. and Fiedler, H. (1969) Some measurements in the self-preserving jet. *Journal of Fluid Mechanics* **38**, pp. 577–612.
- Yeung, W.-S. (1982) Similarity analysis of gas-liquid spray systems. *Journal of Applied Mechanics* **49**, pp. 687–690.
- Zhang, Zh. and Ziada, S. (2000) PDA measurements of droplet size and mass flux in the three-dimensional atomisation region of water jet in air cross-flow. *Experiments in Fluids* **28**, pp. 29–35.